NUMERICAL SIMULATIONS OF THE DCMIX MICROGRAVITY THERMODIFFUSION EXPERIMENTS TO ASSESS THE IMPACT OF TYPICAL INTERNATIONAL SPACE STATION REBOOSTING MANOEUVRES

Rafael Jurado Cruz

Rafael Jurado Cruz

NUMERICAL SIMULATIONS OF THE DCMIX MICROGRAVITY THERMODIFFUSION EXPERIMENTS TO ASSESS THE IMPACT OF TYPICAL INTERNATIONAL SPACE STATION REBOOSTING MANOEUVRES

DOCTORAL THESIS

UNIVERSITAT
ROVIRA i VIRGILI

Tarragona 2019

UNIVERSITAT ROVIRA I VIRGILI
NUMERICAL SIMULATIONS OF THE DCMIX MICROGRAVITY THERMODIFFUSION EXPERIMENTS TO ASSESS THE IMPACT OF TYPICAL INTERNATIONAL SPACE STATION REBOOSTING MANOEUVRES
Rafael Jurado Cruz

UNIVERSITAT ROVIRA I VIRGILI
NUMERICAL SIMULATIONS OF THE DCMIX MICROGRAVITY THERMODIFFUSION EXPERIMENTS TO ASSESS THE IMPACT OF TYPICAL INTERNATIONAL SPACE STATION REBOOSTING MANOEUVRES
Rafael Jurado Cruz

UNIVERSITAT ROVIRA I VIRGILI
NUMERICAL SIMULATIONS OF THE DCMIX MICROGRAVITY THERMODIFFUSION EXPERIMENTS TO ASSESS THE IMPACT OF TYPICAL INTERNATIONAL SPACE STATION REBOOSTING MANOEUVRES
Rafael Jurado Cruz

NUMERICAL SIMULATIONS OF THE DCMIX MICROGRAVITY THERMODIFFUSION EXPERIMENTS TO ASSESS THE IMPACT OF TYPICAL INTERNATIONAL SPACE STATION REBOOSTING MANOEUVRES

Department of Physical and Inorganic Chemistry

Author: Rafael Jurado Cruz

Supervised by: Dr. Fina Gavaldà Martínez
Dr. Josep Xavier Ruiz Martí
Dr. Jordi Pallarés Curto

UNIVERSITAT ROVIRA i VIRGILI

Tarragona 2019

UNIVERSITAT ROVIRA I VIRGILI
NUMERICAL SIMULATIONS OF THE DCMIX MICROGRAVITY THERMODIFFUSION EXPERIMENTS TO ASSESS THE IMPACT OF TYPICAL INTERNATIONAL SPACE STATION REBOOSTING MANOEUVRES
Rafael Jurado Cruz

UNIVERSITAT ROVIRA I VIRGILI
DEPARTAMENT DE QUÍMICA FÍSICA I INORGÀNICA
Campus Sescelades
Marcel·lí Domingo, s/n
43007 Tarragona
Tel. +34 977 55 81 37
Fax +34 977 55 95 63
www.quimica.urv.es

WE STATE that the present study, entitled "*NUMERICAL SIMULATIONS OF THE DCMIX MICROGRAVITY THERMODIFFUSION EXPERIMENTS TO ASSESS THE IMPACT OF TYPICAL INTERNATIONAL SPACE STATION REBOOSTING MANOEUVRES*", presented by Rafael Jurado Cruz for the award of the degree of Doctor of Philosophy, has been carried out under our supervision at the Department of Physical and Inorganic Chemistry of this university, and that it fulfils all the requirements to be eligible for the International Doctorate Award.

SUPERVISORS:

Prof. Fina Gavaldà Martínez

Prof. Josep Xavier Ruiz Martí

Prof. Jordi Pallarés Curto

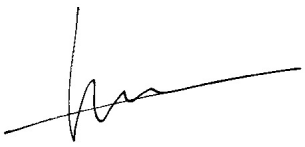

Tarragona, March 2019

UNIVERSITAT ROVIRA I VIRGILI
NUMERICAL SIMULATIONS OF THE DCMIX MICROGRAVITY THERMODIFFUSION EXPERIMENTS TO ASSESS THE IMPACT OF TYPICAL INTERNATIONAL SPACE STATION REBOOSTING MANOEUVRES
Rafael Jurado Cruz

A mi familia y a los que ya no están...

UNIVERSITAT ROVIRA I VIRGILI
NUMERICAL SIMULATIONS OF THE DCMIX MICROGRAVITY THERMODIFFUSION EXPERIMENTS TO ASSESS THE IMPACT OF TYPICAL INTERNATIONAL SPACE STATION REBOOSTING MANOEUVRES
Rafael Jurado Cruz

"A student really learns the material of course N when he or she takes course $N + 1$."

John D. Anderson J.R.

Agradecimientos

En primer lugar me gustaría dar las gracias a mis directores de tesis, Fina Gavaldà, Xavier Ruiz y Jordi Pallarés, tanto en el plano humano por su acogida y trato recibido desde que llegue a Tarragona hace algo más de tres años, como en el plano científico por todo lo aprendido a través de las discusiones sobre termodifusión que me han hecho crecer como investigador. ¡Moltes gràcies! También me gustaría dar las gracias al resto de miembros del grupo SPABE, Judit, por su colaboración durante todo este tiempo, Diana por sus correcciones a este texto y Berin por su ayuda en el desarrollo del solver en OpenFOAM, thank you buddy!

I would also like to thank professor Dala, for giving me the opportunity of doing a stay in his group at the Northumbria University in Newcastle. Also, thanks to Madeleine for helping me to improve my OpenFOAM skills. I am really grateful to Radin, Max, Amélie, Francesco, Linh and all the nice people I had the opportunity to meet there.

En estos agradecimientos no se me pueden olvidar los habitantes de Villacuqui, Yosi, Simoneti, las ibicencas Neus y Cris, la octava inquilina Meri y la quasi habitante Lauri. Gracias por esas fiestas cada fin de semana sin excepción, esos "cheese and wine" como excusa para celebrar lo que fuese, esas largas noches de juegos de mesa y por hacerme pasar sin duda, uno de los mejores cumpleaños de mi vida. Gracias a Miguelinchi y María por esos días de rally y por mantener la tradición de los juegos de mesa después de la disolución de Villacuqui. Quiero también dar las gracias a mis compañeras de piso, Antonella y Verónica por esos Aperol Spritz a la italiana. I can not forget Riccardo for keeping the italian roots in our flat and helping me improving my english. Thank you mate! También quiero agradecer a Ana por tener siempre un plan al que apuntarme y por esas largas e intensas charlas filosóficas después de la cena. A Yisus por esos ratos de ocio y ayudarme a mejorar mis habilidades dialécticas en los debates. Sin todos vosotros mi paso por Tarragona hubiera sido bien distinto.

También quiero dar las gracias especialmente a Limones por sus frecuentes llamadas simplemente para charlar o para mostrarme su apoyo en los momentos que el camino se

hacía más cuesta arriba y por hacer que no importen los kilómetros para mantener una gran amistad.

El agradecimiento más importante es sin duda para toda mi familia, por su apoyo incondicional y su amor. Gracias mamá por tu preocupación, tu inmensa generosidad, tu paciencia y por mostrarme siempre tu amor. Gracias papá por creer siempre en mi y por sentirte tan orgulloso. Quiero agradecer muy especialmente a mi abuela Rafi y mi abuelo Pepe, por su infinito amor y por ser el mejor ejemplo de vida que hubiera podido tener. Gracias abuelo por transmitirme tu pasión por la mecánica y porque desde allá donde estés me has ayudado a conseguir esto. Siempre te llevaré en mi corazón. Quiero agradecer a mi tía Mari Carmen por ser mi segunda madre y por que desde su prudencia, hace que sienta su apoyo cada día. Gracias a todos mis tíos y primos, no existen palabras suficientes para agradecer todo lo que siempre habéis hecho por mí. Os quiero.

Gracias Elena por estar siempre conmigo a pesar de la distancia y por haberme ayudado en este largo viaje, por tu paciencia y por creer siempre en mí. Esta tesis es común. Te quiero.

Quiero agradecer a todos y cada uno de los que, de una forma u otra, me han ayudado a la realización de este trabajo.

Finalmente mis agradecimientos al Ministerio de Economía y Competitividad del Gobierno de España que a través del proyecto BES-2015-074665 ha financiado la realización de este trabajo, y a la Universitat Rovira i Virgili por poner a mi disposición los recursos necesarios para su ejecución.

Publications

Indexed Journal Papers

1. **Jurado, R.**, Pallarés, J., Gavaldà, Jna., Ruiz, X., *Effect of reboosting manoeuvres on the determination of the Soret coefficients of DCMIX ternary liquid systems onboard the International Space Station*, International Journal of Thermal Sciences (Accepted February 2019)

2. **Jurado, R.**, Pallarés, J., Gavaldà, Jna., Ruiz, X., 2018, *On the impact of the ISS reboosting manoeuvres during thermodiffusion experiments of ternary liquid systems: Pure diffusion*, International Journal of Thermal Sciences, Vol. 132, pp. 186-198

3. Dubert, D., Ollé, J., **Jurado, R.**, Gavalda, J., Laverón-Simavilla, A., Ruiz, X., Shevtsova, V., 2018, *Characterization of the Accelerometric Environment of DCMIX2/3 Experiments*, Microgravity Science and Technology, Vol. 30, pp. 683-697

4. **Jurado, R.**, Gavaldà, Jna., Simón, M.J., Pallarés, J., Laverón-Simavilla, A., Ruiz, X., Shevtsova, V., 2016, *Some considerations on the vibrational environment of the DSC-DCMIX1 experiment onboard ISS*, Acta Astronautica, Vol. 129, pp. 345-356

Conferences

1. **Jurado, R.**, Pallarés, J., Gavaldà, Jna., Ruiz, X., *Gravitational instability analyses in THN-IBB-nC12 mixtures*, (ISPS-7) & (ELGRA-25) (European Space Agency), 2017, Juan-les-Pins (France)

2. Ollé, J., Dubert, D., **Jurado, R.**, Gavaldà, Jna., Ruiz, X., Laveron-Simavilla, A., Shevtsova, V., *Several considerations about the acceleration environment of the*

DCMIX2 and DCMIX3 experiments carried out in the ISS, (ISPS-7) & (ELGRA-25) (European Space Agency), 2017, Juan-les-Pins (France)

3. **Jurado, R.**, Pallarés, J., Gavaldà, Jna., Ruiz, X., *On the impact of reboosting manoeuvers in DCMIX1 experiments: Thermodiffusion in ternary liquid systems*, (ISPS-7) & (ELGRA-25) (European Space Agency), 2017, Juan-les-Pins (France)

4. **Jurado, R.**, Pallarés, J., Gavaldà, Jna., Ruiz, X. *On the impact of reboosting manoeuvers in DCMIX1 experiments: Pure molecular diffusion of ternary liquid systems*, 7th International Symposium on Advances in Computational Heat Transfer (ICHMT), 2016, Naples (Italy)

5. **Jurado, R.**, Dubert, D., Simón, M. José., Pallarés, J., Gavaldà, Jna., Ruiz, X., *Further considerations about double-diffusive convection in ternary systems DCMIX1 type*, 7th International Symposium on Advances in Computational Heat Transfer (ICHMT), 2016, Naples (Italy)

6. **Jurado, R.**, Gavalda, J., Pallarés, J., Laveron-Simavilla, A., Shevtsova, V., Ruiz, X., *The acceleration environment of the DCMIX2/3 experiments*, 12th International Meeting on Thermodiffusion, 2016, Madrid (Spain)

Abstract

The impact of the International Space Station (ISS) reboosting manoeuvres on the Diffusion and thermodiffusion Coefficient Measurements in ternary mIXtures (DCMIX) experiments has been investigated in this thesis. First of all, the microgravity environment of the ISS has been analysed by using the signals recorded by the sensors located in different modulus of the station. According to the present analysis the vibratory limit requirements are not always accomplished, especially during strong disturbances such as reboostings. These manoeuvres promote the largest level of acceleration onboard the ISS. Therefore, acceleration signals recorded during reboostings have been used to perform numerical simulations under different reboosting scenarios. A new solver implemented in the open source software, OpenFOAM, to solve numerically the different thermodiffusion problems in ternary mixtures, with the gravity as a function of time has also been developed.

During the thermodiffusive step of the DCMIX experiments, the closer the reboosting occurs to the moment of measuring the concentration field, the larger the error in the estimation of the Soret coefficient. Also, the method used for quantifying the concentration field can affect the error. The analytical solution can be used in advance, to analyse the sensitivity of the system to the acceleration. The reboosting acting in a direction perpendicular to the temperature gradient has been proven to be the most harmful acting direction, giving an error up to 64% when calculating the diffusion coefficients during the pure diffusive step of the experiment.

Contents

List of Figures

List of Tables

Chapter 1

Introduction

1.1 Scope of the DCMIX experiment series

Molecular diffusion is the transport mechanism that occurs when there is a concentration gradient in a multicomponent mixture. The concentration gradient creates a mass flux from regions of high concentration to regions of low concentration. In some mixtures, another important mass transport mechanism is the so-called thermodiffusion. In the case of thermodiffusion, the driving force which creates the mass flux is the temperature gradient. Thermodiffusion, unlike molecular diffusion, tends to increase the concentration gradient by separating the components of the mixture if $\vec{\nabla}T \neq 0$. This mass transport mechanism is also known as Soret effect. Most of the experimental techniques which aim to measure the molecular diffusion and thermodiffusion coefficients of a mixture, use the following definition of the mass flux

$$\vec{J}_i = \sum_{k=1}^{n-1} -D_{ik}\vec{\nabla}w_k - D_{Ti}\vec{\nabla}T, \tag{1.1}$$

where n is the number of components of the mixture, w_k is the mass fraction of component k, D_{Ti} is the thermodiffusion coefficient of component i, T represents the temperature, $\vec{\nabla}$ is the gradient vector and D_{ik} represents the molecular diffusion coefficients matrix. The diffusion coefficient matrix is a square matrix of dimensions $n-1$, which is the number of independent fluxes of a n components mixture. The term $D_{ik}\vec{\nabla}w_k$ for $i \neq k$, is usually referred as cross-diffusion term, while $D_{ik}\vec{\nabla}w_k$ when $i = k$, as pure diffusion term [7]. If the number of components is $n > 2$, a lot of difficulties arise when trying to measure the molecular diffusion coefficients (hereinafter diffusion coefficients) and thermodiffusion coefficients. Even in the pure diffusive case (i.e. isothermal case where there

is not Soret effect), the coupled diffusive mass fluxes among species can produce unstable concentration distributions that can hinder the measuring process. This phenomenon is called double-diffusion convection and using the linear stability analysis of the governing equations, it has been shown that can be caused not only by an unstable density gradient but also when there is a sufficiently large coupled diffusion effect [62].

It is worth mentioning that, the values of diffusion coefficients in ternary mixtures depend on the order of numbering the components of the mixture. Only the eigenvalues of the diffusion matrix are invariant with respect to the order of the components. Therefore, it is normally appropriate to order the components by decreasing density, although sometimes for measuring techniques reasons, experimentalists can choose a different order [51].

The thermodiffusion effect was discovered by Charles Soret in 1879 [91]. Soret observed experimentally how the concentration of salt of a tube filled with a salt solution in which both ends were kept at a different temperature, was not constant along the tube. He noticed a higher concentration at the cold end of the tube. Although this phenomenon was reported very briefly by the german Ludwig [57], it is still called Soret effect due to the significant contribution of Charles Soret to the topic [78].

Thermodiffusion is still today not very well understood, and although many experiments and theoretical approaches have been attempted to investigate this phenomenon, the performance of the existing models is poor or restricted to very specific types of mixtures [79]. In recent years, researchers have been carrying out many different types of experiments to measure reliable diffusion and thermodiffusion coefficients, but unfortunately there is a large disparity in the obtained results. This disparity highlights the complexity of this mass transport mechanism. It is known that the value of the diffusion and thermodiffusion coefficients is a function of the concentration and temperature. For some mixtures the thermodiffusion coefficient exhibits even a change in sign depending on the composition of the mixture. This change in sign, introduces an additional complexity when trying to establish a theoretical model, and it is still a hot topic in the field [5].

The calculation of both diffusion and thermodiffusion coefficients by means of optical techniques is based on the analytical solution of the governing equations. The analytical solution is possible just if the convective terms are neglected, in such a way that, the set of coefficient that better fits the measured concentration field can be found. Therefore any source of convection must be eliminated or at least diminished to avoid the potential sources of error.

One of the latest and more ambitious experimental attempts is the so-called Diffusion and thermodiffusion Diffusion Coefficient Measurements in ternary mIXtures (DCMIX)

project carried out by the European Space Agency (ESA). It is a series of four campaigns (initially five) of experiments performed in microgravity, to measure both diffusion and thermodiffusion coefficients in ternary liquid mixtures. The goal of this project is to deepen the thermodiffusion mechanism, which is a challenging task from the experimental and theoretical point of view even in the simplest multicomponent system, i.e. the ternary mixtures. The development of new experimental techniques such as optical techniques, makes feasible the accurate measurement of small differences in the concentration field that was not possible before. At the same time, the execution of this project will provide an extensive database of diffusion and thermodiffusion coefficients useful to investigate further different proposed theories. The knowledge gained during the different campaigns will be also useful for improving the experimental techniques used in this project.

Initially the DCMIX project was encouraged by the oil industry. The aim of the first and second campaign of the project called DCMIX1 and DCMIX2 respectively, was to obtain the diffusion and thermodiffusion coefficients of two different representative liquid ternary mixtures of oil reservoirs. In oil reservoirs unexpected concentration distributions are found due to the Soret effect, promoted by the presence of geothermal gradients [32, 37]. Therefore, the accurate determination of the thermodiffusion coefficients in ternary liquids systems is relevant because it enables the correct evaluation of transport phenomenon and then, an accurate modelling of oil reservoirs is possible [29, 97]. The better oil reservoir composition is understood the more efficient extraction of the oil resources will be.

In addition to the oil reservoirs modelling, thermodiffusion can play an important role, also in fields like biology for directing DNA molecules [25], polymer blends for phase separation [49], nuclear fusion in ionized gas [19] and diffusion in Sun [10].

After these two first campaigns, a third campaign was carried out (DCMIX3) and a fourth one (DCMIX4) has recently been executed. Table 1.1 shows the schedule and the composition of the mixtures used in each campaign.

1.1.1 DCMIX1 campaign

The selected mixture in DCMIX1 (THN-IBB-nC_{12}) experiments was a simplified representation of the hydrocarbons present in the oil reservoirs. The mixture has to be ternary to start with an easy system and be transparent in order to apply optical techniques. The naphthenic components are represented by THN, and IBB and nC_{12} represent the aromatic and aliphatic compounds of the oil, respectively. Also this composition was used because the binary pairs had already been thoroughly studied, and they are known

	Components	**Composition (Mass fraction)**	**Schedule**
DCMIX1	THN-IBB-nC_{12}	0.10-0.10-0.80 0.10-0.80-0.10 0.80-0.10-0.10 0.45-0.10-0.45 0.40-0.20-0.40 0.50-0.00-0.50	7/11/2011 - 16/01/2012
DCMIX2	Tol-Meth-Ch	0.62-0.31-0.07 0.45-0.15-0.40 0.65-0.15-0.20 0.20-0.40-0.40 0.30-0.30-0.40 0.40-0.00-0.60	1/12/2013 - 23/01/2014
DCMIX3	TEG-Water-Eth	0.60-0.20-0.20 0.33-0.33-0.33 0.15-0.25-0.60 0.10-0.75-0.15 0.40-0.50-0.10 0.00-0.85-0.15	19/09/2016 - 10/11/2016
DCMIX4	Tol-Meth-Ch	0.20-0.25-0.55 0.35-0.25-0.40 0.55-0.25-0.20	December 2018 - March 2019
	THN-Tol-Fullerene	0.60-0.3993-0.0007	
	Polystyrene-Tol-Ch	0.02-0.39-0.59	
	Polystyrene-Tol	0.02-0.98-0.00	

TABLE 1.1: Composition and schedule for each DCMIX campaign. THN.- 1,2,3,4-Tetrahydronaphthalene, IBB.- Isobutylbenzene, nC_{12}.- n-Dodecane, Tol.- Toluene, Meth.- Methanol, Ch.- Cyclohexane, TEG.- Triethylene Glycol and Eth.- Ethanol

as the Fontainebleau benchmark systems. This system was selected as a benchmark by five European research groups during a workshop held at the Ecole des Mines de Paris, Fontainebleau (France), in 1999. The purpose of this benchmark is to provide a database of reliable Soret coefficients for some specified mixtures. The Soret coefficient in binary mixture is the ratio of the thermodiffusion coefficient to the diffusion coefficient, i.e. mass separation due to thermal gradient, and homogenization due to mass diffusion (see Appendices A and B). After the DCMIX1 experiment, the mixture with mass fractions 0.80/0.10/0.10 was selected as the benchmark during the meeting of the topical team "Diffusion in non-metallic liquids" of the European Space Agency held in October 2013 in Mondragón, Spain. [66, 78, 93, 98]

1.1.2 DCMIX2 campaign

The mixture used in the DCMIX2 campaign (Tol-Meth-Ch) had already been extensively analysed on Earth laboratories using the Taylor Dispersion Technique (TDT) at 298.15 K in [35, 36], and the diffusion coefficients for a wide range of compositions were measured.

Having in advance the values of the diffusion coefficients measured on Earth was a good starting point to check the results obtained during the experiment.

The DCMIX2 mixture is also interesting to be investigated because of different features. First of all, the system is immiscible for a certain range of compositions. This immiscible zone in the concentration map is known as miscibility gap (see Figure 1.1). In addition in this immiscible zone the mixture has a critical point [98]. Particularly this mixture is interesting to be analysed in microgravity because it has a region of compositions where the Soret coefficient is negative [88] ($\backsim$ 0.8 mass fraction of Toluene for the binary mixture Tol-Meth, see Figure 1.2). The negative Soret cause an unstable concentration distribution when experiments are carried out in terrestrial conditions. The gravitational instability created by the negative Soret coefficient, promotes a convective process in the mixture making impossible to obtain any relevant result. This second campaign had some technical problems related with the manufacturing of the cells that contained the sample. The incompatibility of the mixture with the sealing material produced some leakages and bubble formation in two of the cells.

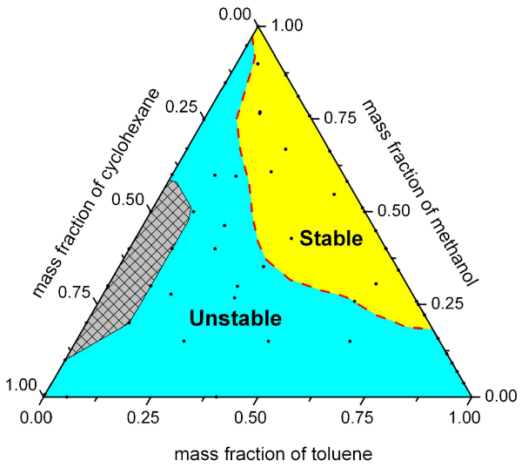

FIGURE 1.1: Concentration stability diagram of DCMIX2 mixture. Shadowed area represents the demixing zone. Blue and yellow zones represent the gravitationally unstable and stable region for terrestrial conditions [88]

1.1.3 DCMIX3 campaign

During the DCMIX3 campaign an aqueous mixture (TEG-Water-Eth) was analysed for the first time in this project. According to the literature a change in the Soret coefficient sign was reported for the binary system water/ethanol, so it was expected to have also a change in the sign of the Soret coefficient in the ternary mixture [50].

The delivery of the samples to the ISS had to be delyed till July 2016 because of the explosion of the Cygnus CRS Orb-3 unmanned aircraft in charge of carrying the

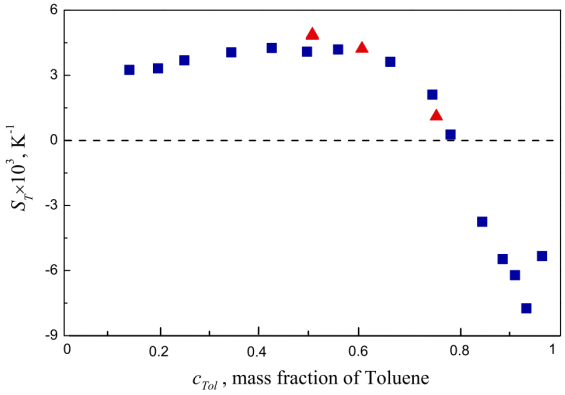

FIGURE 1.2: Experimentally obtained values of Soret coefficient for the binary mixture Tol-Meth as a function of mass fraction of Toluene. Squares correspond to the results measured in [13] and triangles show measurements using Optical Diagnostic Instrument (ODI) presented in [88]

experiment to the ISS. The explosion occurred few seconds after the take-off, destroying completely the samples, so a new experimental set up filled with new samples had to be manufactured once more. The SpaceX CRS-9 aircraft successfully took the new set up to the station. During the experiment, a small subset of the data could be used to judge the quality of the measurements. The full data, brought to Earth onboard SpaceX CRS-10, was available for analysing the results in June 2017. This campaign was not exempt of the bubble formation problem mentioned before. A growing bubble was detected in one cell, but it was at least possible to perform one bubble-free measurement with this cell [98].

1.1.4 DCMIX4 campaign

As a consequence of the problems observed with some DCMIX2 samples, the reliability of the results has been questioned. Thus, considering the novelty and importance of the obtained results, three cells of the DCMIX4 containing the same DCMIX2 mixture (Tol-Meth-Ch) with three different concentrations were further proposed.

When the eigenvalues of the mass diffusion coefficient matrix are very close, the time evolution of the two concentration profiles is similar. Therefore, the data measured with the Selectable Optical Diagnostics Instrument (SODI) apparatus can be difficult to interpret. Keeping this in mind, a Polystyrene-Toluene-Hexane system was originally chosen, since its diffusion matrix eigenvalues are expected to be separate by a factor of $\backsim$ 10. However, this system showed bubble presence after few months of compatibility tests, and had to be substituted by a Polystyrene-Tol-Ch mixture. To detect any problem during the experiment, a companion cell filled with a simpler binary Polystyrene-Tol mixture was included in the cell array. Likewise, this cell is used to establish reference values

for polymers in molecular solvent mixtures. In 2007 an experiment called GRADFLEX, carried out onboard the Russian satellite FOTON-M3, was used to investigate a similar binary system Polystyrene-Tol under microgravity conditions [22]. Thus, the data obtained during the DCMIX4, can be cross-checked with the existing results for the system. In the future an experiment with a different approach called Non-EquilibriUm Fluctuations during DIffusion in compleX liquids (NEUF-DIX) is planned to also investigate the ternary mixture of Polystyrene-Tol-Ch.

For the first time in this project, the thermodiffusion and mass diffusion coefficients and thermophysical properties of a nano-fluid mixture (THN-Tol-Fullerene), have been explored during this campaign. Presently, just the results of the binary systems are published [61]. The obtained results are expected to be of great value for the manufacturing, health, nano and biotechnology industry.

1.2 Microgravity requirements

When the thermodiffusion experiments are carried out on ground based laboratories, there is a wide region of compositions where gravitational instabilities can occur due to the buoyancy forces. In the type of experiments designed to estimate diffusion and thermodiffusion coefficients, buoyancy promoted by temperature and concentration gradients is the only driving force that can induce convection in the fluid. When convection occurs, the convective mass transport mechanism prevails over diffusion and thermodiffusion. This situation must be avoided, since the measurement of the coefficients is mostly based on the analytical solution of the mass transport equations. The only way to ensure the experiment will not develop to an unstable situation is by making null the buoyancy term. This just can happen in a gravity free environment i.e. when the value of the gravity field is zero.

Since a completely gravity free environment is impossible to achieve, currently there are different facilities for performing microgravity experiments, like drop towers, parabolic flights, sounding rockets and orbital laboratories like the International Space Station (ISS). Each of these facilities can provide a different type of microgravity environment in terms of the microgravity available time (see Figure 1.3) and mean level of residual gravity:

- **Drop Tower** $\backsim 10^{-6}\ g$
- **Parabolic flights** $\backsim 10^{-2} - 10^{-3}\ g$

- **Sounding rockets** $\backsim 10^{-4}\ g$
- **ISS** $\backsim 10^{-6}\ g$

where $g \approx 9.81\ m/s^2$ is the value of the Earth gravity.

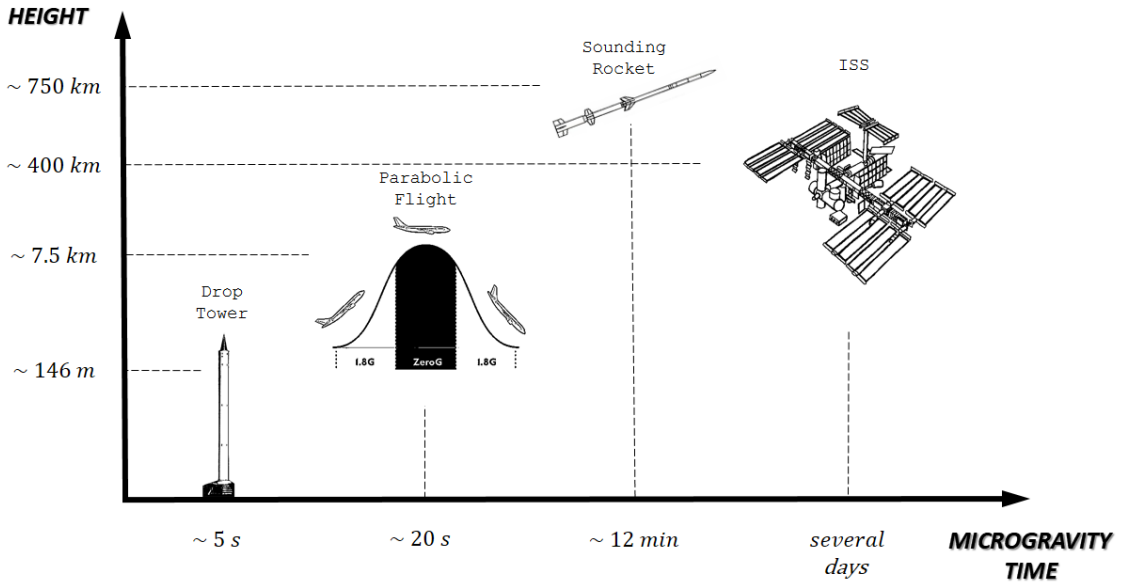

FIGURE 1.3: Microgravity time provided for the existing facilities to carry out microgravity experiments

The long duration of these experiments, typically several hours, requires a platform that can host the experiments long enough. Neglecting the buoyancy term is a reasonable assumption, as long as the gravity level is sufficiently low. Currently, orbital laboratories are the only platform that can provide the required microgravity environment for thermodiffusion experiments. Although the ISS is a suitable platform to carry out experiments in which the absence of gravity is required, different sources of vibration (usually called *g-jitter*) make the ISS a non-fully zero gravity platform. Additionally to all the background vibration sources like crew activity and rotating machinery, the largest acceleration source on the ISS are the reboosting manoeuvres [42]. These manoeuvres need to be performed periodically to keep the station in the correct orbit, otherwise the residual aerodynamic forces would make the station fall on the Earth. Beside the problem of buoyancy and the low value of the diffusion ($\hat{D}_{ik} \backsim 10^{-9}\ m^2/s$) and thermodiffusion ($\hat{D}_{Ti} \backsim 10^{-12}\ m^2/sK$) coefficients, the experiment is challenging because of the difficulty of the concentration measuring process (the hat variables denote dimensional variables). The concentration gradients all over the domain should be large enough, in such a way that the components are sufficiently separated. If the separation of one component is

small in comparison with the others, it is unfortunately, not possible to measure experimentally any diffusion coefficient for that component due to the limitations of the optical techniques used.

1.3 Relevant studies about the influence of oscillations in thermodiffusion experiments

In several studies the impact of vibration on thermodiffusion experiments carried out in microgravity environments using numerical simulations has been analysed. These studies use different approximations for modelling the gravity field, equation of state (EOS), numerical scheme, spatial dimensions of the problem and thermophysical properties.

However, the attention is normally focused on how either a low residual gravity field, a background vibration, or a combination of both affects the concentration and thermal field, although, none of the studies assesses the impact of a strong and short disturbance like a reboosting in the estimation of the diffusion and thermodiffusion coefficients. Due to the lack of knowledge on the impact of the acceleration promoted by the reboosts on DCMIX type experiments, they are typically scheduled to be performed during quiescent periods. However, sometimes unpredicted reboostings are performed and these can be done without any warning to the operations and science team. A better understanding of the impact of these kind of perturbations, can help to establish a criterion for stopping or running the experiments during this reboostings periods. The diffusion time, τ_D, is the largest time scale present in the experiment and it is related with the smallest eigenvalue of the diffusion coefficients matrix, $\hat{D}_{min}$, and a characteristic length, $\hat{L}$. For a typical DCMIX experiment in which $\hat{D}_{min} \approx 10^{-9}\ m^2/s$ and $\hat{L} = 0.005\ m$, the diffusion time $\hat{\tau}_D = \hat{L}^2/\hat{D} \approx 7\ h$ for each part of the experiment (i.e. thermodiffusion and pure diffusion step).

As mentioned before, the computational studies related to the impact of a microgravity accelerometric environment on thermodiffusive experiments, use different approximations to model the microgravity environment. One alternative is using an idealized single or multifrequency model of the microgravity environment. Another option is extracting the main frequencies present in the real acceleration signals using a Fourier analysis, trying to reproduce as faithfully as possible, the real acceleration data from a certain microgravity platform (e.g. ISS and FOTON). The last alternative, is using directly the real acceleration data during quiescent periods, as input for computing the buoyancy term, to reproduce the onboard conditions. To adjust the sampling frequency with the

computational time step, the direct acceleration measurements are also adapted by means of different strategies: Max/Min, Root Mean Square (RMS) or Interval Averaging [47].

The orientation of the gravity field with respect to the temperature gradient has critical effects on the results of the thermodiffusive experiments. In accordance with the literature [16–18, 58], it was found out that the most harmful situation is when the gravity is applied perpendicular to the temperature gradient, strongly affecting the thermodiffusive process, while directing the gravity parallel to the temperature gradient the buoyancy effect can be even completely damped [16].

A variety of gravity models have been used to study a range of frequencies combined with different levels of residual gravity. In references[46, 104], it was determined that negative effects of oscillatory gravity field, are intensified for lower frequencies and larger amplitudes. In [87] it was concluded that the heat and mass transport increases with the decrease of the frequency. Also different studies [17, 89, 104], concluded that the resulting main flow is a combination of velocity components driven by each individual frequency, so that, the flow oscillates at the same frequency of the imposed vibration.

The combination of a static residual and an oscillatory gravity field have been studied in [47, 87, 92, 94, 103–105]. Although it was observed that a static residual gravity field creates a single convective cell which could affect the experimental results [47], it was pointed out that, the residual acceleration onboard the ISS is too weak to cause a significant distortion. The combination of residual and oscillatory gravity field affects non-linearly the flow field. This non-linear interaction increases when the amplitude of the vibration is increased.

Usually the temperature field is less affected than the concentration field, remaining in some cases unaltered, due to the smaller Prandtl numbers, $\mathcal{O}(Pr) \approx 10^{-2}$, compared to the Schmidt numbers, $\mathcal{O}(Sc) \approx 10$, involved in these type of problems [6, 89].

The model used for the equation of state (EOS) was found to be critical and was based on the Perturbed Chain Statistical Associating Fluid Theory (PC-SAFT) and a weighted average EOS model [74]. The authors observed that the PC-SAFT predicts a stronger flow than the one predicted by the weighted average scheme, due to the larger density gradients obtained with the PC-SAFT model.

Also the modelling technique used for the acceleration data strongly affects the results. In [47] the authors used in the simulations a real signal coming from the ISS manipulated using different methods. The interval average method successfully models the sign of the raw accelerations but results in a smaller acceleration value. The RMS analysis results in an always positive sign of the acceleration, changing significantly the nature of the signal. The Min/Max method results in an amplified acceleration signal.

The studies [47, 86, 103], agreed that ISS is an effective platform for thermodiffusion problems, even though, by using acceleration data from the ISS, it the authors observed a strong convective cell which distorted up to 85% the separation of the components [94].

In Table 1.2, the main characteristics of the most relevant previous studies have been summarized. As stated in the literature, one can see that numerical simulations of thermodiffusion problems are controlled by many parameters such as the EOS model, numerical method used for discretizing the governing equations, gravity field applied to the experiment, diffusive and thermodiffusive coefficients model and thermophysical properties of the mixture. Due to the complexity that all these parameters give to the problem, in this work a simple model for thermodiffusion in ternary mixture has been used: laminar flow (the induced velocities in microgravity are very small), Boussinesq approximation (density varies linearly only with concentration and temperature) and constant thermophysical properties, including diffusion and thermodiffusion coefficient. In this way a simple but accurate assessment of the dynamics of the problem can be analysed with the minimum possible number of parameters.

Ref.	Year	2D/3D	Num. Method	Accelerometric environment	Mixture	EOS	Coeff. model	Visc. model	HP/HT	Orientation	ΔT	Platform
[89]	2001	2D	FEM	model real	Binary	Boussinesq	constant	constant	N/N	$\perp$ $\parallel$	–	Space Shuttle
[16]	2002	2D	FEM	model	Binary	P-R	$D(T,p)$	$\nu(T,w,p)$	Y/Y	$\perp$ $\parallel$	10	–
[18]	2005	3D	FEM	real (modeled)	Ternary	P-R	$D_{ij}(T,w_1,w_2,p)$ $D_{Ti}(T,w_1,w_2,p)$	$\nu(T,w_1,w_2,p)$	Y/Y	–	5	FOTON-12
[58]	2005	2D	FDM	model	Binary	Boussinesq	constant	constant	N/N	$\perp$ $\parallel$	–	–
[17]	2005	2D	FVM	model Earth	Binary	P-R	$D(T,w)$ $D(T,w)$	$\nu(T,w,p)$	Y/Y	$\perp$	10	–
[104]	2005	3D	FVM	model	Binary	Boussinesq	$D_T(w)$ $D = constant$	constant	N/N	$\parallel$	10	–
[87]	2007	3D	FVM FDM	model	Binary	Boussinesq	constant	constant	N/N	$\perp$	–	–
[103]	2007	3D	FVM	real (modeled)	Ternary	P-R	$D_{ij}(T,w_1,w_2)$ $D_{Ti}(T,w_1,w_2)$	constant	N/N	–	10	ISS FOTON-12
[102]	2007	3D	FVM	real (modeled)	Ternary	P-R	$D_{ij}(T,w_1,w_2,p)$ $D_{Ti}(T,w_1,w_2,p)$	constant	Y/Y	–	10	ISS
[105]	2008	3D	FVM	model	Binary	Boussinesq	constant	constant	N/N	$\perp$	10	–
[92]	2010	2D	FVM	real (modeled)	Ternary	P-R	$D_{ij}(T,w_1,w_2)$ $D_{Ti}(T,w_1,w_2)$	$\nu(w_1,w_2)$	Y/Y	–	10	FOTON-M3
[94]	2011	2D	FVM	real (modeled)	Ternary Binary	P-R PC-SAFT	$D_{ij}(T,w_1,w_2)$ $D_{Ti}(T,w_1,w_2)$	$\nu(w_1,w_2)$	Y/Y N/N	$\perp$	10 5	ISS
[74]	2012	2D	FVM	model	Binary	Weigthed-Average PC-SAFT	$D(T,w)$ $D_T(T,w)$ constant	$\nu(w)$	Y/Y	$\perp$	15	–
[46]	2012	2D	FDM	model	Binary	Boussinesq	constant	constant	N/N	$\alpha = [0,180]$	10	–
[6]	2013	2D	FDM	real (modeled)	Binary	PC-SAFT	$D(T,w)$ $D_T(T,w)$	$\nu(T,w)$	N/N	–	10	FOTON-M3 ISS
[47]	2014	2D	FDM	real (modeled)	Binary	Boussinesq	constant	constant	N/N	–	5 10	ISS
[86]	2015	3D	FVM	model	Binary	Boussinesq	constant	$\nu(T)$	N/N	$\perp$	5 10 15	–

TABLE 1.2: Main features of the most relevant studies in which the impact of microgravity environments on thermodiffusion experiments is analysed. **FVM**.- Finite Volume Method, **FDM**.- Finite Difference Method, **P-R**.- Peng-Robinson, **PC-SAFT**.- Perturbed Chain Statistical Associating Fluid Theory

In summary, using numerical simulations, the potential impact of reboosting manoeuvres on the accuracy of the results obtained during the DCMIX experiments can be analysed. This information is useful for taking decisions about possible different procedures associated with the remote operation of the runs (e.g. to stop or not the experiments

during a reboosting manoeuvre) by the Spanish User Support and Operations Centre (E-USOC) staff.

1.4 Objectives and contribution of the present study

This study aims to determine how the level of acceleration promoted by reboosting manoeuvres can affect the measuring process of the DCMIX experiments onboard the ISS. To that purpose, it has been analysed how the convection promoted by the reboostings can distort the concentration field on the actual DCMIX ternary systems. In this way, if the concentration field differs from the pure thermodiffusive analytical solution, the estimated values of the diffusion and thermodiffusion coefficients (the main objective of the DCMIX project) can be unrealistic.

First of all, the accelerometric environment during DCMIX1, DCMIX2 and DCMIX3 has been characterized both during quiescent periods (periods without reboosting or any other source of strong disturbances) and during reboostings. Real acceleration signals recorded with different sensors located in different modules of the ISS, provided by the Principal Investigator Microgravity Services (PIMS) of the National Aeronautics and Space Administration (NASA), have been used to quantify the acceleration level on the station. This information can also be used to estimate which sensors better register the acceleration experienced by the experiment.

To perform the simulations the open source C++ library OpenFOAM has been used. A new custom solver has been created to numerically resolve the equations that govern the thermodiffusion problem in ternary mixtures. In such way, DCMIX type experiments (using real thermophysical properties) under different real reboosting gravity conditions (using raw acceleration signals, without any further assumption) have been simulated. The coefficients obtained during reboosting conditions have been compared with the ones obtained experimentally to calculate the error if the experiments were run during a reboosting manoeuvre.

1.5 Structure of the thesis

In Chapter 2, the characterization of the ISS microgravity environment is presented. Signal processing techniques have been applied to study real acceleration signals coming from different sensors of the ISS. The characterization has been divided into the different DCMIX campaigns and also between quiescent periods (regular background vibration) and

weak, medium and strong disturbances like extra vehicular activities (EVA), dockings, berthings and reboostings.

Chapter 3 explains the fundamentals of the DCMIX experiments. Also the mathematical model of the problem, together with the analytical solution of both parts of the experiment (thermodiffusion and pure diffusion step) are presented. A brief description of the OpenFOAM solver used is shown in this chapter.

The results of the simulations with different compositions of the DCMIX experiments under different reboosting conditions are presented in Chapter 4. The analyses are divided in thermodiffusion and the pure diffusion step. The value of the thermodiffusion and diffusion coefficients estimated with the resulting concentration fields has been compared with the one obtained experimentally and the resulting error is reported.

Finally, Chapter 5 presents the main conclusions of the study and proposes different considerations for future studies.

Chapter 2

Accelerometric environment

2.1 Introduction

The International Space Station (ISS) is a very active environment where many daily activities can deteriorate the microgravity environment. The source of these perturbations are for example reboostings for orbital adjustments or to avoid collisions with orbital debris, dockings/berthings to bring astronauts/equipment to the ISS, undockings to return the crew to the Earth, flight attitude changes to reorient the ISS to the Sun for power supply reasons, EVA for maintenance purposes and crew activities among others [3, 15, 48, 64].

To study the impact of large disturbances (principally reboostings) on the concentration and thermal fields in DCMIX experiments, the ISS accelerometric quasi-steady and vibratory/transient range need to be accurately characterized. The quasi-steady range gives us useful information about the quasi-constant levels attained by large disturbances happened during the experiment, while the vibratory/transient range informs us about the spectral characteristics of the machinery vibrations acting simultaneously. This second range, also checks if the environment of the experiment accomplish the ISS vibratory limit requirements or not [81]. To have an accurate accelerometric characterization of any experiment carried out in the ISS, the use of data coming from the on-site sensor nearest to the experimental device is the natural choice. However, sometimes and for different reasons this is impossible and the characterization must be made based on data provided by other sensors located further from the experimental equipment, either in the same module or even in different modules of the Station. Different characterization has been made for the DCMIX1 and DCMIX2/3 campaigns. In all cases, the acceleration data have been downloaded from PIMS website [4]. The digital signal processing

technique for the DCMIX1 and DCMIX2/3 campaign will be explained in more detail in Sections 2.3 and 2.4 respectively. Further a brief summary of the analysis done for each campaign is presented:

DCMIX1 The schedule of the runs carried out during DCMIX1 campaign was not available. Thus, an eight hours averaged of the acceleration level and the corresponding RMS values during the whole campaign (November 7^{th} 2011 to January 16^{th} 2011), was used to have an insight of the accelerometric conditions during the campaign. The study was divided into a strong disturbances and a quiescent periods analysis.

DCMIX2/3 Since the runs schedule of the DCMIX2/3 campaigns was available, the specific signals recorded during the experimental runs could be analysed. For both campaigns, a quiescent period and a strong disturbance one have been chosen. Table 2.1 presents the name of the analysed runs, the microgravity episode occurred during the run and the signal processing techniques applied.

	Run	**Episode**	**Techniques**
DCMIX2	run 1b	Quiescent period	SEN
	run 16	EVA	RMS
DCMIX3	run 6	Quiescent period	SEN
	run 20a	Docking	RMS

TABLE 2.1: Runs, microgravity episode and signal processing techniques used for each DCMIX campaign. **EVA**.- Extra Vehicular Activity, **SEN**.- Spectral ENtrophy and **RMS**.- Root Mean Square

2.2 Signal processing techniques

Power Spectral Density Regarding the spectral analysis it is worth mentioning that the periodogram based directly on the Power Spectral Density (PSD), is not a consistent estimator of its true value. To perform a consistent spectral analysis, two different strategies have been used. The first one is the so-called *Welch* technique [101] and the second is the *Thomson's* multitaper method [76]. Briefly, the *Welch* technique reduces the variance of the periodogram dividing the time series into segments usually overlapped. Multiplying each segment by a window function and averaging the set of uncorrelated periodograms obtained, a final estimation of the PSD is achieved. Thus, the *Welch* method uses the segmentation to decorrelate the different modified periodograms. Unlike the *Welch* method, the *Thomson's* multitaper method does not consider segments, the method uses the entire signal and a family of mutually orthogonal windows with

optimal time-frequency concentration properties (Slepian sequences) to generate each uncorrelated periodogram. Therefore, the orthogonality of the Slepian sequences decorrelates the different modified periodograms. To calculate the PSD of the MAMS signals, the *Thomson's* method has systematically been used, but, for large SAMS2 signals, the *Welch* method with Hanning windows has been considered more versatile and operative. Mention also that, for convenience, the ordinate scale of the different graphic representations of PSD is linear for the PSD magnitude in the case *Thomson's* method (g^2/Hz), while in the *Welch* method the scale is logarithmic (dB/Hz), although, obviously, both scales are equivalent.

Wavelet Denoising In all the SAMS2 signals, due to the high sampling ratio of the sensors, there is an important amount of masking noise. Therefore, a systematic cleaning process has been carried out before any further comparison. To do so, the literature indicates two possible strategies. The classical filtering based on *Fourier* analysis and wavelet denoising using the Discrete Wavelet Transform (DWT) [85, 99]. Unlike the sine and cosine functions used in the *Fourier* Transform, the DWT decomposes the signal into a set of more versatile basic functions, obtained by dilations and translations of a mother one $\psi(j,k)$. In this way, being $\{x(n),\ \forall\ n = 0...M-1\}$ an initial discrete raw signal (of the space of all square integrable discrete functions), the discrete wavelet reconstruction, $x_{rec}(n)$, of $x(n)$ at level L, is given by [33, 77]

$$x_{rec}(n) = \sum_{j=1}^{L} \sum_{k} W_{\psi}(j,k)\psi_{j,k}(n) + \sum_{k} W_{\phi}, \tag{2.1}$$

with $W_{\psi}(j,k)$, $W_{\phi}(1,k)$ the so-called detail and approximation coefficients respectively. The factor $\psi_{j,k}(n)$ is a set of dilations and translations of the mother wavelet $\psi(j,k)$ while the other one $\phi_{j,k}(n)$ is a set of scale functions, orthogonal to $\psi(n)$, used to decompose the generic signal. The scale parameter (dilations) is related with the subindex j while that the temporal displacement (translations) is related with the subindex k.

Equivalently, the discrete wavelet reconstruction, is usually written as,

$$x_{rec} = \sum_{j=1}^{L} D_j + A_L, \tag{2.2}$$

being D_j and A_L the detail and approximation terms respectively.

The Fast Wavelet Transform (FWT) algorithm allows the calculation of the different coefficients (and so the different terms) by the use of a dyadic filter bank [21, 59, 90].

This filter bank decomposes the initial broadband of the raw signal into a collection of successively more band-limited components by repeatedly dividing the frequency range. In wavelet reconstruction only the low-frequency output of the previous level is newly decomposed into adjacents high- and low-frequency sub-bands by a high- and low-pass filter pair. Each one of the two output sub-bands is approximately half the bandwidth of the input to that level.

When the mother wavelet is a good fit for the signal, the Wavelet Denoising Technique (WDT) works considerably better than the classical filtering procedures, specially in the case of additive Gaussian white noise in which the noise is spread in all frequencies [85, 99]. If a signal has its energy concentrated in a small number of wavelet dimensions, its coefficients will be relatively large compared to the noise, which will have its energy spread over a large number of coefficients. To separate the signal into its different wavelet dimensions, a threshold value λ (or a set of values λ_j) must be considered and compared with every value of the corresponding detail coefficient $W_\psi(j,k)$, in order to decide if this value must be considered as noise or not. Despite there are many possible approaches to the estimation of threshold level, we use in here a soft thresholding [26]. In this way, this procedure eliminates those coefficients whose absolute values are lower than the corresponding threshold and shrinks the non-zero coefficients towards zero. The denoised signal is finally obtained by adding all the corrected detail terms and the final approximation. Due to the above-mentioned considerations on the filter effectiveness to eliminate noise, the denoising process has been tackled using the DWT. The first step was, thus, the selection of a suitable mother wavelet function. In the present case and after a careful visual approach trying to capture the fine details of the signals we had initially selected three generic orthogonal families, Coiflet, Daubechies and Symlet [33, 77]. In the case of Coiflets we have selected coif2, coif3 and coif4, in the case of Daubechies db3, db4, db5, db6 and db7 and in the case of Symlets sym4, sym6 and sym8. For decomposition levels between one and nine, a quantitative criterion was applied based, for simplicity, on the Percent Root Mean Square of the Difference (PRMSD) [20, 71]:

$$PRMSD = 100\sqrt{\frac{\sum(x_{rec}-x)^2}{\sum x^2}}. \tag{2.3}$$

After all this process, the DWT decomposes the raw signal into a set of terms, details and a final approximation, enabling the beginning of the denoising process [24, 44]. The determination of λ is based on the minimization of the Stein's Unbiased Risk Estimator, SURE, and a subsequent soft thresholding. However, since this last coefficient represents a low-frequency term containing valuable components of the signal, less affected by the noise, the threshold here has been restricted to the detail coefficients, not to the

approximation one [14, 95].

Root Mean Square For SAMS2 raw signals, the Root Mean Square (RMS) acceleration levels integrated over each one of the thirty-three one-third octave bands between 0.0891 and 224 Hz, have also been evaluated in order to compare it with the ISS vibratory limit requirements [81]. Hanning windows have been used in all PSD calculations [80, 81].

Spectral Entropy Magnitude (one-minute interval RMS) One-minute interval RMS together with one-minute Spectral ENtropy magnitude (SEN) have been calculated for each acceleration component [72]. SEN was calculated by means of the normalized PSD, $Q(f)$, defined as

$$Q(f) = \frac{PSD(f)}{\sum_f PSD(f)}, \tag{2.4}$$

where $PSD(f)$ is the power spectral density magnitude of the frequency bin f and $\sum_f PSD(f)$ represents the sum of the power spectral density magnitudes of all discrete frequency bins considered. Then, based on the Shannon entropy concept [84], the spectral entropy has been calculated as

$$SEN = -\frac{1}{\log(N)} \sum_f Q(f) \log(Q(f)), \tag{2.5}$$

where N is the number of discrete frequency bins considered in the $\sum_f$. Equations (2.4) and (2.5) were applied for each one of the 1320 records considered obtaining finally the minute by minute evolution of SEN along the whole experiment. SEN was evaluated for two ranges of frequencies. The first one, labelled whole frequency interval, contains all frequencies below the Nyquist frequency. The second range, labelled low frequency interval, involves frequencies less than 20 Hz. In this last case, the signals were previously low-pass filtered at 20 Hz. The particular interest in this low frequency interval is due to their potential negative impact in liquid thermodiffusive experiments [104].

SEN is an adequate parameter to quantify not only the shape of the power spectrum at a specific time, but also the distribution of the spectrum energy along the time. In this way, a high SEN value ($\backsim 1$) implies a flat spectrum with a broad spectral content, whereas a low SEN ($\backsim 0$) involves a peaked spectrum with its energy content restricted

to a small interval of frequencies. Moreover, SEN calculated through Equations (2.4) and (2.5), could explicitly separate contributions from different frequency ranges (in this case, the two intervals above mentioned) in order to observe specific alterations of each range. This represents an additional advantage comparing to RMS magnitude. The existence of a good correlation between RMS and SEN peaks was recently reported [72, 98] and it is newly confirmed here, in Figure 2.1. Also, it can be seen that SEN was more sensitive to small perturbations compared to RMS (see marked circles in Figure 2.1). Due to these favourable properties, SEN magnitude was selected as a warning parameter to detect possible disturbances during all runs.

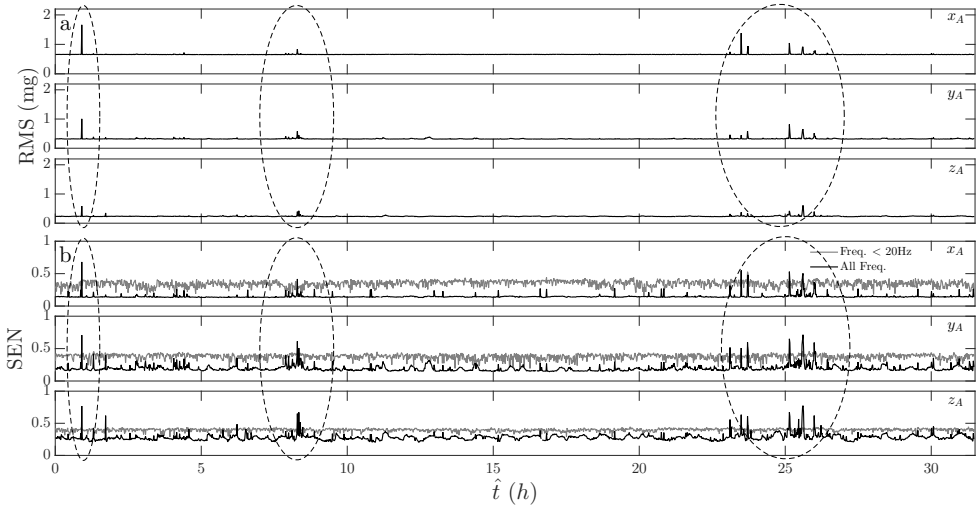

FIGURE 2.1: Minute by minute evolution of RMS (a) and SEN (b) along the three spatial directions associated to DCMIX2 experiment, Run7 (December $8^{th} - 9^{th}$ 2013)

2.3 DCMIX1 analysis

2.3.1 Sensors detail

Two different frequency ranges have been used in this signal analysis. The first one, called quasi-steady range, is referred to oscillations whose frequencies are lower than 0.01 Hz. Acceleration data in this range come from the Microgravity Acceleration Measurement System (MAMS) OSSBTMF accelerometer located in the mid-deck Lockers 3 and 4 of EXPRESS Rack 1 (ER1), in overhead bay 2 (O2) of the Destiny module (LAB1O2). The second one, called vibratory/transient range, covers oscillations between 0.01 and 400 Hz. These data come from the MAMS OSSRAW sensor also located in the LAB1O2, ER1, Lockers 3,4 and from the Space Acceleration Measurements System II (SAMS2) 121f08 sensor, at that time near Deck 1 (D1), EXPRESS Rack 3 of the Columbus module

(COL1A1, ER3, Seat Track near D1). Also, SAMS 121f02 and 121f03 sensors were at that time located in the Destiny module. SAMS2 121f02 was mounted in the Microgravity Science Glovebox (MSG) (LAB1S2, MSG, Upper Left Seat Track) while SAMS2 121f03 was placed on the lower Z panel assembly of the EXPRESS Rack 2, in overhead bay 1 (LAB1O1, ER2, Lower Z Panel). Therefore, 121f03 measured directly the vibration of the ISS structure, while 121f02 measured the Glovebox vibration. The sample rate of MAMS OSSBTMF and OSSRAW are 0.0625 Hz and 10 Hz, and the cut-off frequencies are 0.01 and 1 Hz respectively. The 121f02, 121f03 and 121f08 sensors gather data at 1000, 500 and 1000 Hz with cut-off frequencies of 400, 200 and 400 Hz, respectively. Unfortunately, simultaneous data from the Japanese module of the ISS was not available for comparisons during the different episodes analysed.

All the raw signals have been systematically demeaned (i.e. the mean value has been removed from the raw signal) to eliminate possible instrument bias before attempting any mathematical manipulation. This process does not perturb in any sense the frequency analysis. The results presented here are always related to the common ISS Absolute Coordinate System, SSA. In this reference system, the x-axis is oriented in the direction of the ISS velocity vector and z-axis is oriented toward the Earth.

2.3.2 Results

Table 2.2 details the most relevant episodes during the DCMIX1 period as well as their origin. The third column presents the interval analysed and the fourth and fifth present the sensors used. The number of data is, in all cases, high enough to properly describe the different episodes considered.

	Day	Analyzed Interval (UTC)	Analyzed Sensor		Episode Type	Origin
			MAMS	SAMS2		
1	09-11-2011	05:07-23:00	OSS RAW	121f02 121f03	QP	-
2	14-11-2011	-	-	-	SGP	Unknown
3	16-11-2011	-	-	-	DCK	Soyuz TMA-22 MKC Astraeus (Port: Mini-Research Module 2 Poisk)
4	18-11-2011	0:4:06-04:11	OSS RAW	121f02	ZOA	Thruster ignition (Zvezda Service Module)
5	21-11-2011	-	-	-	UDCK	Soyuz TMA-02 MKC Astraeus (Port: Mini-Research Module 1 Rassvet)
6	22-11-2011	-	-	-	SGP	Unknown
7	26-11-2011	-	-	-	SGP	Unknown
8	30-11-2011	11:30-21:31	OSS RAW	121f02	ZOA	Thruster ignition (Zvezda Service Module)
9	02-12-2011	11:30-23:31	OSS RAW	121f02 121f03	QP	-
10	09-12-2011	19:50-19:51	OSS RAW OSSBTMF	121f02 121f03 121f08	ZOA	Thruster ignition (Zvezda Service Module)
11	23-12-2011	-	-	-	DCK	Soyuz TMA-03 M Antares (Port: Mini-Research Module 1 Rassvet)
12	24-12-2011	13:03-23:50	OSS RAW	121f02 121f03	QP	-
13	09-01-2012	13:41-23:46	OSS RAW	121f02 121f03	QP	-
14	13-01-2012	16:18-16:23	OSS RAW	121f02	ZOA	Thruster ignition (Zvezda Service Module)

TABLE 2.2: Accelerometric episodes during the DCMIX1 experiment. **QP**.- Quiescent Period; **DCK**.- Docking; **ZOA**.- Zvezda Orbital Adjustment (reboosting); **UDCK**.- Undocking; **SGP**.- Short Generic Perturbation (unknown origin)

Figure 2.2 plots the aforementioned eight hours averaged X_A, Y_A and Z_A quasi-steady acceleration levels and the corresponding RMS values as a function of time, from November 7^{th} 2011 to January 16^{th} 2012. Similarly as the widely used spectrograms [3], this new quasi-steady strategy allows to resume in a few data points (three per day) the evolution of a long time period. Because, in the case of relatively fast events, a resolution of eight hours is very low, the information contained in these kind of plots is merely indicative. However, sharp changes correlate well with strong disturbances as orbital adjustments. Dockings and undockings can also be detected but their magnitudes are considerably lower [82].

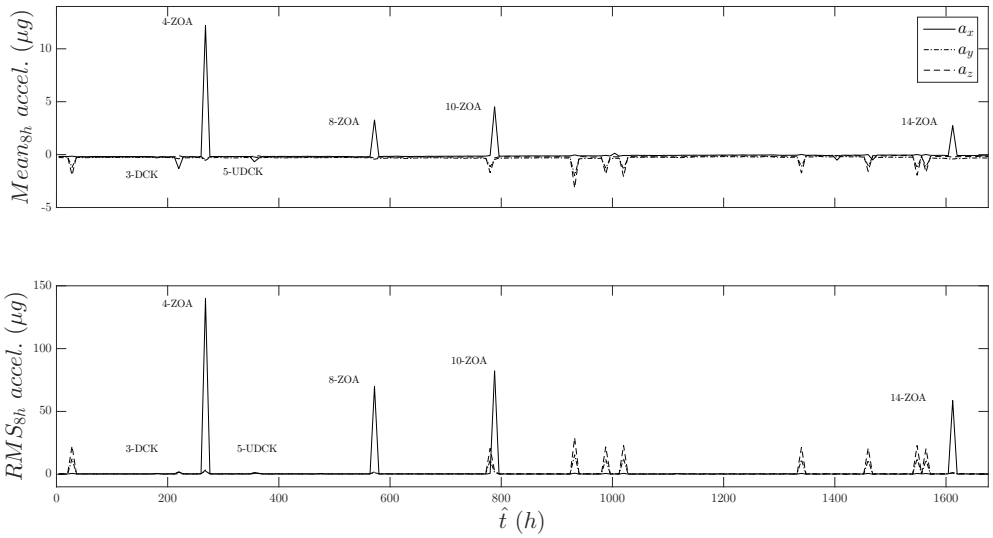

FIGURE 2.2: Eight hours averaged X_A, Y_A and Z_A quasi-steady acceleration and RMS values during DCMIX1 experiment as a function of time, from November 7^{th} 2011 to January 16^{th} 2012

In particular, the information contained in Figure 2.2 and Table 2.2 correlates the highest four peaks of the plot in the direction of X_A with the four different Zvezda Orbital Adjustments (ZOA). The fact that these disturbances always alter appreciably the X_A values (but not the other Y_A and Z_A ones) shows the high level of direction-dependence of these events. Due to the strong impact on the accelerometric footprint of the ZOAs, special attention will be paid on these kind of perturbations. To this regard, it is worth mentioning that in the case of the Zvezda Service Module the two main engines, with a thrust of 3070 N each, are reserved for orbital manoeuvring. For ZOAs the 2×16 attitude control engines (with a thrust of 130 N each) were used.

The presentation of the results, has been divided in two main sections related with the above-mentioned strong disturbances and with quiescent periods. Each of these sections will cover separately two different ranges of frequency, a low ($0 - 1$ Hz) and a high one

(up to 200/400 Hz, depending on the sensor used). This separation is a consequence of the two different cut-off frequencies of MAMS and SAMS2 sensors used.

2.3.2.1 Strong disturbances

Low sampling rate sensors The search for low frequency information has been focused on the interval $0 - 1$ Hz, the OSSRAW's standard cut-off. To do so, frequency bands instead of single frequencies has been used, since not only a certain device creates oscillations of a given frequency, but as well the elements of the ISS and the onboard equipment located near this device, oscillate with the same or similar frequency. A frequency band is, thus, better suited for the characterization of these oscillations.

To obtain the frequency bands, the Thomson's periodogram associated with each component of the four ZOAs of DCMIX1 considering separately the pre-boosting, the boosting and the post-boosting needed to be calculated. It is important to mention that, for analysing the strong disturbance periods, the frequency resolution of MAMS data is very poor due to the low number of points considered. For these periods, SAMS2 data have also been used. Then, in each of the thirty-six periodograms (4 ZOAs $\times$ x-, y- and z-direction $\times$ pre-boosting, boosting and post-boosting) analysed, the peak with the highest PSD value has been selected. The analysed bands are then located around all maxima, in such a way that the bands boundaries correspond with the values of frequency which has a magnitude equal to the fifty percent of the corresponding local maxima. Table 2.3 shows the results obtained in this study. Starred frequencies correspond to frequency values associated with the highest PSD magnitude in the corresponding periodogram. Based on these results, it can bee seen that during the four reboostings of the DCMIX experiment, the spectrum of the X_A component concentrates the higher values in the interval 0.16–0.23 Hz. Also, the Y_A component concentrates the maxima in the interval 0.62–0.71 Hz while the maxima in the Z_A direction are detected in the interval 0.24–0.37 Hz. Pre-boosting results give different frequency characteristics, compared to those during the reboosting, in the three cartesian axes. In the X_A direction higher value interval is located in 0.17–0.63 Hz. In the Z_A direction the interval is 0.11–0.72 Hz while in the Y_A direction the interval is in a higher frequency region, $0.31 - 0.98$ Hz. Post-boosting characteristics are similar to the pre-boostings ones but new single frequencies, such as 0.30 and 0.39 Hz appear. To illustrate the results compiled in Table 2.3, Figure 2.3 shows, as an example, the PSD of the X_A component (before, during and after a reboosting) for the four ZOAs analysed.

Notice that the amplitude of the different peaks increases notably during reboostings (approximately two orders of magnitude). The structural mode of the ISS, detected at

		Pre-reboosting		**Reboosting**		**Post-reboosting**	
		Freq. range	**f_{max}**	**Freq. range**	**f_{max}**	**Freq. range**	**f_{max}**
X_A	4-ZOA	0.18-0.19	0.18*	0.16-0.20	0.18*	0.18-0.19	0.18*
		0.28-0.29	0.28				
	8-ZOA	0.17-0.19	0.18	0.17-0.20	0.18*	0.17-0.18	0.18*
		0.26-0.28	0.27				
		0.60-0.63	0.62*				
	10-ZOA	0.17-0.19	0.18	0.16-0.20	0.18*	0.17-0.18	0.18*
		0.27-0.28	0.28*				
	14-ZOA	0.18-0.20	0.19*	0.17-0.23	0.19*	0.18-0.19	0.18*
Y_A	4-ZOA	0.63-0.67	0.65*	0.62-0.65	0.63*	0.27-0.29	0.28
						0.38-0.40	0.39*
		0.94-0.98	0.95			0.54-0.65	0.56
	8-ZOA	0.69-0.74	0.72*	0.62-0.66	0.64*	0.17-0.18	0.18*
						0.25-0.27	0.27
		0.81-0.86	0.84			0.83-0.85	0.85
	10-ZOA	0.69-0.72	0.71*	0.68-0.71	0.70*	0.17-0.18	0.18*
		0.83-0.85	0.84			0.30-0.31	0.30
	14-ZOA	0.31-0.32	0.32*	0.17-0.22	0.20	0.31-0.32	0.31
				0.61-0.66	0.64*		
Z_A	4-ZOA	0.11-0.12	0.12	0.28-0.31	0.30*	0.58-0.63	0.60*
		0.61-0.65	0.65*				
	8-ZOA	0.60-0.64	0.61*	0.25-0.30	0.28*	0.61-0.62	0.61*
	10-ZOA	0.11-0.12	0.11	0.24-0.28	0.26*	0.11-0.12	0.12
		0.60-0.64	0.62*				
		0.70-0.72	0.71	0.34-0.37	0.36	0.61-0.66	0.62*
	14-ZOA	0.12-0.13	0.12*	0.25-0.31	0.28	0.12-0.13	0.12
		0.60-0.66	0.63			0.58-0.64	0.62*

TABLE 2.3: Significant frequency bands at low frequency for the pre-reboosting, reboosting and post-reboosting analysed. The intervals range from the minimum and a maximum frequencies that have a magnitude value of 50% of the magnitude of the peak. Starred frequencies are the ones with the highest PSD magnitude

approximately 0.18 Hz, arises from the excitation of natural frequencies of large components of the structure, for instance the truss or the solar panel arrays during reboostings. Structural resonances generated by relatively small magnitude vibrations at just the adequate frequencies will excite these modes too. At this respect remember that for very low frequencies, structural vibrations propagate via mechanical linkage and arrive throughout the ISS with the same frequencies but different amplitudes depending on the location.

Mention that, except for the ubiquitous 0.18 Hz frequency, none of the other ones coincide with the values associated to the elastic vibrations of the ISS reported in the literature [106]. The most likely cause is the change in geometry of the ISS. The station has changed constantly due to the frequent Space Shuttle missions delivering modules (the last Shuttle to the ISS was the STS-135 Atlantis which, docked the ISS on July-10-2011, and delivered the Multi-Purpose Logistics Module, Raffaello, to complete the assembly).

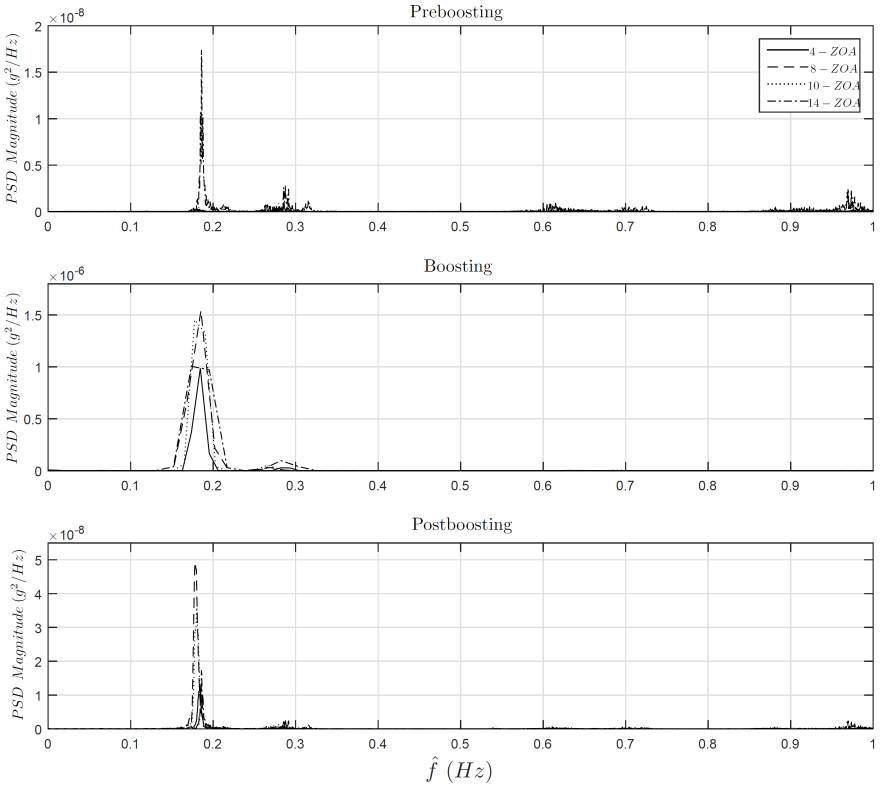

FIGURE 2.3: Low frequency spectra for the four ZOA cases of the X_A acceleration component

High sampling rate sensors The WDT procedure in the analysis of SAMS2 data will be explained step by step together with the obtained results. Also, from now on, the analysis will be concentrated in just the characterization of the orbital adjustment labelled as 10-ZOA in Table 2.2.

Figure 2.4 summarizes the calculations effected in the selection procedures of the mother wavelet function in terms of PRMSD coefficient for the three different wavelet families considered. Despite the differences, which are certainly low and depend more strongly on the particular mother wavelet used than on the level considered, results conclude that the best mother wavelet was sym8 with a detail level $L = 9$.

Figure 2.5 shows the discrete wavelet decomposition of the raw signal using the selected sym8 wavelet with a detail level $L = 9$. It can be observed that in the present case, the noise is mainly located in the first four detail terms, $D1$ to $D4$, and that the last approximation term $A9$ maintain the lowest frequency components of the raw signal.

Figures 2.6, 2.7 and 2.8 show respectively the raw signal, denoised signal and the difference between the raw and the denoised signal for the 10-ZOA. The abrupt features in the original raw signal (see Figure 2.6) at the beginning and the end of the orbital adjustment remain abrupt in the denoised one (see Figure 2.7). The denoising effect in

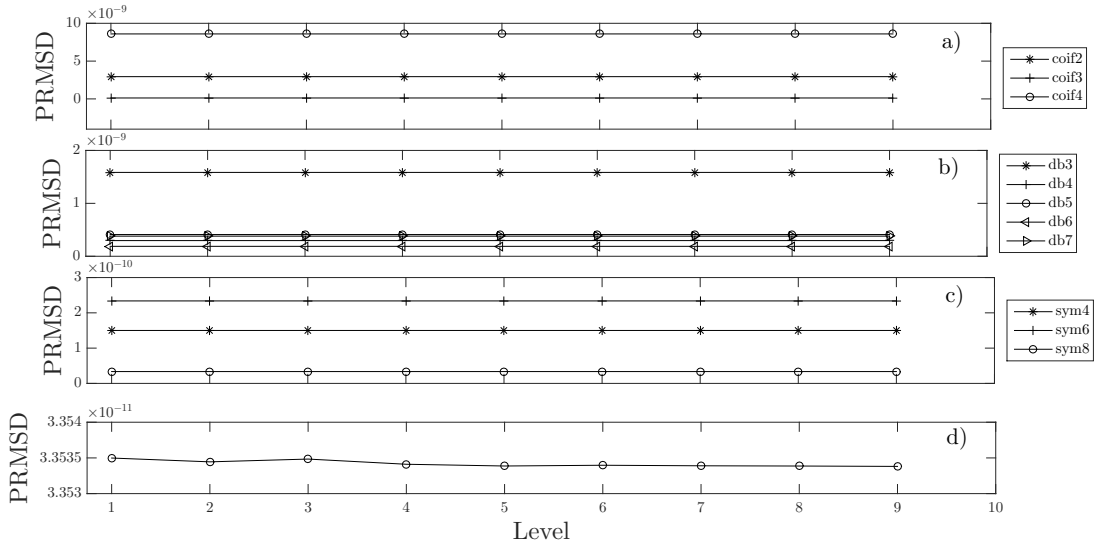

FIGURE 2.4: Wavelet selection details from 10-ZOA SAMS2 121f02 in X_A direction. Mother functions: (a) Coiflets, (b) Daubechies, (c) Symlets, and (d) detail of the results only in the sym8 case

the frequency domain is drastic, only leaving a few frequencies located in the lower part of the spectrum (see Figure 2.7). The present denoising strategy is, thus, very effective in the elimination of high frequency contents of the raw signal as it can be appreciated in Figure 2.8.

Figure 2.9 summarizes the denoised signals corresponding to 10-ZOA in the X_A direction for different SAMS2 sensors (121f02, 121f03 and 121f08) and the raw MAMS (OSSBTMF and OSSRAW) signals. Remark that OSSBTMF, OSSRAW, 121f02 and 121f03 sensors are located in the Destiny module while 121f08 is located in the Columbus one. As it is shown in Figure 2.9 an average magnitude of about 2 mg is sustained during the $\backsim$ 76 s of the ZOA's activity. The onset of the perturbation reasonably agrees in both OSSBTMF and OSSRAW signals, but due to the different sample rates, the slope at the beginning is different. Regarding the vibrational range, all denoised signals are very similar to the OSSRAW one. The denoising process eliminates higher frequencies and SAMS2 121f02, 121f03 and 121f08 sensors show a common high amplitude frequency of roughly 0.18 Hz. Figures 2.10 and 2.11 summarize the components of Y_A and Z_A. Both the quasi-steady (OSSBTMF sensor) and vibratory/transient values are considerably lower than the X_A ones. Y_A component exhibits the same pattern than Z_A, but with lower magnitude except for signals coming from the Columbus module, which have the same intensity. Also, in both Y_A and Z_A components, SAMS2 121f02 and 121f03 sensors (cases b and c in Figures 2.10 and 2.11), the amplitude is lower than the 121f08 (cases d in Figures 2.10 and 2.11). Remark finally the fact that only SAMS2 data enable to investigate on-site the low frequency contents of the different signals not only from the

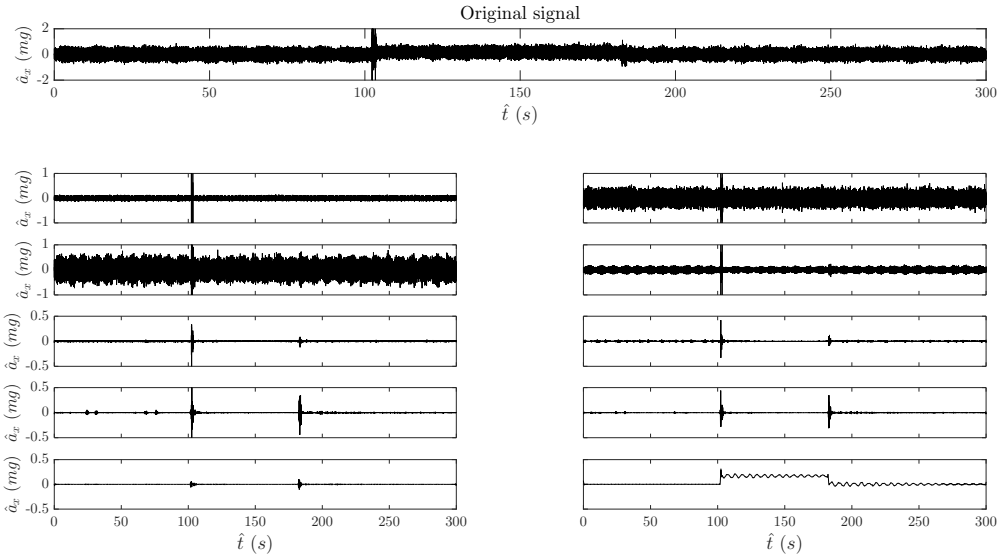

FIGURE 2.5: Original raw signal from 10-ZOA SAMS2 121f02 sensor in X_A direction, as well as approximation and detail coefficients until level 9 from its sym8 discrete wavelet decomposition.

Destiny module but also from the Columbus and Kibo ones, since there are not MAMS sensors placed in these modules.

Finally, Figure 2.12 compares the RMS values for specific one-third octave frequency bands of SAMS2 121f02, 121f03 and 121f08 to the ISS vibratory limit requirements before and during the 10-ZOA strong disturbance. Although all sensors have similar spectral features for the medium frequency range during ZOAs, the RMS level in the low frequency range ($< 1\ Hz$ approximately), increases considerably during the reboosting episode. In all cases the limits are largely exceeded. Before the reboosting, the low frequency levels of the signals coming from the SAMS2 121f02 and 121f03 sensors also exceed slightly the limits required. The Destiny SAMS2 121f02 and 121f03 signals show an increment in the bands containing the frequencies associated with air processing machinery. Mention finally that the localization of the sensor inside the Glovebox (121f02) or in contact with the structure itself (121f03) introduces significant changes in the signals mainly at the higher frequencies.

2.3.2.2 Quiescent periods

Low sampling rate sensors As mentioned before, the searching for low frequency bands in the raw MAMS OSSRAW quiescent periods have been focused on the interval 0–1.0 Hz. Figure 2.13 shows that the most significant band for the X_A component is in all the analysed cases, located between 0.18–0.20 Hz. Figure 2.13 plots the 0.15–0.3 Hz

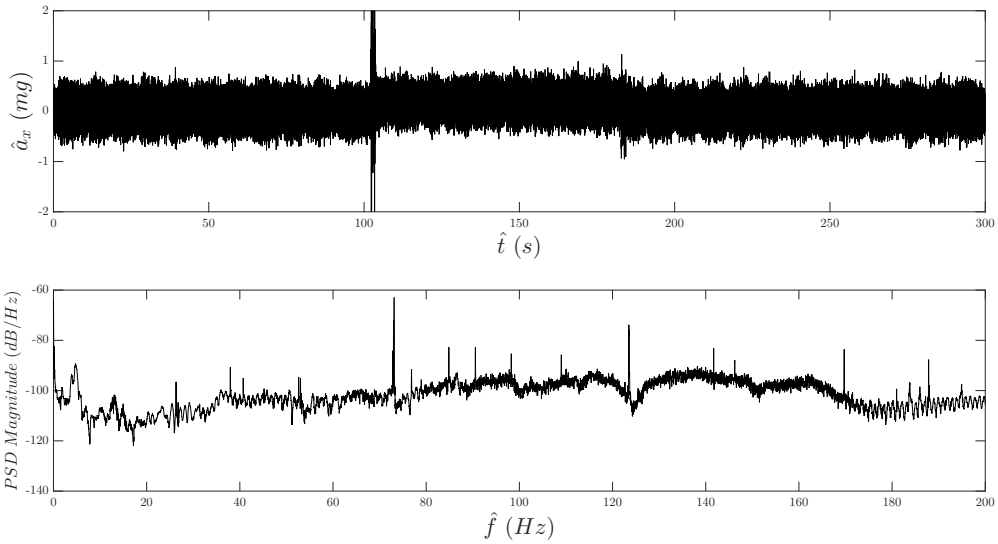

FIGURE 2.6: Raw 10-ZOA SAMS2 121f02 signal in X_A direction and Power Spectral Density

interval, since the PSD magnitude of frequencies lower than 0.15 Hz and higher than 0.3 Hz is very low. The frequency of the dominant peak in this band is 0.185 Hz, approximately. Concerning the Y_A component, the coincidence between bands for the four different signals considered is not as good as in the X_A case, but they still have common frequency bands located at 0.10–0.14 Hz, and 0.55–0.74 Hz, which have two associated peaks at 0.13 and 0.61 Hz respectively. For Z_A component, a common interval between 0.26 and 0.32 Hz has also been detected.

Table 2.4 details all the high amplitude bands found in the three components of the different signals. Notice that the band 0.18–0.20 Hz of the X_A component also appears during reboostings. This, suggests again, that this low frequency band could correlate with structural vibrations of the ISS. Concerning the Y_A and Z_A directions, there is no common bands when comparing with the reboostings results of Table 2.3.

High sampling rate sensors As typical examples of quiescent periods in the vibrational/transient range, Figure 2.14 shows the two raw signals of 1-QP recorded by the SAMS2 121f02 and 121f03 sensors located in the Glovebox and in the lower Z panel respectively. Unfortunately, Columbus module signals recorded by 121f08 sensor were not available during this period.

In this regard, it is interesting to mention that the 121f03 signal (structure) is noisier than the 121f02 one (Glovebox) except on the X_A direction. A possible explanation lies on the fact that the structure receives vibration from the whole ISS, therefore, the noise

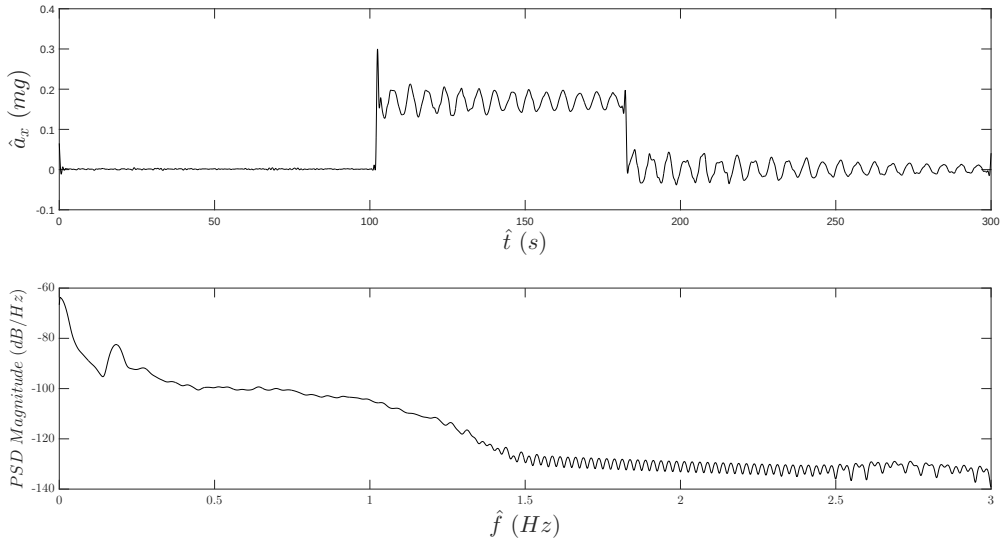

FIGURE 2.7: Denoised 10-ZOA SAMS2 121f02 signal in X_A direction and Welch's Power Spectral Density

level is higher. The Glovebox subsystems cause sudden peaks in the signal, but the level of noise is lower probably due to the isolation from the structure.

The denoising procedure applied to these couple of signals also eliminates their high frequency component (see Figure 2.15). However, now the results are not as relevant as in the previous section. In fact, this procedure does not discover any peculiar trend of the signal.

The spectral study of the SAMS2 signals have been focused on the ranges 1–400 Hz and 1–200 Hz due to the different cut-off values of both the 121f02 and 121f03 SAMS2 signals respectively. Concerning the 121f02 sensor, inside the Glovebox, the dominant frequencies are 73.11 Hz, 90.6 Hz, 98.3 Hz and 141.7 Hz (see Table 2.5). All these high values are related with machinery. For instance, 98.26 Hz could be related with the Common Cabin Air Assembly while the 73.1 Hz peak could be attributed, as mentioned before, to the Glovebox fan in open mode [3]. The spectral fingerprint of the 121f03 sensor is similar. The dominant frequency practically in all cases is found at 141.7 Hz, which corresponds to the InterModule Ventilation (IMV) fan. In other words, high frequency analysis of the quiescent periods are mainly dominated by the activity of air processing machinery. However eliminating the frequency values associated with these large amplitudes, the low frequency contents are very similar to the ones reported in subsection 2.3.2.1.

Finally, Figure 2.16 also presents the RMS acceleration values for two raw signals during 1-QP. It can be seen that, in all one-third octave bands the amplitudes are lower than the corresponding ISS requirement limits for the case of the Glovebox 121f02 sensor.

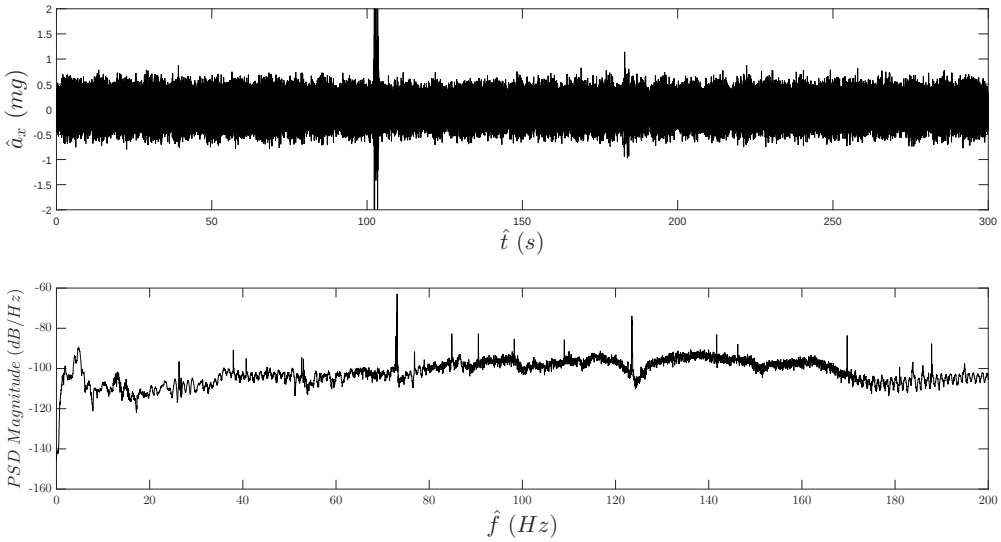

FIGURE 2.8: Difference 10-ZOA SAMS2 121f02 signal in X_A direction and Welch's Power Spectral Density

This limit is exceeded in certain bands for the signal recorded by 121f03 sensor located in contact with the ISS structure. Mention also that, 121f03 RMS values are larger than 121f02 ones at low and high frequencies.

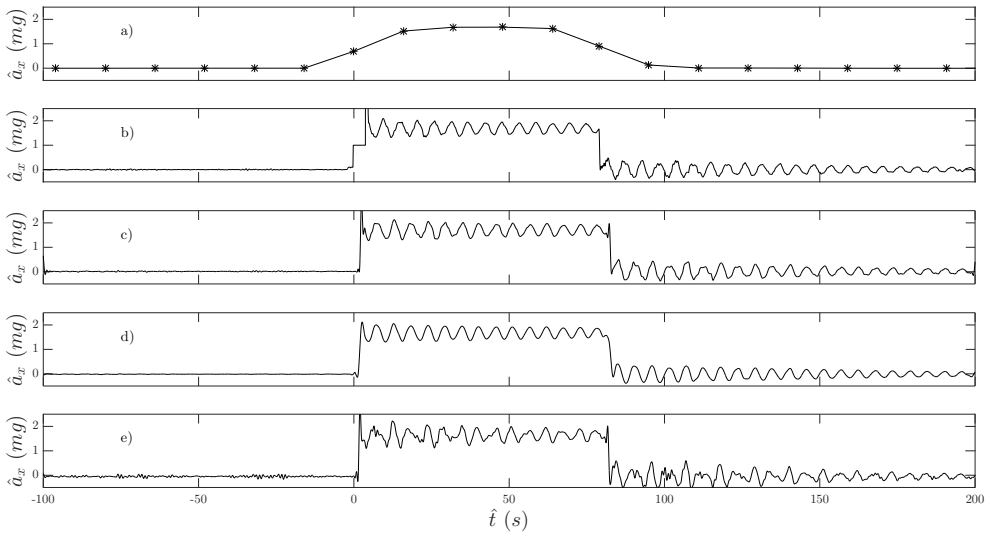

FIGURE 2.9: Quasi-steady and vibratory/transient 10-ZOA X_A signals coming from: (a) OSSBTMF and (b) OSSRAW sensors. Denoised signals from: (c) 121f02, (d) 121f03 and (e) 121f08 sensors are also plotted

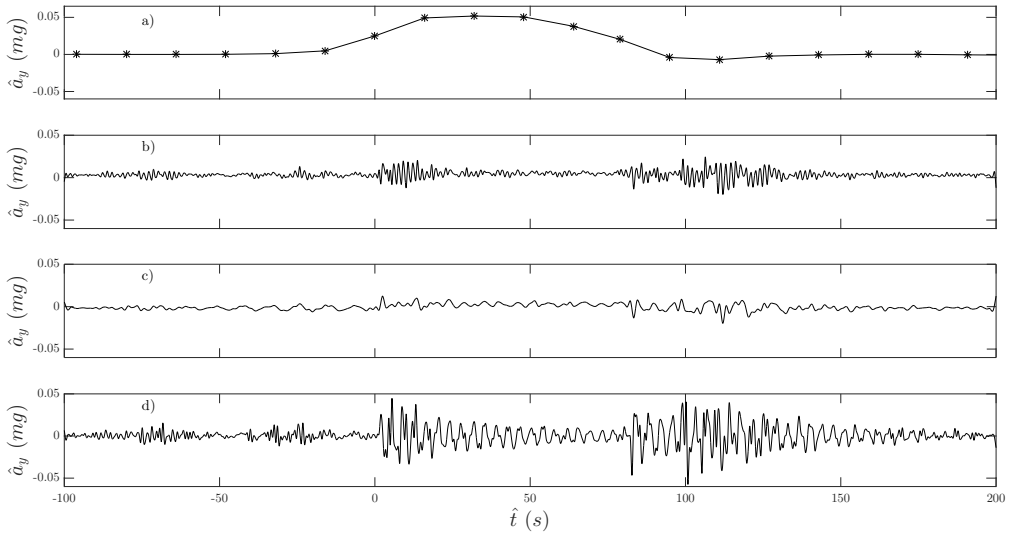

FIGURE 2.10: Quasi-steady and vibratory/transient 10-ZOA Y_A signals coming from: (a) OSSBTMF. Denoised signals from: (b) 121f02, (c) 121f03 and (d) 121f08 sensors are also plotted

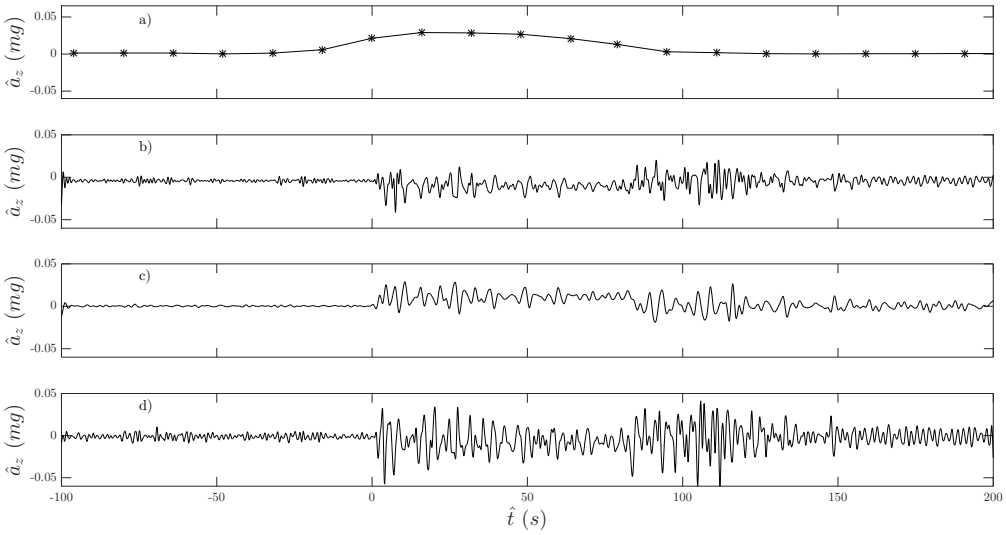

FIGURE 2.11: Quasi-steady and vibratory/transient 10-ZOA Z_A signals coming from: (a) OSSBTMF. Denoised signals from: (b) 121f02, (c) 121f03 and (d) 121f08 sensors are also plotted

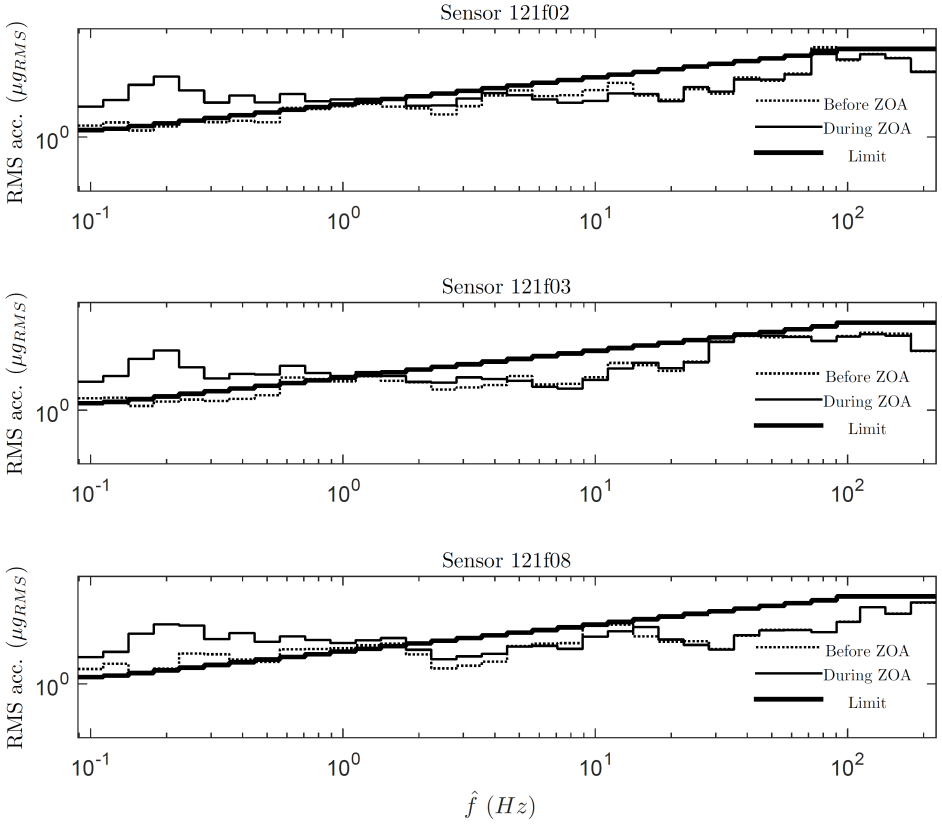

FIGURE 2.12: SAMS2 121f02-121f03-121f08 (Destiny-Destiny-Columbus) 10-ZOA RMS acceleration values vs. the ISS vibratory limit requirements

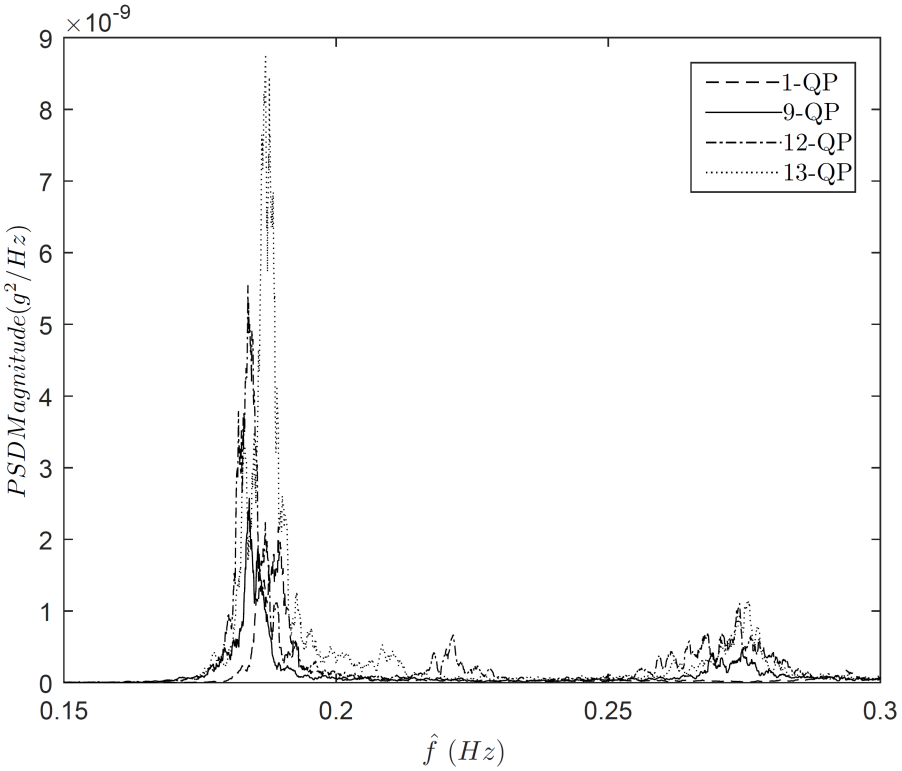

FIGURE 2.13: Thomson's power spectral densities of the four X_A components corresponding to 1-QP, 9-QP, 12-QP and 13-QP MAMS OSSRAW signals

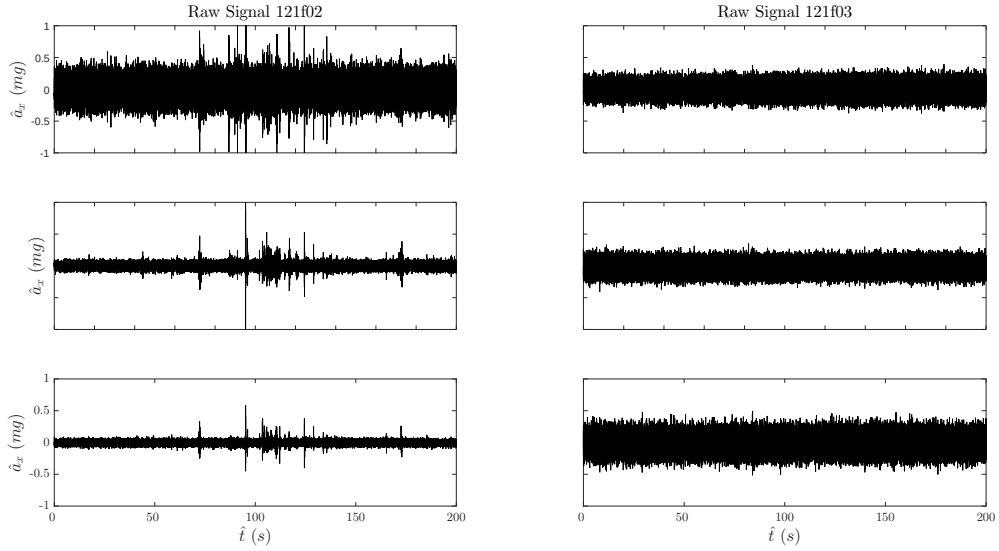

FIGURE 2.14: Raw 1-QP signals during a quiescent period from SAMS2 121f02 and 121f03 sensors in XA, YA and ZA directions

		Freq. range	$\mathbf{f_{max}}$
$\mathbf{X_A}$	1-QP	0.18-0.20	0.19*
	9-QP	0.18-0.20	0.18*
		0.26-0.28	0.27
	12-QP	0.18-0.20	0.18*
		0.27-0.28	0.27
	13-QP	0.18-0.21	0.19*
		0.27-0.28	0.27
$\mathbf{Y_A}$	1-QP	0.12-0.14	0.13*
		0.61-0.66	0.64
	9-QP	0.10-0.11	0.10
		0.58-0.67	0.61*
	12-QP	0.09-0.12	0.11
		0.26-0.28	0.26
		0.55-0.68	0.61*
	13-QP	0.10-0.11	0.10
		0.25-0.28	0.26
		0.56-0.74	0.60*
$\mathbf{Z_A}$	1-QP	0.26-0.34	0.32*
		0.41-0.42	0.41
	9-QP	0.24-0.33	0.32*
		0.39-0.42	0.41
	12-QP	0.26-0.28	0.26
		0.30-0.33	0.31*
	13-QP	0.26-0.37	0.32*
		0.56-0.57	0.57

TABLE 2.4: Significant frequency bands at low frequency for the four Quiescent Periods (1-QP, 9-QP, 12-QP and 13-QP) analysed. Starred values indicate the highest peak when more than one band has been found

Label	**Sensor**	**Frequency peak ($\mathbf{X_A}$) (Hz)**	**Frequency peak ($\mathbf{Y_A}$) (Hz)**	**Frequency peak ($\mathbf{Z_A}$) (Hz)**
1-QP	121f02	141.7	73.1	98.3
	121f03	141.7	141.7	98.3
9-QP	121f02	73.1	73.1	73.1
	121f03	141.7	141.7	141.7
12-QP	121f02	141.7	98.3	98.3
	121f03	141.7	141.7	141.7
13-QP	121f02	90.6	73.1	73.1
	121f03	141.7	141.7	141.7

TABLE 2.5: Spectral characteristics of the raw signals during the four Quiescent Periods (1-QP, 9-QP, 12-QP and 13-QP) in the vibrational/transient range

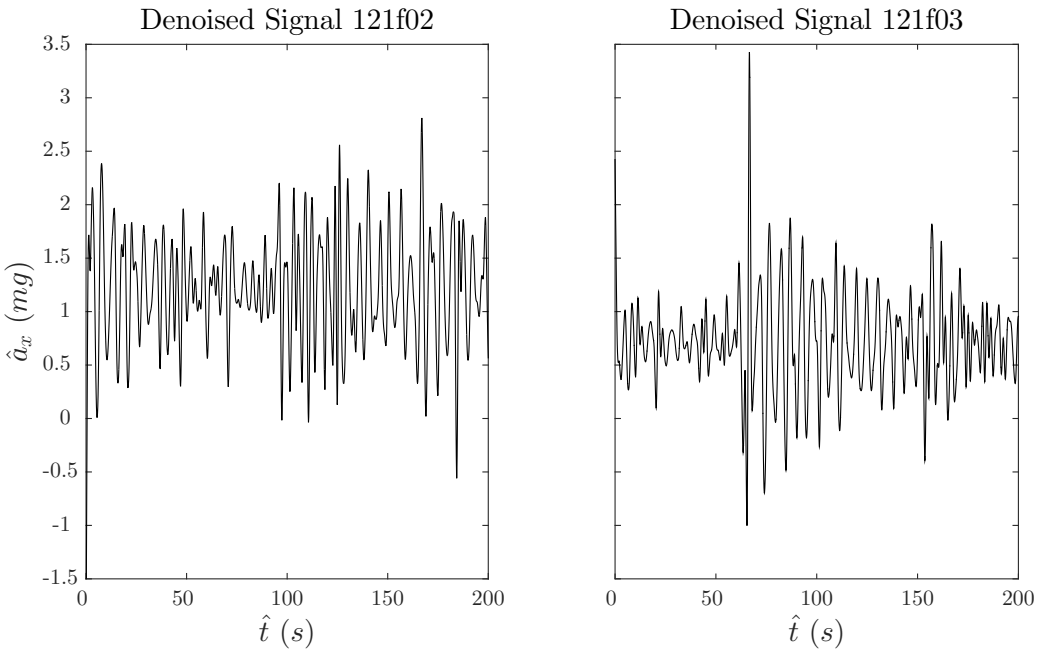

FIGURE 2.15: Denoised 1-QP signals during a quiescent period from SAMS2 121f02 and 121f03 sensors in X_A directions

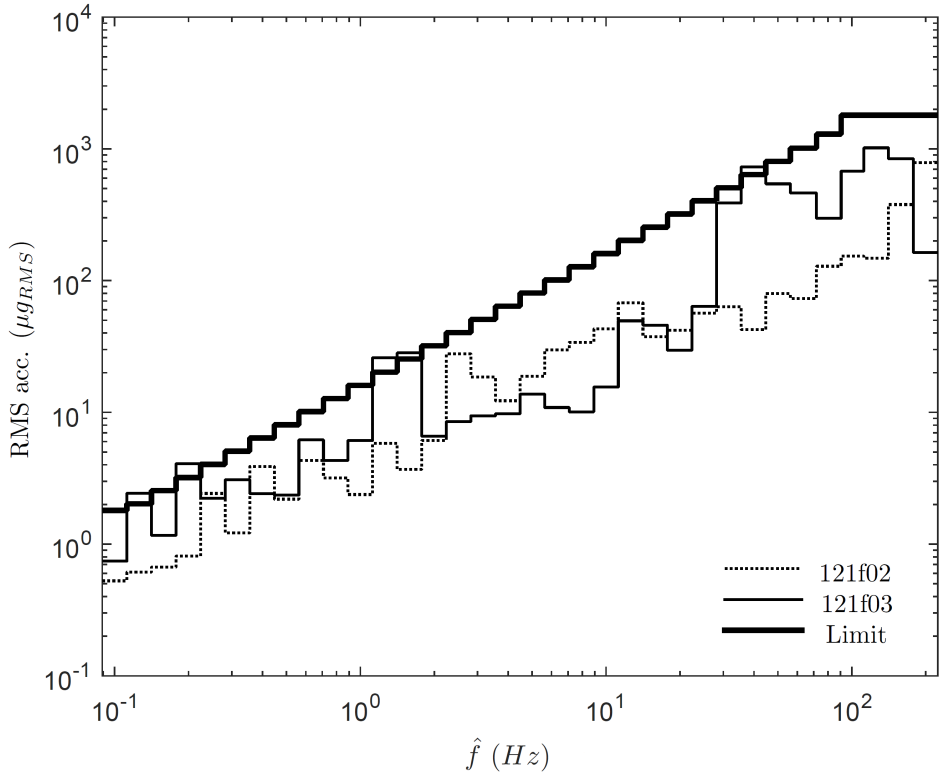

FIGURE 2.16: 1-QP RMS values from SAMS2 121f02-121f03 (Glovebox-Lower Z panel) vs the ISS vibratory limit requirements

2.4 DCMIX2 and DCMIX3 analysis

2.4.1 Sensors detail

The four signals analysed here are summarized in Table 2.6. Runs 1b and 16 correspond to DCMIX2 experiment while Runs 6 and 20a were performed during the DCMIX3 campaign. Run 16 (December 26th/27th 2013) was performed coinciding with a Russian EVA which attempted the installation of a pair of high-fidelity cameras on the exterior of the ISS (PIMS website [4]). Run 1b (December 10th/11th, 2013) was selected due to the good quality of the microgravity environment (quiescent period). In case of DCMIX3 Run 20a (October 2st/21st, 2016) coincided with the Soyuz MS-02/48S docking event carrying three crew members to the ISS (Expedition 49/50). Run 6 (September 27th/28th, 2016) was also selected as a quiescent period.

The sensors used to record DCMIX2/3 signals were: es03, 121f03, 121f08 and 121f05, thereafter S1, S2, S3 and S4, respectively. The first two were located inside the Destiny module, while the last two ones were placed in the Columbus and Kibo modules, respectively. Details of the specific position and characteristics of all sensors are presented in Table 2.7. Notice that, during the Run 16 (DCMIX2), Columbus and Kibo sensors were inoperative.

Data units are in $\hat{g}$ (9.8 m/s^2) and before any mathematical manipulation, all raw signals have been demeaned and the acceleration components always refer to the absolute ISS coordinates [40]. Unlike in the DCMIX1 analysis, the analysis has been focused in different actual runs, instead of analysing particular disturbances. Due to the long duration of all runs (around 22 hours) and to accurately detect possible disturbances the signals were segmented in 1320 records of 1 minute each [72].

Experiments	Run/Date	Spacecraft type	Port	Disturbance		Sensor used
				Type	Main direction	
DCMIX2	Run 1b 10-11/12/2013	-	-	Quiescent period		Es03 (S1) SAMS2 121f03 (S2) SAMS2 121f08 (S3) SAMS2 121f05 (S4)
	Run 16 26-27/12/2013	-	-	EVA	All directions	Es03 (S1) SAMS2 121f03 (S2)
DCMIX3	Run 6 27-28/09/2016	-	-	Quiescent period		Es03 (S1) SAMS2 121f03 (S2) SAMS2 121f08 (S3)
	Run 20a 20-21/10/2016	Soyuz MS-02/48s	Zenith port (Poisk module)	Docking	Z_A	SAMS2 121f05 (S4) Es03 (S1) SAMS2 121f03 (S2) SAMS2 121f08 (S3) SAMS2 121f05 (S4)

TABLE 2.6: Selected episodes during DCMIX2/3 experiments

Experiments		DCMIX2			DCMIX3		
Sensors	**Module**	**Localization**	**Sampling rate (Hz)**	**Cut-off freq. (Hz)**	**Localization**	**Sampling rate (Hz)**	**Cut-off freq. (Hz)**
S1	Glovebox	LAB1S2 MSG Ceiling Plate Y1-B1 Y2-A1	250	101.4	LAB1S2 MSG Floor Plate OASIS	250	101.4
S2	Destiny	LAB1O1 ER2 Lower Z Panel	500	200	LAB1O1 ER2 Lower ZPanel	500	200
S3	Columbus	COL1A1 ER3 Seat Track near D1	1000	400	COL1A3 EPM near PK-4	500	200
S4	Kibo	JPM1F5 ER4 Drawer 2	500	200	JPM1F5 ER4 Drawer 2	500	200

TABLE 2.7: Sensors used and their characteristics

2.4.2 Results

2.4.2.1 Strong disturbances

Spectral Entropy Analysis Figures 2.17a and b display minute by minute the SEN values for S1 and S2 sensors, respectively during the Run 16 of the DCMIX2 experiment. The rectangle in both figures indicates the time period corresponding to the EVA episode. SEN values associated to the three acceleration components were plotted for both low and whole frequency ranges. In case of the S1 sensor (see Figure 2.17a), SEN values calculated for the whole interval of frequencies, presented some spikes at the end of the run (approximately 20 h of experiment) for the three coordinates corresponding to the EVA disturbance period. Due to the absence of these spikes in SEN evolution of the S2 sensor (Figure 2.17b), it cannot be assured that the spikes detected were provoked by the EVA event itself. As the MSG disposes of a good vibration isolation system, the spikes identified might be originated from its own machinery devices. In addition, the SEN associated with the a_y and a_z components presents a higher degree of oscillation compared to the other one (a_x). SEN values of the sensor S2 show a more stabilized evolution all along the run.

Figure 2.18 corresponds to the Run 20a of the DCMIX3 and the rectangle shows the Soyuz docking period between 9 and 13 hours of the run. During the 22 h of experiment, SEN values were practically constant at all times for all the signals and all three coordinates, except for the one recorded by S3 sensor, which presented different periods with significant spikes and oscillations in all directions (x_A, y_A, z_A), specially if the entire range of frequencies was considered (see Figure 2.18c). In the first period with the sharpest spikes corresponding to the docking episode, SEN peaks were more pronounced in the z_A direction. This direction coincided with that of the external disturbance (See Table 2.6). The second spiky period detected at the end of the run has an unknown source. In case of the S2 sensor (see Figure 2.18b), some small oscillation can also be appreciated during the period matching with the docking event. This situation was not reproduced in the

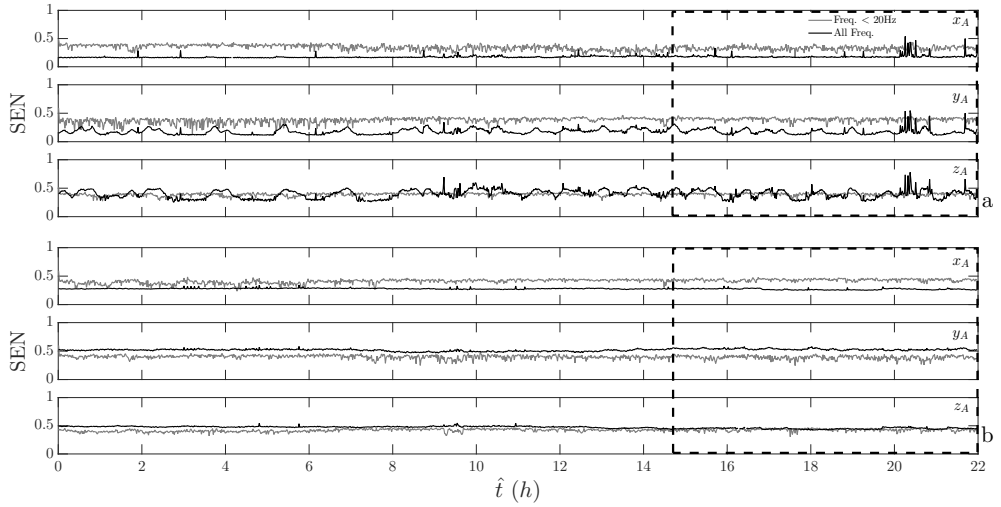

FIGURE 2.17: SEN values calculated for S1 (a) and S2 (b) sensors along the three spatial directions, during DCMIX2 experiment, Run 16. Black rectangle indicates the EVA period

other sensors (see Figures 2.18a and d).

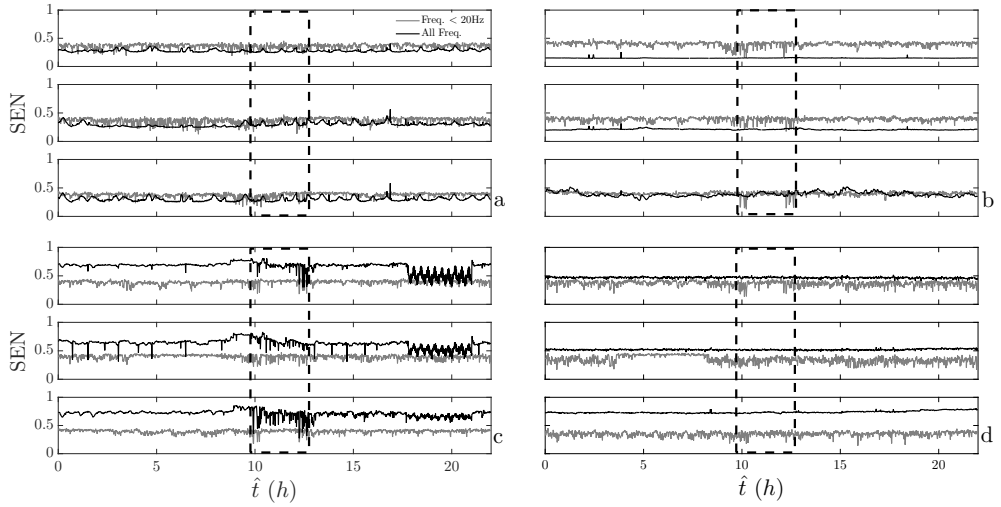

FIGURE 2.18: SEN values calculated for S1 a, S2 b, S3 c and S4 d sensors along the three spatial directions, during DCMIX3 experiment, Run 20a. Black rectangle indicates the Soyuz docking period

RMS Obtained by Integration Over Each one of the Different One-Third Octave Frequency Bands It has been demonstrated that minute by minute RMS acceleration values integrated over each one of the one-third octave bands that overcome the ISS limit requirements in the vibratory range may be visually compiled to easily warn the experimental researchers [72]. Figures 2.19, 2.20, present the RMS warning maps applied for the acceleration components of Run 16 and Run 20a signals, EVA and docking respectively. When a symbol is found in these figures, it indicates the specific time and frequency range that the RMS values surpassed the ISS limits requirements (blue

stars x_A, green circles y_A and red triangles z_A direction). In case of Run 16 (DCMIX2), for the selected sensors (see Figure 2.19) the microgravity condition was accomplished for frequencies above 10 Hz, except some warnings detected for the S1 sensor mainly in y_A and z_A directions. Note that at low frequencies the limit was surpassed during most of the duration of the experiment. These warnings detected along the experiment did not increase during the EVA period.

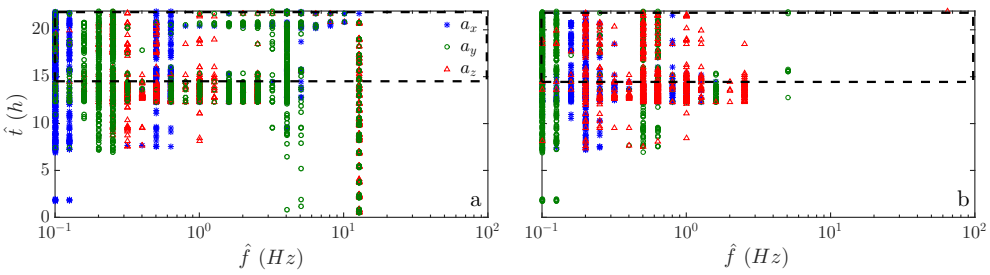

FIGURE 2.19: RMS warning map of S1 a and S2 b sensors, DCMIX2, Run 16 with EVA event (black rectangle). Symbols indicate when the RMS exceeds the ISS vibratory limit requirements

During the Run 20a of DCMIX3, Figures 2.20, the sensor S3 showed no warning for frequencies above 10 Hz, meanwhile S1, S2 and S4 surpassed the ISS limit at higher frequencies. This fact was accentuated for S2 sensor around 40 and 66 Hz bands.

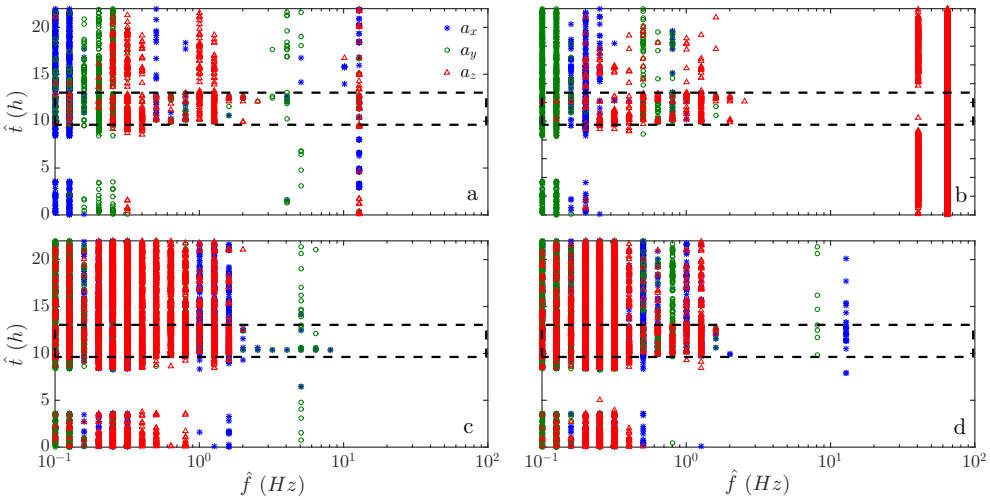

FIGURE 2.20: RMS warning map of S1 a, S2 b, S3 c and S4 d sensors, DCMIX3, Run 20a with docking event (black rectangle). Symbols indicate when the RMS exceeds the ISS vibratory limit requirements

According to the Table 2.8 the source of these particular frequencies might be the internal thermal control system equipment. Taking into account the low frequency range, the sensors placed in Columbus and Kibo modules, were more sensitive to the vibrations compared to the other two sensors, especially in the z_A direction. This behaviour was

observed considering all the signals. Focusing on the docking period, Figure 2.20 (black rectangle), non-visible increment of warnings, has been detected.

Frequency band	Sensor (type and position)	Disturbance source	Spectral fingerprint (Hz)
	MAMS HiRAP006 at LAB1O2, ER1, Lockers 3,4	Progress Docking	0.01 - 0.8 0.7 (after the event)
	SAMS2 121f08006 at COL1A1, ER3, Seat Track near D1		0.01 - 1.5
	SAMS2 121f05006 at JPM1F5, ER4, Drawer 2		
	MAMS HiRAP006 at LAB1O2, ER1, Lockers 3,4	Progress Undocking	0.2, 0.6, 1.8 0.7 (after the event)
	SAMS2 121f08006 at COL1A2, ER3, Seat Track near D1		1.3, 2, 3, 3,3, 3.7 (during the previous Russian attitude control period)
	SAMS2 121f03006 at LAB1O1, ER2, Lower Z Panel		0.01 - 3
	SAMS2 121f05 at JPM1F5, ER4, Drawer 2		
	MAMS HiRAP006 at LAB1O2, ER1, Lockers 3,4 121f03	Progress Reboost	0.01 - 1
	MAMS HiRAP006 at LAB1O2, ER1, Lockers 3,4	Progress Propellant Line Purgue	0.5 – 2
†$0.01 \leq f \leq 8\ Hz$	SAMS2 121f02 at LAB1O2, ER1, Drawer 1	Automated Transfer Vehicles, ATV, docking	≤ 6
	SAMS2 121f05006 at JPM1F5, ER4, Drawer 2		0.01 - 0.3, 0.6
	SAMS2 121f08 at COL1A1, ER3, Seat Track near D1	Automated Transfer Vehicle, ATV, Reboost	0.01 – 2
	SAMS2 121f05 at JPM1F5, ER4, Drawer 2		0.01 – 2
	MAMS HiRAP at LAB1O2, ER 1, Lockers 3,4	Soyuz Docking	≤ 6
	SAMS2 121f03 at LAB1O1, ER2, Lower Z Panel		
	SAMS2 121f02 at LAB1O2, ER1, Drawer 1	Soyuz Undocking	
	SAMS2 121f03 at LAB1O1, ER2, Lower Z Panel		
	SAMS2 121f05 at JPM1F5, ER4, Drawer 2	Solar Array Efficiency Test, **SAET** (Russian Segment thrusters were used for attitude maintenance during test, while US Control Moment Gyros, CMGs, were used before and after it)	0.5 - 1.5
	SAMS2 121f05 at LAB1O1, ER2, Upper Z Panel	Cycle Ergometer with Vibration Isolation System, **CEVIS**	0.1 – 3
	SAMS2 121f03006 at LAB1O1, ER2, Lower Z Panel	Crew exercise	≤ 3
	SAMS2 121f03 at LAB1O1, ER2, Lower Z Panel	Velosiped, **VELO-VB-3M**	2.3, 4.6
	SAMS2 121f03 at LAB1O1, ER2, Lower Z Panel	Optimized Propellant Maneuver, **OPM**	0.01 - 6
	SAMS2 121f05006 at JPM1F5, ER4, Drawer 2		
	MAMS HiRAP at LAB1O2, ER1, Lockers 3,4	Crew Glovebox Push-Off (important for Glovebox data interpretation !!!)	near 7.5
	SAMS2 121f02 at LAB1O2, ER1, Drawer 1	Ku-Band Antennas	5 – 20
	SAMS2 121f02 at LAB1O2, ER1, Drawer 1	Russian **SKV** Air Conditioner	23.5
	SAMS2 121f03 at LAB1O1, ER2, Lower Z Panel	JEM Airlock Vacuum Pump activity	24 (2nd through 4th harmonics)
	SAMS2 121f05 at JPM1F5, ER4, Drawer 2		24 (2nd through 4th harmonics)
	SAMS2 121f02 at LAB1O2, ER1, Drawer 1	Resistive Exercise Device, **RED**	≤ 30
	MAMS HiRAP at LAB1O2, ER1, Lockers 3,4	Urine Processing Assembly, **UPA**	3.6, 33.3
	SAMS2 121f03 at LAB1O1, ER2, Lower Z Panel	Robonaut operations	47.4
	SAMS2 121f04 at LAB1O2, ER1, Lower Z Panel	Internal Thermal Control System, **ITCS**	35 - 60 (also 130, 195)
	SAMS TSH-ES03 at LAB1S2, MSG, Ceiling Plate Y1-B1 Y2-A1	Microgravity Science Glovebox Operations, **MSG**	46 - 47 (normal fans mode) 73 (open fans mode)
‡$8 \leq f \leq 200\ Hz$	SAMS2 121f02 at LAB1O2, ER1, Drawer 1	Gas Analysis System for Metabolic Analysis of Physiology, **GASMAP**	57 - 58 (fan), 54 - 62 (pumps)
	SAMS2 121f02 at LAB1O2, ER1, Drawer 1	Medical Equipment Computer, **MEC**	59.5 – 70.4
	SAMS2 121f02 at LAB1O2, ER1, Drawer 1	Periodic Fitness Evaluation, **PFE**	68 – 72
	SAMS2 121f05 at JPM1F5, ER4, Drawer 2	FROST Stirling Cooler	80
	SAMS2 121f08 at COL1A3, EPM, near PK-4	Centrifuge Rotor of **Biolab**	86.5, 107.3
	SAMS2 121f03 at LABO1, ER2, Lower Z Panel	Station Control Moment Gyroscopes, **CMGs**	110
	SAMS2 121f02 at LAB1S2, MSG, Upper Left Seat Track	General Laboratory Active Cryogenic ISS Experimental Refrigerator, **GLACIER**	60, 120, 180 (start-up)
	SAMS2 121f08 at COL1A2, ER3, Seat Track near D1	Columbus General Laboratory Active Cryogenic ISS Experimental Refrigerator, **GLACIER-3**	116 - 120 (start-up) near 80 (steady state)
	SAMS2 121f03 at LAB1O1, ER2, Lower Z Panel	Common Cabin Air Assembly, **CCAA**	53 - 128 (inlet variable speed fan) 95 - 100 (water separator fan)
	SAMS2 121f08 at COL1A3, EPM, near PK-4	Electro-Magnetic Levitator, **EML**, in the European Drawer Rack	50 – 90 140 - 170
	SAMS TSH-ES06 at LAB1S4, Fluid Integrated Rack(FIR)	**LAB** Aft Port IMV fan	141.7
	SAMS2 121f04 at LAB1O2, ER1, Lower Z Panel	InterModule Ventilation fans, **IMV**	139 – 145

†This band includes the frequency range of the structural modes of the Station. These modes could be excited when short impulsive forces (reboostings) mechanically excite large components of the structure as, for instance, the main Truss and/or the solar panels. Also when different Station manoeuvres are effected in order to prepare spacecraft dockings or undockings (for instance, in case of docking, a typical ISS manoeuvre could start from -XVV/ + ZLV TEA attitude to –XVV/ + ZLV and back again to -XVV/ + ZLV TEA; similarly, an ISS manoeuvre for undocking could start from + XVV/ + ZLV TEA attitude to + ZVV/-XLV and then back again to + XVV/ + ZLV TEA)
‡This band includes the frequency range of the Station internal subsystems, like pumps and fans, used in the different kind of scientific experiments as well as in life support equipment

TABLE 2.8: Spectral fingerprints of several sources of mechanical disturbances [3, 41, 65]

2.4.2.2 Quiescent Periods

Spectral Entropy Analysis Figure 2.21 displays SEN evolution calculated for the three acceleration components corresponding to a quiescent period of the DCMIX2 experiment (Run 6) and for the four sensors considered. Notice that the signal coming from S1 sensor lasted 20 h approximately (not 22 h) due to lack of data. The sensor that presented more spikes was S1 and these were more pronounced in y_A and z_A directions.

Remark that, the spikes in SEN does not mean perturbations itself, but a change in the spreading of the spectral content at a specific time. As the above spikes appeared only in the SEN values related with whole frequency interval, they could probably be the result of the running machinery (high frequencies) inside the Glovebox [41]. SEN values for the other three sensors, showed a more stable evolution all along the experiment.

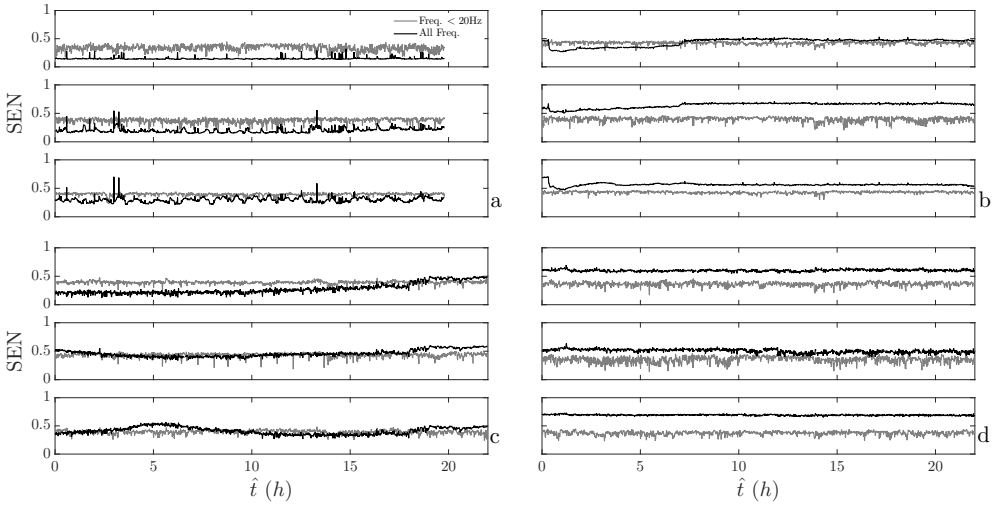

FIGURE 2.21: SEN values calculated for S1 a, S2 b, S3 c and S4 d sensors along the three spatial directions during DCMIX2 experiment, Run 1b

Analysing the signals coming from the four selected sensors during the quiescent Run 6, (see Figure 2.22), a very similar behaviour in SEN values was observed for both frequency intervals and for the three components. There was though a small difference in the degree of oscillation, when sensor S3 and the whole range of frequency were involved (see Figure 2.22c). In particular, intense spikes were detected along the 22 h of the run mainly in the z_A direction. In other words, the sensor located in the Columbus module always showed high sensibility to vibratory environment compared to the other ones.

During both experiments, S1 sensor showed different patterns compared to S3 and S4 ones, located in the Columbus and Kibo modules, respectively. Some similarities have been detected between S1 and S2 sensors, both placed in the same Destiny module during DCMIX3 runs (Figures 2.18a and b and 2.22a and b). Therefore, these slight differences in patterns, might be due to distinct S1 sensor location in DCMIX2 and DCMIX3 experiments (See Table 2.7). This suggests that the position of the sensors within the modules is an important factor to take into account when interpreting the results.

RMS Obtained by Integration Over Each one of the Different One-Third-Octave Frequency Bands Comparing the signals during the quiescent period of DC-

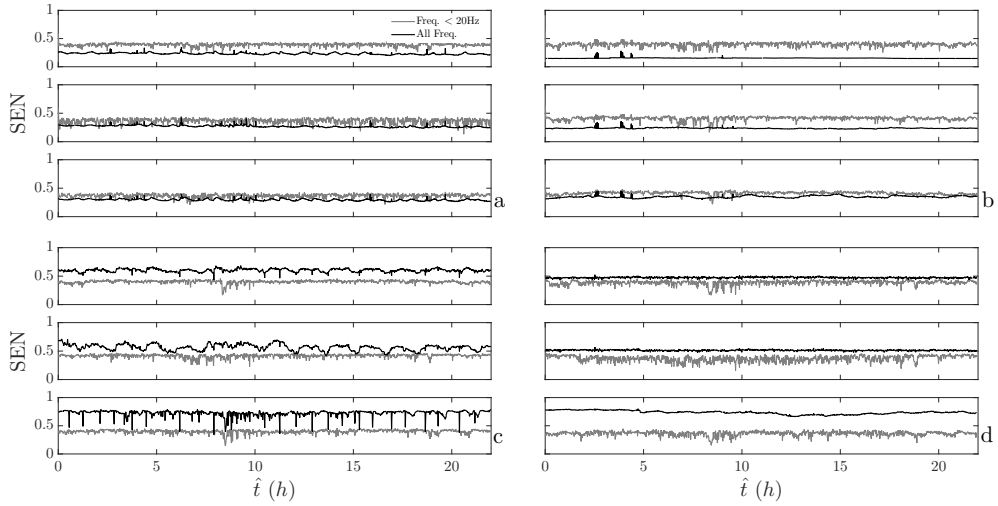

FIGURE 2.22: SEN values calculated for S1 a, S2 b, S3 c and S4 d sensors along the three spatial directions, during DCMIX3 experiment, Run 6

MIX2 (see Figure 2.23), the sensors located in Columbus and Kibo modules, were more affected by vibrations, especially considering the low frequency range (less than 10 Hz) and z_A direction. Like in DCMIX2 EVA, Figure 2.24 shows that the microgravity mode condition was accomplished for frequencies above 10 Hz for the sensor S3, and once more, sensors S1, S2 and S4 surpassed the ISS limits.

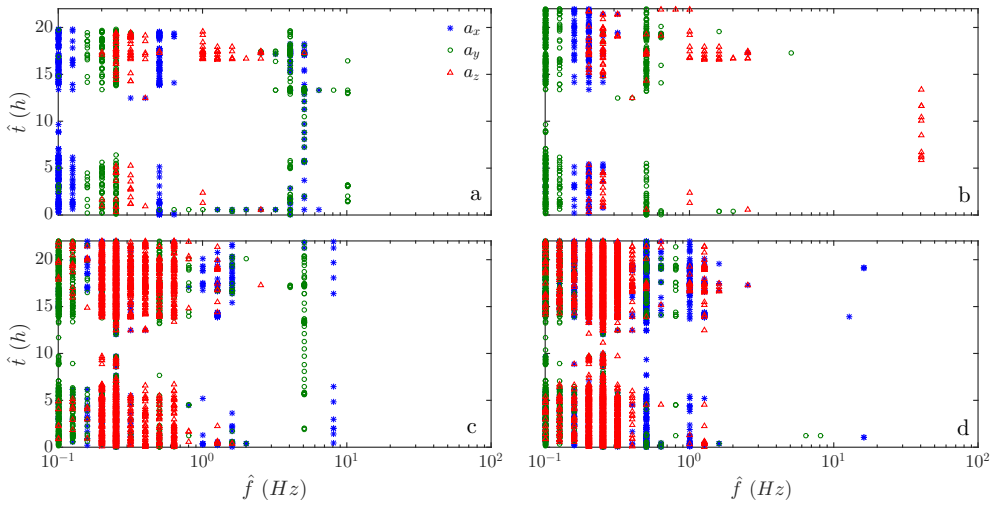

FIGURE 2.23: RMS warning map of S1 a, S2 b, S3 c and S4 d sensors, DCMIX2, Run 1b. Symbols indicate when the RMS exceeds the ISS vibratory limit requirements

Table 2.8 summarizes the main spectral fingerprints of different mechanical disturbances compiled from the NASA PIMS Microgravity Environment Handbook [4, 41, 63]. Remark that, the 73.1 Hz frequency was detected as dominant frequency for the signals coming from S1 sensor located in the MSG and for the three components. According to the Table 2.8 this peak can be attributed to the MSG fan in open mode. In the case of the

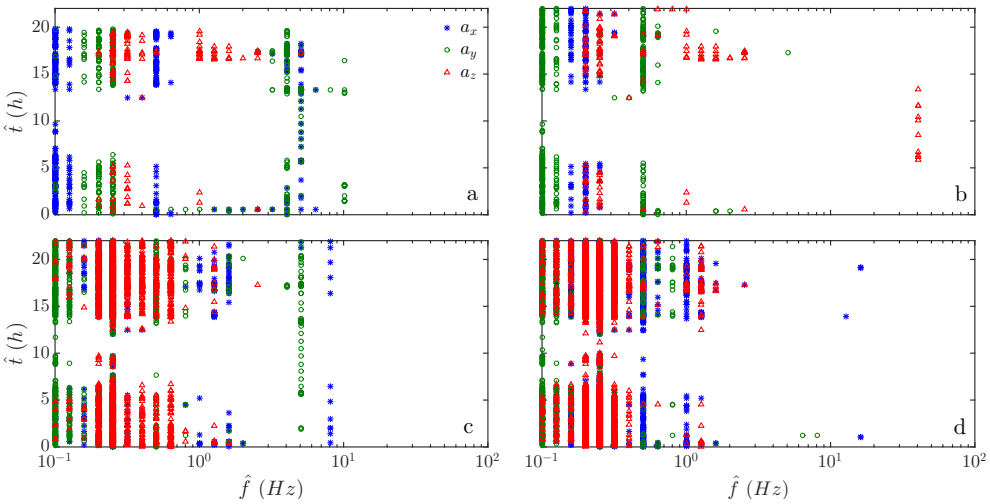

FIGURE 2.24: RMS warning map of S1 a, S2 b, S3 c and S4 d sensors, DCMIX3, Run 6. Symbols indicate when the RMS exceeds the ISS vibratory limit requirements

others sensors, high frequencies, between $50 - 100\ Hz$, governed the power distribution and might thus be linked to general machinery functioning.

Chapter 3

Fundamentals of the DCMIX experiments

3.1 Description of the experiment

DCMIX experimental setup is located in the MSG inside the european Destiny Module of the ISS. An array of cells (Soret cells) previously filled with the samples of the corresponding ternary system (or binary in the case of the companion cell), is located inside the Selectable Optical Diagnostic (SODI) facility (see Figure 3.1), used previously in the SODI-IVIDIL project [30].

FIGURE 3.1: DCMIX cell array mounted on the SODI [27]

Each Soret cell is a transparent rectangular cavity with dimensions $10 \times 5 \times 10\ mm$ with two opposite heated walls. The mixture has necessarily to be transparent, since a

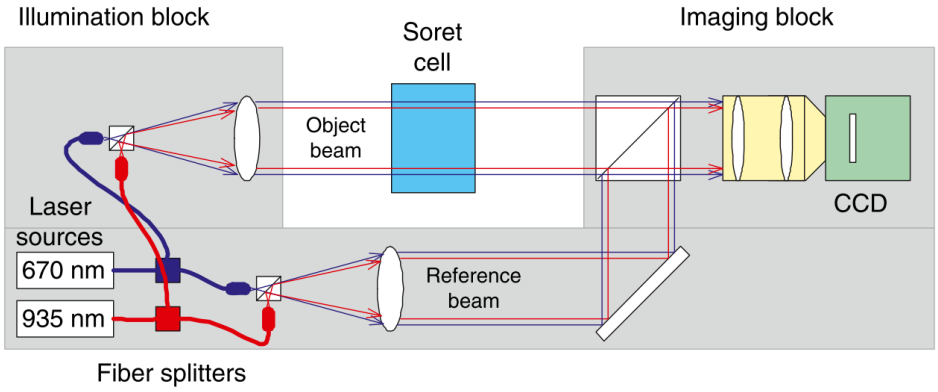

(A) Soret cell scheme

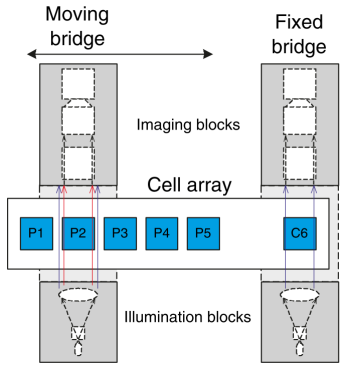

(B) Scheme of the cell array used in the DCMIX experiments

FIGURE 3.2: DCMIX experiments set up [88]

Mach-Zehnder Interferometer (MZI) is used for visualizing the concentration field [7]. The MZI apparatus projects two laser beams with different wavelengths, 670 nm and 935 nm across the sample in a direction perpendicular to the path between the two heated walls. A fringe pattern can be acquired as an image when the source wavelength is modified by fraction of a nanometre. These images, called "fringe images", are processed to calculate the corresponding concentration field.

The experimental procedure to perform a single DCMIX run can be divided into four well defined steps:

- **Step 1**: A thermal homogenisation needs to be performed to ensure an isothermal temperature field and an homogeneous concentration field as initial state for the experiment.

- **Step 2**: The two heated walls change their temperature applying a temperature difference $\Delta\hat{T} = \hat{T}_H - \hat{T}_C \neq 0$ across the sample, where $\hat{T}_H$ and $\hat{T}_C$ are the temperatures of the hot and cold wall, respectively. This temperature gradient creates

a linear temperature profile perpendicular to the laser beams. Since the characteristic thermal time $\hat{\tau}_T = \hat{L}^2/\hat{\alpha}$ is $\hat{\tau}_T \ll \hat{\tau}_D$, where $\hat{\alpha} \approx 10^{-7}\ m^2/s$ is the thermal diffusivity, the concentration field can be assumed as constant during the transition to the steady thermal state.

- **Step 3**: During this step $\Delta\hat{T} = \hat{T}_H - \hat{T}_C$, so after a time $\backsim\ \hat{\tau}_D$, a linear concentration profile driven by the linear temperature gradient is obtained. The temporal evolution of the concentration profile and the steady state are used to estimate both diffusion and thermodiffusion coefficients.

- **Step 4**: Once it is assumed the separation of the components has reached the steady state (sometimes this is debatable since theoretically, the steady state solution will be reached at $\hat{t} = \infty$), the temperature difference is set to $\Delta\hat{T} = 0$. As in step 2, due to the short period of time to reach isothermal conditions, it can be assumed that concentration does not change with time during this step.

- **Step 5**: Since during this step $\vec{\nabla}\hat{T} = 0$, a pure diffusive process takes place decreasing the concentration gradient. Therefore the diffusion coefficient matrix D_{ik} can be estimated again as an independent experiment.

Figure 3.3 depicts the thermodiffusion and pure diffusion steps (i.e. step 3 and 5). Once this process is finished, the experiment can be repeated on the same cell in case of any detected problem. If the imaging process concludes correctly, the moving bridge changes the position to the next cell in the cell array, and the process is repeated. The companion cell filled with the binary sample, is analysed independently using the fixed bridge to detect possible perturbations that could affect the measurements. This bridge mounts only one laser of 670 nm wavelength, since for a binary mixture only one mass transport equation is required to define the concentration field.

The experiment is based on the fact that the refractive index, $n(T, w_1, w_2)$ of the sample, is function of the temperature and the concentration [9]. In a ternary system, two equations are required to solve the concentration field, since there are only two independent mass fluxes (see Equation (1.1)). The variation of $\Delta n(T, w_1, w_2)$ all over the domain can be expressed as

$$\Delta n_1(x,y) = \left(\frac{\partial n_1}{\partial w_1}\right)_{\lambda_1} \Delta w_1(x,y) + \left(\frac{\partial n_1}{\partial w_2}\right)_{\lambda_1} \Delta w_2(x,y) + \left(\frac{\partial n_1}{\partial T}\right)_{\lambda_1} \Delta T(x,y), \quad (3.1)$$

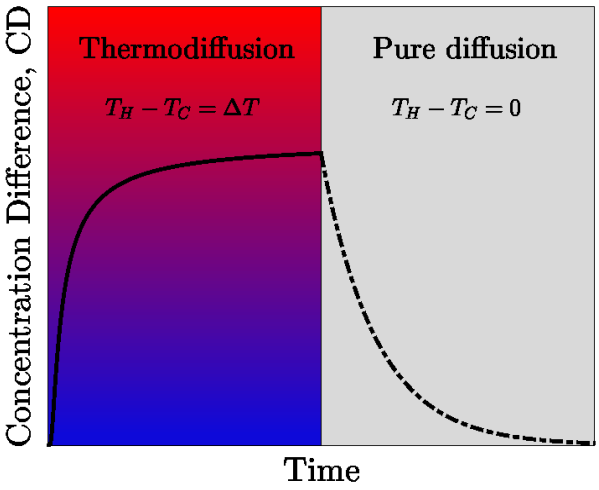

FIGURE 3.3: Sketch of steps 3 and 5 of a typical DCMIX experiment

$$\Delta n_2(x,y) = \left(\frac{\partial n_2}{\partial w_1}\right)_{\lambda_2} \Delta w_1(x,y) + \left(\frac{\partial n_2}{\partial w_2}\right)_{\lambda_2} \Delta w_2(x,y) + \left(\frac{\partial n_2}{\partial T}\right)_{\lambda_2} \Delta T(x,y), \quad (3.2)$$

where $\Delta T(x,y)$ and $\Delta w(x,y)$ are the temperature and concentration changes at point (x,y), respectively. The temperature $\left(\frac{\partial n}{\partial T}\right)_\lambda$ and concentration $\left(\frac{\partial n}{\partial C}\right)_\lambda$ contrast factors, represents the variation of the refractive index for each wavelength λ due to temperature and concentration, respectively. Although the contrast factors are function of temperature and composition, they are assumed to be constant for each mixture due to the small variation in temperature and concentration.

Since $\hat{\tau}_T \ll \hat{\tau}_D$ (for a DCMIX mixture $\hat{\tau}_T \approx 250\ s$), during step 2, the variation of concentration can be neglected. Thus, the temperature field can be obtained with both lasers as

$$\Delta T(x,y) = \frac{\Delta n_1(x,y)}{\left(\frac{\partial n_1}{\partial T}\right)_{\lambda_1}}, \quad (3.3)$$

$$\Delta T(x,y) = \frac{\Delta n_2(x,y)}{\left(\frac{\partial n_2}{\partial T}\right)_{\lambda_2}}. \quad (3.4)$$

Once the temperature field is known, the concentration field can be obtained by

solving the system

$$\begin{bmatrix}\Delta w_1(x,y)\\ \Delta w_2(x,y)\end{bmatrix} = \begin{bmatrix}\left(\frac{\partial n_1}{\partial w_1}\right)_{\lambda 1} & \left(\frac{\partial n_1}{\partial w_2}\right)_{\lambda 2}\\ \left(\frac{\partial n_2}{\partial w_1}\right)_{\lambda 1} & \left(\frac{\partial n_2}{\partial w_2}\right)_{\lambda 2}\end{bmatrix}^{-1} \begin{bmatrix}\Delta n_1(x,y) - \left(\frac{\partial n_1}{\partial T}\right)_{\lambda 1}\Delta T\\ \Delta n_2(x,y) - \left(\frac{\partial n_2}{\partial T}\right)_{\lambda 2}\Delta T\end{bmatrix}. \tag{3.5}$$

The measurement of the concentration contrast factors is very important for the correct estimation of the concentration field. The inverse of the concentration contrast factor matrix in the system (3.5) can be ill-conditioned, therefore small variations in the value of the concentration contrast factors (e.g. measurement errors) lead to large errors and consequently the calculated coefficients can be wrong [67].

3.2 Mathematical model

In the thermodiffusion experiments performed in microgravity conditions, the flow always remain in laminar regime, since the induced velocities are generally very small due to the weak buoyancy forces. Therefore, the viscous energy dissipation is neglected. The mixture is a non-reacting system, so there is no internal heat generation. The Boussinesq approximation is used to take into account the buoyancy forces, since the variation of density with concentration and temperature in the analysed range is linear [53]. The use of constant thermophysical values in this model relies on the fact that this values are obtained by means of experimental techniques (e.g. thermogravitational column and sliding symmetric tubes) that assume constant thermophysical values for a specific composition [52], therefore, constant values must be used. Furthermore, the variation of concentration in the analysed cases is $< 1\%$ and to the best of our knowledge, for such specific systems there are not available data of the variation of these properties with temperature, just values at room temperature for each specific composition.

Under the aforementioned assumptions, the thermodiffusive flow of a ternary incompressible mixture, under a non-uniform temperature field is governed by the following dimensionless continuity, momentum, mass transfer and energy equations

$$\frac{\partial u_j}{\partial x_j} = 0 \tag{3.6}$$

$$\begin{gathered}\frac{\partial u_i}{\partial t_i} + \frac{\partial u_j u_i}{\partial x_j} = -\frac{\partial p}{\partial x_i} + Sc\frac{\partial^2 u_i}{\partial {x_j}^2} + \\ Sc[Ra_{1i}\,(w_1 - w_{01}) + Ra_{2i}\,(w_2 - w_{02}) + Ra_{Ti}\,(T - T_0)]\end{gathered} \tag{3.7}$$

$$\frac{\partial w_1}{\partial t} + \frac{\partial u_j w_1}{\partial x_j} = \frac{\partial^2 w_1}{\partial {x_j}^2} + D_{12}\frac{\partial^2 w_2}{\partial {x_j}^2} + D_{T1}\frac{\partial^2 T}{\partial {x_j}^2} \tag{3.8}$$

$$\frac{\partial w_2}{\partial t} + \frac{\partial u_j w_2}{\partial x_j} = D_{21}\frac{\partial^2 w_1}{\partial {x_j}^2} + D_{22}\frac{\partial^2 w_2}{\partial {x_j}^2} + D_{T2}\frac{\partial^2 T}{\partial {x_j}^2} \tag{3.9}$$

$$\frac{\partial T}{\partial T} + \frac{\partial u_j T}{\partial x_j} = \frac{Sc}{Pr}\frac{\partial^2 T}{\partial {x_j}^2}, \tag{3.10}$$

respectively. Hereinafter, $x_1 = x$, $x_2 = y$ and $x_3 = z$.

To define the dimensionless variables, the distance between the hot and cold walls $\hat{L}$ has been chosen as the characteristic length, the pure diffusion coefficient of component 1, $\hat{D}_{11}$ is used as the characteristic time as $\hat{L}^2/\hat{D}_{11}$ and $\Delta\hat{T} = \hat{T}_{hot} - \hat{T}_{cold}$ is used as the characteristic temperature.

In Equation (3.7), $Sc = \hat{\nu}/\hat{D}_{11}$ is the Schmidt number and $Ra_{1i} = \beta_1 \hat{L}^3 \hat{g}_i\left(\hat{t}\right)/\hat{\nu}\hat{D}_{11}$, $Ra_{2i} = \beta_2 \hat{L}^3 \hat{g}_i\left(\hat{t}\right)/\hat{\nu}\hat{D}_{11}$ and $Ra_{Ti} = \hat{\beta}_T \hat{L}^3 \hat{g}_i\left(\hat{t}\right)\Delta\hat{T}/\hat{\nu}\hat{D}_{11}$ are the two solutal and thermal Rayleigh numbers respectively. $\hat{g}_i\left(\hat{t}\right)$ is the acceleration field acting in the cavity as a function of time, and $\hat{\nu}$ is the kinematic viscosity. The values β_1, β_2 and $\hat{\beta}_T$ involved in the buoyancy term, are the expansion factor related with the variation in concentration of component 1 and 2, and temperature respectively. Using β_1, β_2 and $\hat{\beta}_T$, the linear variation of the density can be expressed as,

$$\hat{\rho} = \hat{\rho}_0\{1 + \beta_{w1}\left(w_1 - w_{01}\right) + \beta_{w2}\left(w_2 - w_{02}\right) - \hat{\beta}_T\left(\hat{T} - \hat{T}_0\right)\}, \tag{3.11}$$

where $\hat{T}_0$ is the reference temperature and $\hat{\rho}_0$ is the average density.

The non-dimensional diffusion matrix is defined as $\hat{D}_{ik}/\hat{D}_{11}$,

$$D_{ik} = \begin{pmatrix} 1 & D_{12} \\ D_{21} & D_{22} \end{pmatrix}. \tag{3.12}$$

In Equation (3.8), $D_{Ti} = \hat{D}_{Ti}\Delta\hat{T}/\hat{D}_{11}$, is the the thermodiffusion coefficient and the Prandtl number defined as $Pr = \hat{\nu}/\hat{\alpha}$ is also used in Equation (3.9).

The domain used in the calculations is a rigid parallelepiped cavity (see Figure 3.4) with two opposite heated walls with a difference temperature $\Delta\hat{T} \neq 0$ for the thermodiffusion step and $\Delta\hat{T} = 0$ for the pure diffusion step. The cavity has the same dimensions as the Soret cell used in the actual DCMIX experiments ($\hat{L} = 5\ mm$).

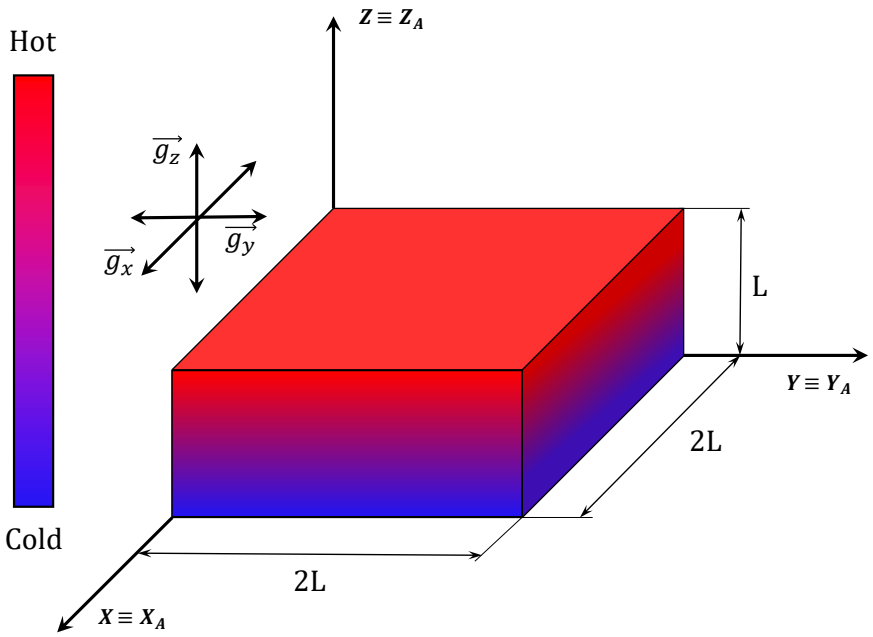

FIGURE 3.4: Sketch of the Soret cell. System of reference for simulations (x, y and z) and its equivalence with the ISS absolute coordinate system (x_A, y_A and z_A)

No-slip impermeable boundary conditions for velocity are imposed at the six walls of the domain,

$$u_i\left(t, x_i\right) = 0, \qquad x_i \in \Omega_w \qquad \forall t \geq 0 \qquad i = 1, 2, 3, \tag{3.13}$$

where Ω_w is the surface of all the walls of the domain. Regarding the concentration, zero mass flux through the adiabatic walls,

$$\frac{\partial w_j\left(t, x_k\right)}{\partial x_i} = 0, \quad x_k \in \Omega_{adia,i} \quad \forall t \geq 0 \quad i = 1, 2 \quad j = 1, 2 \quad k = 1, 2, 3, \tag{3.14}$$

is used as boundary condition, where $\Omega_{adia,i}$ are the adiabatic walls perpendicular to x_i direction. Non-homogeneous Neumann boundary conditions are imposed on the heated walls,

$$\frac{\partial w_j\left(t, x_k\right)}{\partial x_i} = -S_{Tj}\frac{\partial T\left(t, x_k\right)}{\partial x_i}, \quad x_i \in \Omega_{T,i} \quad \forall t \geq 0 \quad i = 3 \quad j = 1, 2 \quad k = 1, 2, 3, \tag{3.15}$$

where $\Omega_{T,i}$ are the heated walls perpendicular to x_i direction and S_{Tj} is the Soret coeffi-

cient.

For the energy equation, again homogeneous Neumman boundary conditions are used for the adiabatic walls,

$$\frac{\partial T\left(t, x_i\right)}{\partial x_i} = 0, \qquad x_i \in \Omega_{adia,i} \qquad \forall t \geq 0, \qquad i = 3. \tag{3.16}$$

Initially, the fluid is assumed to be at rest,

$$u_i\left(t = 0, x_i\right) = 0, \qquad \forall x_i \qquad i = 1, 2, 3. \tag{3.17}$$

The boundary conditions for temperature at the heated walls, and the initial conditions for temperature and concentration depend on the step of the experiment (i.e. thermodiffusion or pure diffusion step).

3.2.1 Thermodiffusion step

Here the thermodiffusion step has been modelled as started right after the thermal homogenisation step. Thus, the initial condition for temperature is

$$T\left(x_i, t = 0\right) = \frac{1}{2}, \qquad \forall x_i \qquad i = 1, 2, 3. \tag{3.18}$$

An homogeneous concentration field associated with the isothermal temperature field is the initial condition for both components,

$$w_j\left(x_i, t = 0\right) = w_{0j}, \qquad \forall x_i \qquad i = 1, 2, 3 \qquad j = 1, 2. \tag{3.19}$$

Dirichlet boundary conditions are applied at the heated walls, to set both walls at two different temperatures,

$$T\left(x_i, t\right) = 1, \qquad x_i \in \Omega_{hot} \qquad \forall t \geq 0 \qquad i = 1, 2, \tag{3.20}$$

$$T\left(x_i, t\right) = 0, \qquad x_i \in \Omega_{cold} \qquad \forall t \geq 0 \qquad i = 1, 2. \tag{3.21}$$

3.2.2 Pure diffusion step

The pure diffusion step starts once the thermodiffusion step has finished and the temperature difference between the heated walls is set to $\Delta T = 0$. So, in this case the same Dirichlet boundary condition is used at both walls,

$$T\left(x_i, t\right) = \frac{1}{2}, \qquad x_i \in \Omega_{hot}, \Omega_{cold} \qquad \forall t \geq 0 \qquad i = 1, 2. \tag{3.22}$$

An isothermal temperature field can be assumed as initial condition for temperature, since $\tau_t \ll \tau_D$,

$$T\left(x_i, t = 0\right) = \frac{1}{2}, \qquad \forall x_i \qquad i = 1, 2, 3. \tag{3.23}$$

Again the fluid is considered at rest, so the initial condition for velocity is,

$$u_i\left(x_i, t = 0\right) = 0, \qquad \forall x_i \qquad i = 1, 2, 3. \tag{3.24}$$

During the thermodiffusion step, the resulting steady state linear temperature profile between the heated walls promotes, due to the Soret effect, also a linear concentration profile. Therefore, the steady state concentration profile of the thermodiffusion step, has been used as initial condition for the concentration field in this step,

$$w_j\left(x_i, t = 0\right) = -S_{Tj} x_i + w_{0,j} + \frac{S_{Tj}}{2} \qquad \forall x_i \qquad i = 3 \qquad j = 1, 2. \tag{3.25}$$

3.3 The CFD tool (OpenFOAM)

To solve numerically the governing Eqs. (3.6) to (3.10) with the corresponding initial and boundary conditions, the open source Computational Fluid Dynamics (CFD) software Open Source Field Operation and Manipulation (OpenFOAM) v2.3.0, which uses the C++ programming language, has been used in this study. OpenFOAM takes advantage of the object oriented programming features of C++ to offer a very efficient way for expressing mathematical abstract concepts. The *applications* included in OpenFOAM can be divided into two categories: *solvers*, which use the Finite Volume Method [100] to

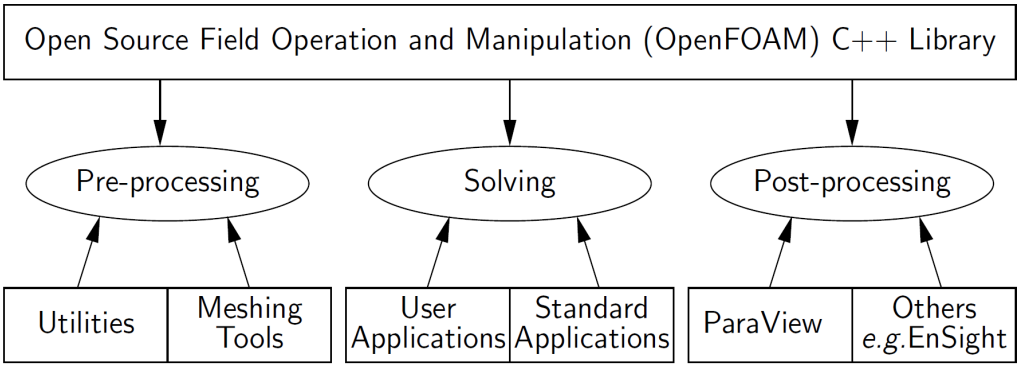

FIGURE 3.5: General structure of the OpenFOAM software [2]

discretize the equations for solving a specific continuum mechanics problem, and *utilities*, designed for a wide variety of pre- and post-processing tasks. Figure 3.5 shows the structure of the OpenFOAM software.

The standard *solvers* implemented in the native OpenFOAM installation cover a wide spectra of problems, like potential flow, in/compressible flow, multiphase flow, Direct Numerical Simulation (DNS), combustion, heat transfer and buoyancy-driven flows, particle-tracking flows, molecular dynamics problems, direct Monte Carlo simulations, stress analysis of solids and Finance problems [2]. As an open source, the user has access to the source code and can modify it to create or customize his own *solvers*/*utilities*. Unfortunately, OpenFOAM does not include any standard *solver* for thermodiffusion in ternary systems under microgravity conditions. Thus, a custom *solver* called `thermoGFoam` has been created to this purpose.

3.3.1 Customized solver: *thermoGFoam*

When a new *solver* has to be created, a good starting point is using an existing one and adding the missing terms of the new problem. For this problem, the standard *solver* `buoyantBoussinesqPimpleFoam` for transient buoyant, turbulent/laminar flows of incompressible fluids has been chosen as an initial step.

The solver `buoyantBoussinesqPimpleFoam` solves the incompressible Navier-Stokes equations, where a constant gravity value is used for computing the buoyancy term related with the change in temperature, together with the energy equation. The coupling pressure-velocity is solved using the *PIMPLE* algorithm, a combination of *SIMPLE* [75] and *PISO* [38] algorithms. So, the mass transport equations of component 1 and 2 (Eqs. (3.8) and (3.9)) and the compositional buoyancy terms for both components in the momentum equation (3.7) had to be added in the custom solver (see Figure 3.6). In

order to reproduce the microgravity environment which the gravity is a function of time $\vec{g}(t)$, the *solver* has to read an external file `gravity` that includes the gravity values for each time step in the x, y and z-direction.

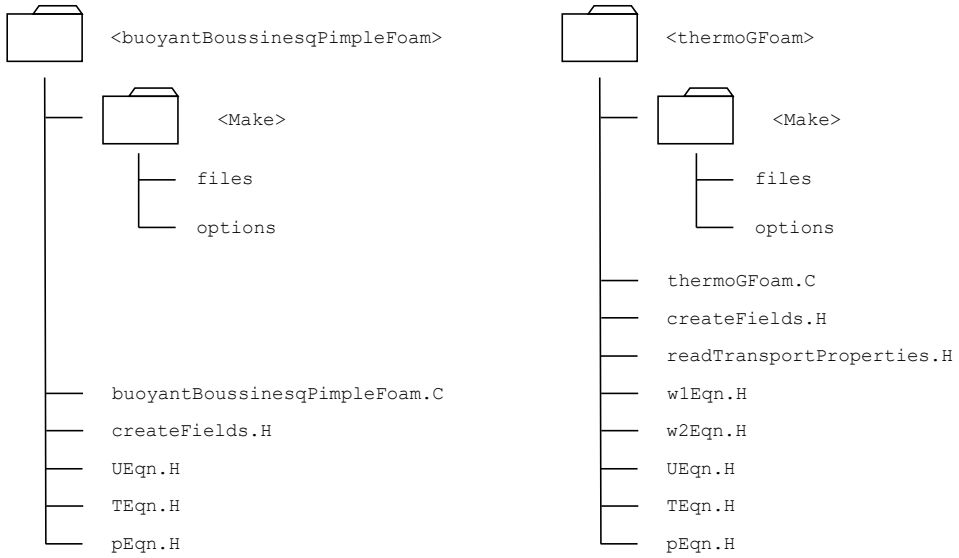

FIGURE 3.6: OpenFOAM *solver* structure comparison between the base and the customized one

Due to the particular nature of the boundary conditions for concentration at the heated walls (see Equation (3.15)), the source code needs to be modified, since the standard boundary conditions can not address such a specific condition. Fortunately, OpenFOAM capabilities can be enhance with an additional toolbox called `swak4Foam` (`swak` stands for Swiss Army Knife), that combine the functionality of `groovyBC` and `funkysetfields`. The former allows to implement sophisticated boundary conditions by just modifying the case setup, without any source code modification, while the latter is used to create very specific scalar or vector fields, as initial conditions. The source code of the customized *solver* and a typical case is shown in Appendices C and D respectively.

One of the most powerful capabilities of OpenFOAM is that allows the selection of many different discretization schemes. The user can use a different scheme for each term simply by using the corresponding key words in the case set up. In this study the mass, momentum and energy diffusive fluxes and the momentum and energy convective terms are discretized with a second-order centered scheme while the mass advection terms are discretized with a TVD scheme. The momentum, mass transfer equations and energy equations are integrated in time using a Crank-Nicolson scheme. The results have been compared with the ones obtained with an in-house code used in [73] showing a good agreement.

Chapter 4

Effect of the reboostings on the determination of the diffusion and Soret coefficients onboard the ISS

4.1 Thermodiffusion step

In this section the impact of different reboostings accelerometric scenarios on the DCMIX1 experiment has been analysed by reproducing the experimental method for calculating the diffusion coefficients. To this end, the physical and mathematical model described in Chapter 3 has been solved numerically.

4.1.1 Characteristics of the studied cases

DCMIX European Space Agency's (ESA) project, counts with four campaigns, DCMIX1, DCMIX2, DCMIX3 and DCMIX4. DCMIX4 campaign has been recently carried out, so the values of the coefficients are not available at the present time. Several groups participate in the project, and so, different techniques for measuring the physical properties are used both on Earth and orbital laboratories. The disparity of the methods used and the difficulty of measuring thermophysical properties of ternary systems on Earth laboratories, make difficult to reach an agreement in the value of all the thermophysical properties. Sometimes different studies give even different signs for cross and thermodiffusion coefficients. It is also very rare to find a study in which a complete listing of the thermophysical properties for a certain composition is given. The disagreement of the

results, together with the scattering of the properties along the related studies, make difficult to obtain a questionless set of parameters to perform the simulations.

The order in which the components are numbered for the same mixture and composition is sometimes different depending on the reference. For certain experimental techniques it is more useful to use as independent components the two heaviest components, while for some others, is more convenient to take the heaviest and the lightest. Because the diffusion matrix and the thermodiffusion coefficients depend on the order of numeration, it is very important to be consistent with the numbering of the two independent components. Therefore, the following order of numeration has been used in this study:

- DCMIX1.- Component 1: THN, component 2: IBB and component 3: nC_{12}
- DCMIX2.- Component 1: Tol, component 2: Meth and component 3: Ch
- DCMIX3.- Component 1: TEG, component 2: Water and component 3: Eth

Here, the two independent components are always component 1 and component 2. For the numerical simulations the numeration of the components is not relevant, the only thing that has to be kept in mind is the consistency of the choice with the value of the thermodiffusion and diffusion coefficients.

For the time being, the required thermophysical properties for simulating the DCMIX4 systems are not available. Therefore, DCMIX4 has not be analysed in this thesis. The set of properties required for the simulations in each DCMIX campaign and references where they can be found are summarized in Table 4.1. The value of the thermal diffusivity is not reported in the literature, and a value of $\hat{\alpha} = 10^{-7} m^2/s$ has been used as a typical value for all cases [45].

	Composition	$\hat{\rho}$ (kg/m^3)	$\hat{\nu}$ ($10^{-7}\ m^2/s$)	β_T ($10^{-3}\ K^{-1}$)	β_1	β_2	$\hat{D}_{11}$ ($10^{-9}\ m^2/s$)	$\hat{D}_{12}$ ($10^{-9}\ m^2/s$)	$\hat{D}_{21}$ ($10^{-9}\ m^2/s$)	$\hat{D}_{22}$ ($10^{-9}\ m^2/s$)	$\hat{D}_{T1}$ ($10^{-13}\ m^2/sK$)	$\hat{D}_{T2}$ ($10^{-13}\ m^2/sK$)	$\hat{S}_{T1}$ ($10^{-3}\ K^{-1}$)	$\hat{S}_{T2}$ ($10^{-3}\ K^{-1}$)	Reference
DCMIX1	0.10-0.10-0.8	771.952	17.002	0.954	0.2376	0.1220	1.06	-0.031	-0.267	0.822	5.0	2.6	0.49	0.47	[43]
	0.10-0.80-0.10	847.296	12.428	0.947	0.2692	0.1449	1.04	-0.047	-0.168	0.957	3.4	1.4	0.34	0.21	[43]
	0.45-0.10-0.45	841.862	17.105	0.900	0.2582	0.1372	0.756	0.001	-0.138	0.682	13.4	0.7	1.77	0.46	[43]
	0.80-0.10-0.10	925.440	18.575	0.848	0.2838	0.1567	0.578	-0.113	-0.039	0.695	7.3	-2.8	1.2	-0.34	[43]
DCMIX2	0.62-0.31-0.07	829.99‡	6.6989‡	1.1568§	0.1368‡	0.0449‡	2.30§	1.52§	-0.24§	0.51§	-6.806	-6.841	0.445†	-1.122†	[34, 51, 67]
DCMIX3	0.15-0.25-0.60	894.784‡	29.001‡	0.9474‡	0.3050‡	0.2891‡	0.598	0.056	-0.407	0.234	-1.06‡	4.36‡	-0.302	1.337	[51, 56]
	0.33-0.33-0.33	975.479‡	44.337‡	0.8239‡	0.3461‡	0.2741‡	0.458	-0.014	-0.155	0.321	-1.74‡	3.67‡	-0.377	0.961	[51, 56]

†Values taken from [67]
‡Values taken from [51]
§Values taken from [34]

TABLE 4.1: Thermophysical properties of the mixtures analysed in each DCMIX campaign

4.1.2 Spatial discretization verification

Different uniform meshes have been tested to obtain a good compromise between the spatial accuracy and the computing cost of the simulations. In Table 4.2, the number

Mesh	$\mathbf{N_x}$	$\mathbf{N_y}$	$\mathbf{N_z}$	**Time required for simulating 2.778 h of experiment** (h)
M20	20	20	10	0.525
M30	30	30	15	1.341
M40	40	40	20	3.765
M50	50	50	25	10.507
M60	60	60	30	20.347

TABLE 4.2: Mesh configuration used for testing the validity of the spatial discretization

of cells, together with the time spent for performing a simulation with each mesh are shown.

The DCMIX2 case has been chosen for analysing the spatial discretization verification, since after some simulations it resulted in the most distorted case. A value of acceleration ($\hat{a}_x = 10^{-1}\ m/s^2$) in the x-direction (perpendicular to the concentration and temperature gradients), larger than the module of the highest peak found in the real acceleration signal ($\bar{\hat{a}} \approx 2 \cdot 10^{-2}\ m/s^2$) has been used as a constant gravity field, to ensure the worst gravity scenario.

Figure 4.1 shows the concentration difference (CD), as a function of time, $CD(t)$, for the five different meshes used. The CD is defined as the difference in concentration between the hot and cold walls of the Soret cell. It can be seen that mesh M40 reproduces accurately the transient until the steady state is reached. The difference in the steady state $CD(t)$ value between meshes M40 and M60 is only 1.2%, and hence mesh M40 has been chosen for the calculations, since it exhibits a good compromise between accuracy and computational cost.

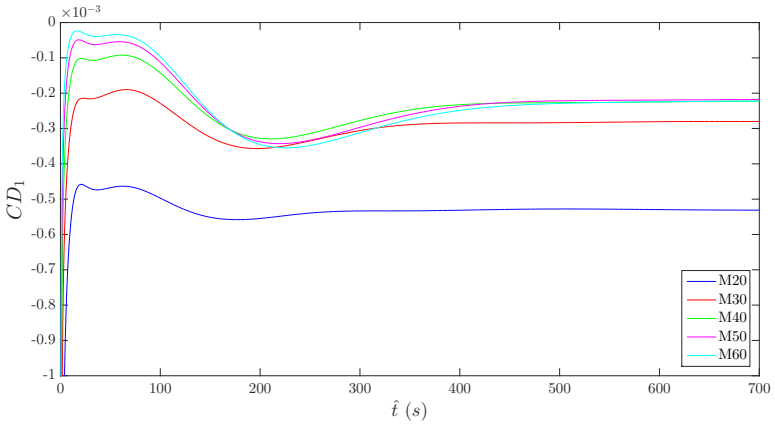

FIGURE 4.1: Concentration difference, CD, of component one as a function of time for each mesh

4.1.3 Accelerometric environment

As it has been stated before, regular reboostings are needed to overcome the effects of residual atmospheric drag which makes the ISS lose about 100 m in altitude per day. These reboostings easily exceed the ISS vibratory limits requirements [42]. The different spacecrafts in charge of the reboosting manoeuvres, Progress, Space Shuttle, Soyuz, Zvezda, and Automated Transfer Vehicle (ATV), produce different intensities, durations and footprints in the acceleration signal [60]. For instance, during 19^{th} of June 2008 a reboosting manoeuvre provided an increment of velocity $\Delta\hat{V} = 4.05\ m/s$. The thrust generated by two of the ATV's four main engines lasted $\backsim 20\ min$. The intensity of this reboosting lifted the altitude of the ISS by around 7 km, surpassing the largest reboosting to date performed on the 25^{th} of April 2008, which was less powerful with an increment of velocity $\Delta\hat{V} = 2.6\ m/s$ [1]. Thus, this most intense reboosting has been chosen as the accelerometric environment for the simulations. In this way, it is guaranteed that the most adverse accelerometric scenario is analysed.

Reboosting produces a larger thrust intensity in the x-direction according to the absolute reference system of the ISS (which is also the x-direction of the local reference system for the simulations, see Figure 3.4). This acceleration signal has been introduced perpendicular to the temperature gradient, not only because is the actual direction of the reboosting, but also because in [43], it was concluded that the most harmful orientation of the experiment during a reboosting, occurs when the concentration gradient is perpendicular to the direction of the thrust force.

The acceleration signal of the reboosting, has been split in five different signals as it can be seen in Figure 4.2. These five signals simulate a reboosting starting at different stages of the experiment. The signals have been named as Beginning1, Beginning2, Middle1, Middle2 and End, representing the time of the experiment in which the reboosting occurs. Figure 4.2b shows an apparently larger acceleration in the y-direction than in the x-direction. This is due to high amplitude peaks in the y-direction but since they are very short in time the average value of the signal in the x-direction is one order of magnitude larger.

Two additional simulations have been performed with the DCMIX2 mixture assuming the steady state of the thermodiffusion step as initial conditions. Therefore, the initial conditions correspond to the analytical solution of the DCMIX2 at $\hat{t} = 2.5 \cdot 10^4\ s$ (end of the thermodiffusion step). In this point the density gradient is maximum, and consequently any acceleration would have a larger impact on the system. One of the simulations has been performed introducing the reboosting at the beginning and the other one using a quiescent period signal. In this way the time required to restore the analytical

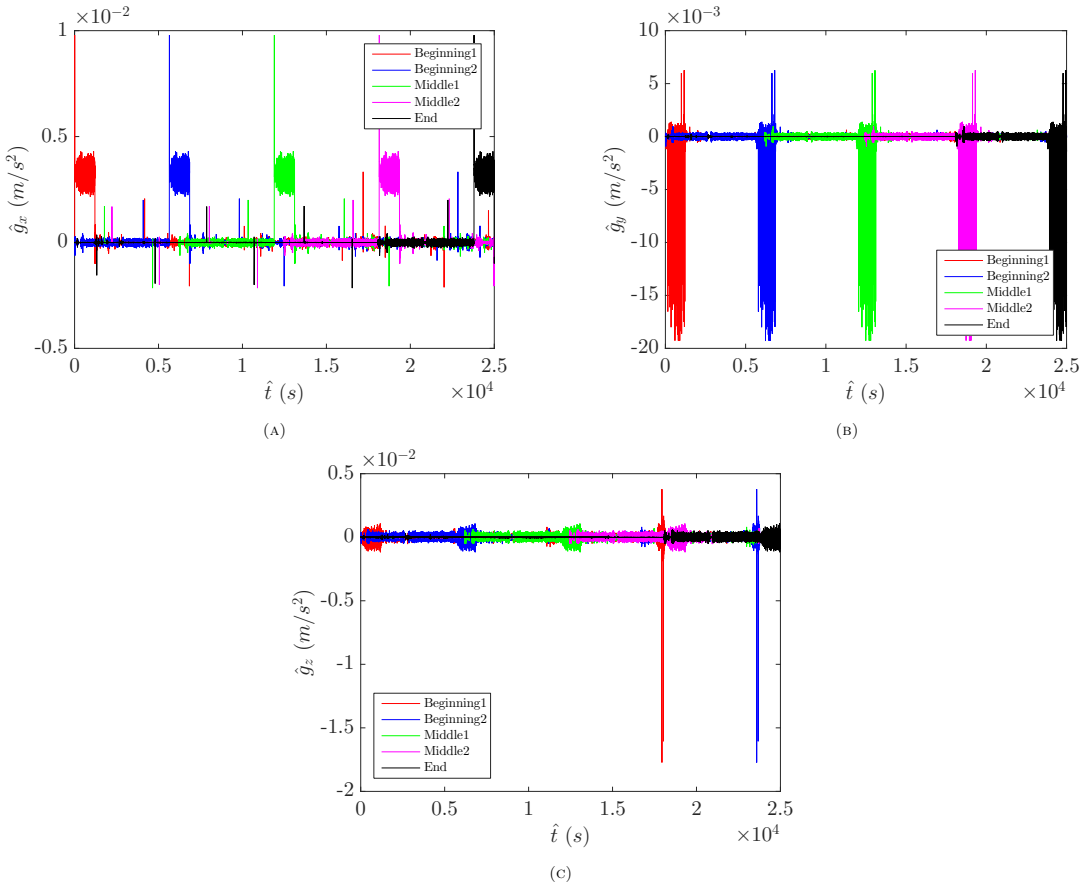

FIGURE 4.2: Accelerations caused by the reboosting in x (a), y (b) and z (c) directions

steady state solution can be calculated.

Table 4.3 summarizes the composition of the selected mixtures and the accelerometric conditions of the twenty simulations used for evaluating the impact of the reboosting.

The acceleration used in all the simulations is recorded by the OSSRAW sensor which has a sample frequency of 10 Hz, so the timestep used in all simulations was set to $\Delta\hat{t} = 10^{-1}\ s$ to match the sampling rate of the sensor. The value of the timestep, is small enough to ensure a Courant number below one during the whole simulation due to the low magnitude of the induced velocity inside the cell.

4.1.4 Results

This section presents the effect of the reboosting on the concentration field and the error obtained in the calculation of the Soret coefficient, if the DCMIX experiments were performed during a reboosting. Equation (4.1) has been used to calculate the Soret coefficient at $\hat{t} = 2.5 \cdot 10^4\ s$ and subsequently calculate the error caused by the reboosting.

Experiment	**Composition**	**Acceleration applied**	**Simulation time**
DCMIX1	0.45-0.10-0.45	Zero gravity	$2.5 \cdot 10^4$ s
		Beginning1	
		Beginning2	
		Middle1	
		Middle2	
		End	
DCMIX2	0.62-0.31-0.07	Zero gravity	$2.5 \cdot 10^4$ s
		Beginning1	
		Beginning2	
		Middle1	
		Middle2	
		End	
		Reboosting at the steady state	$5 \cdot 10^4$ s
		Quiescent period at the steady state	$5 \cdot 10^4$ s
DCMIX3	0.15-0.25-0.60	Zero gravity	$2.5 \cdot 10^4$ s
		Beginning1	
		Beginning2	
		Middle1	
		Middle2	
		End	

TABLE 4.3: Summary of the acceleration signals used in each simulation

In addition, the impact of the reboosting once the steady state has been reached has also been studied.

4.1.4.1 Concentration profile

Figure 4.3 shows the temporal evolution of the numerically predicted concentration profiles in the z-direction (the direction of the thermal gradient) of component 1, $w_1(\hat{t}, \hat{x} = \hat{y} = 0.005\ m, \hat{z})$, during a reboosting together with the analytical solution (Figures 4.3a.1, 4.3b.1 and 4.3c.1, see Appendix A [69]). Although the governing equations have been written in dimensionless form, the presented results use dimensional length and time for the sake of clarity when comparing the three different systems. These results correspond to the five different reboosting scenarios (Beginning1, Beginning2, Middle1, Middle2 and End) applied to the DCMIX1, DCMIX2 and DCMIX3 mixtures (see Table 4.3). The shape of the initial concentration in all cases (black solid line at $\hat{t} = 0\ s$) is a straight line, since initially, the concentration of all components is homogeneous in the whole domain. The black dashed line represents the concentration profile at time $\hat{t}_{end} = 2.5{\cdot}10^4\ s$, and the magenta markers refer to the value of concentration at hot and cold walls ($\hat{z} = 0.005\ m$ and $\hat{z} = 0\ m$).

The locus $w_1(\hat{t}, \hat{x} = \hat{y} = 0.005\ m, \hat{z})$ is more distorted when the thermodiffusion flux has created a large enough component separation, and therefore a large enough density gradient. On the contrary, the Beginning1 scenario, barely affects the concentration profile of the three DCMIX systems (see Figures 4.3a.2, 4.3b.2 and 4.3c.2).

The only mechanism that can induce convection in the system is the buoyancy force and the viscous force is the only one that can dissipate the kinetic energy of the fluid. Thus, the ratio between these two forces, known as Grashof number, is the parameter that determines which system is more sensitive to an acceleration field. In a ternary thermodiffusive system, one can define three different Grashof numbers. The solutal Grashof numbers $Gr_{1i} = \beta_1 \hat{L}^3 \hat{g}_i(\hat{t})(w_1 - w_{01})/\hat{\nu}^2$ and $Gr_{2i} = \beta_2 \hat{L}^3 \hat{g}_i(\hat{t})(w_2 - w_{02})/\hat{\nu}^2$ and the thermal Grashof number, $Gr_T = \hat{\beta}_T \hat{L}^3 \hat{g}_i(\hat{t})(\hat{T} - \hat{T}_{01})/\hat{\nu}^2$. In Figure 4.4, it is shown the three Grashof numbers Gr_1, Gr_2 and Gr_T and the sum of them as a function of $\hat{z}$, which can be considered as the overall buoyancy term for each DCMIX system at time $\hat{t} = 6 \cdot 10^3\ s$, just before the reboosting in the Beginning2 scenario. It can be seen how the solutal Grashof Gr_1 and Gr_2 have similar values in all DCMIX systems. The thermal Grashof Gr_T is larger than the solutal ones in DCMIX1 and especially in DCMIX2, and therefore, the value of the buoyancy term is dominated by Gr_T in these cases. The larger value of the buoyancy term in DCMIX2 and the smaller value in DCMIX3 match the

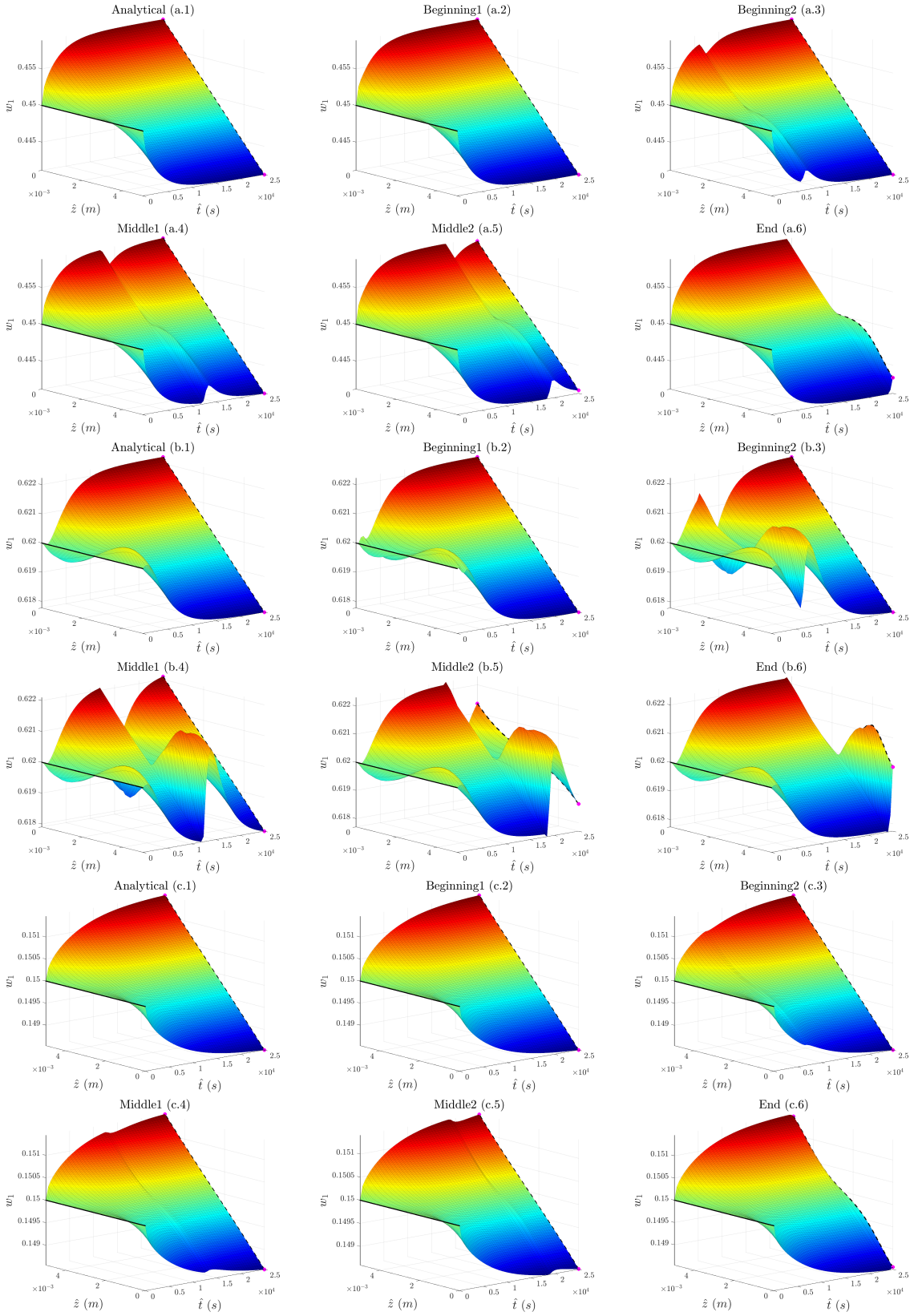

FIGURE 4.3: Locus of the analytical and numerical $w_1(\hat{t}, \hat{z})$ in DCMIX1, a), DCMIX2, b) and DCMIX3, c)

larger and smaller distortion observed respectively in the concentration field represented in Figure 4.3.

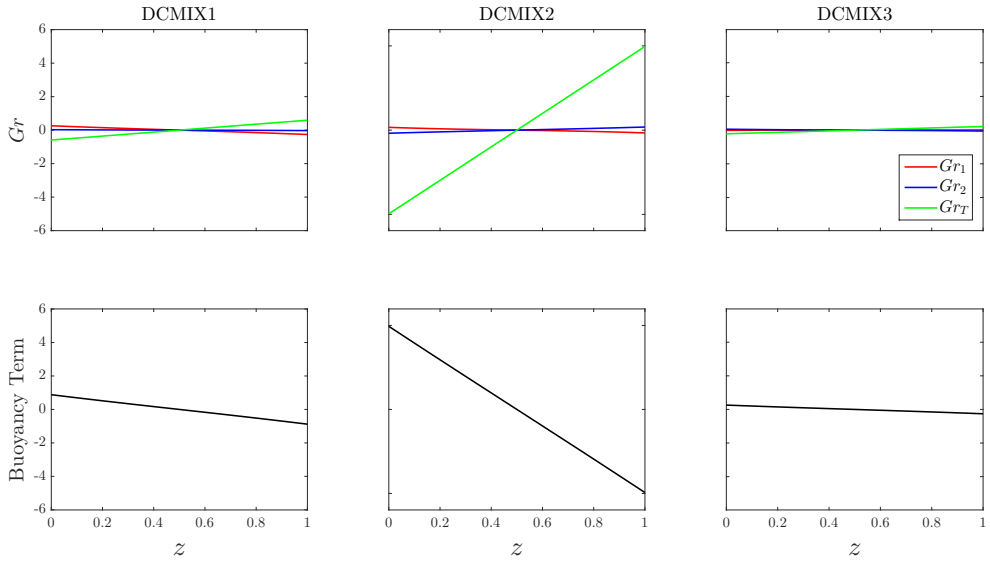

FIGURE 4.4: Concentration, Gr_1 and Gr_2, thermal Gr_T Grashof numbers and the value of the buoyancy term as a function of the z-direction at time $\hat{t} = 6 \cdot 10^3$ s ($\hat{g} = 0.0031$ m/s^2) for DCMIX1, DCMIX2, and DCMIX3

4.1.4.2 Error of the Soret coefficients

To follow the procedure used in [8] and [28] for calculating the Soret coefficients, S_{Ti}, from the experimental measurements, the expression

$$S_{Ti} = -\frac{CD_i^{SteadyState}}{\Delta T}, \qquad i = 1, 2, \tag{4.1}$$

has been used. Thus, the CD, at the end of the thermodiffusion step, $CD_i(t_{end})$, for each component needs to be determined. The analytical value of the CD is defined as

$$CD_{i,a}(t) = w_i(t, z = 1) - w_i(t, z = 0), \qquad i = 1, 2, \tag{4.2}$$

whereas the numerical value of CD has been obtained in two ways. In the first one, the averaged value $CD^1_{i,n}(t)$ on the hot and cold walls, has been obtained as

$$CD^1_{i,n}(t) = \overline{w_i}(t, x, y, z = 1) - \overline{w_i}(t, x, y, z = 0), \qquad i = 1, 2, \tag{4.3}$$

where i refers to component 1 and 2, and $\overline{w_i}$ corresponds to the averaged value of concentration of component i on the corresponding wall. The second way for calculating the $CD^2_{i,n}(t)$, is by using the local value at hot and cold walls along the line $x = y = 1$

$$CD^2_{i,n}(t) = w_i(t, x = y = z = 1) - w_i(t, x = y = z = 0), \qquad i = 1, 2, \tag{4.4}$$

Table 4.4 shows the theoretical value of S_{Ti} at $t = \infty$, together with the analytical and numerical predictions at $\hat{t}_{end} = 2.5 \cdot 10^4\ s$. To be as accurate as possible, the numerical error has been eliminated from the numerical simulations assuming that this error is constant over the whole simulation, so the error ε_{num} when solving Equations (3.6)-(3.10) numerically has been calculated as

$$\varepsilon_{num} = \frac{S_{Ti}^{t_{end}} - S_{Ti}^{G0}}{S_{Ti}^{t_{end}}} \cdot 100, \tag{4.5}$$

where S_{Ti}^{G0} and $S_{Ti}^{t_{end}}$ are the values of the Soret coefficient obtained with a simulation with $g_i = 0$ and from the analytical solution respectively.

Table 4.5 shows the error caused by the reboosting when the Soret coefficient S_{Ti} is calculated using the Equation (4.1). The error that each reboosting scenario can produce is defined as

$$\varepsilon_{B1,B2,M1,M2,E} = \frac{S_{Ti}^{B1,B2,M1,M2,E} - S_{Ti}^{t_{end}}}{S_{Ti}^{t_{end}}} \cdot 100 + \varepsilon_{num}, \tag{4.6}$$

where subscripts B1, B2, M1, M2 and E, correspond to reboosting applied at the Beginning1, at the Beginning2, at the Middle1, at the Middle2 and at the End respectively. All the numerical values of S_{Ti} have been obtained using both Equations (4.3) and (4.4).

It can be seen in Table 4.5 how the DCMIX2 mixture is the one that exhibits the largest error and the DCMIX1 the smallest one. This is in agreement with the distortion of the concentration fields shown in Figure 4.3 and discussed above. As it was expected, the error increases as the reboosting occurs closer to the instant of measuring the CD in all DCMIX mixtures, since the method used considers $CD_i(t_{end})$ for calculating the Soret coefficient. Thus, the largest error arises when the End reboosting scenario is applied. To better analyse the error ε as a function of the time when the reboosting takes place, it has been plotted for both components and all accelerometric scenarios in Figure 4.5. The closer to the measuring point the reboosting occurs, the larger the error ε is. Also, the error ε, is systematically larger when Equation (4.4) is used for calculating the CD.

		$S_{Ti_{t=\infty}}$ (10^{-4})	$S_{Ti_{t=t_{end}}}$ (10^{-4})	$S^1_{Ti_{G0}}$ (10^{-4})	$S^2_{Ti_{G0}}$ (10^{-4})	ε^1_{num} (10^{-4})	ε^2_{num} (10^{-4})	$S^1_{Ti_{B1}}$ (10^{-4})	$S^2_{Ti_{B1}}$ (10^{-4})	$S^1_{Ti_{B2}}$ (10^{-4})	$S^2_{Ti_{B2}}$ (10^{-4})	$S^1_{Ti_{M1}}$ (10^{-4})	$S^2_{Ti_{M1}}$ (10^{-4})	$S^1_{Ti_{M2}}$ (10^{-4})	$S^2_{Ti_{M2}}$ (10^{-4})	$S^1_{Ti_E}$ (10^{-4})	$S^2_{Ti_E}$ (10^{-4})
DCMIX1	w_1	17.719	17.711	17.711	17.711	-5.873	-5.873	17.710	17.710	17.698	17.698	17.596	17.597	16.922	16.837	14.856	13.454
	w_2	4.162	4.591	4.591	4.519	-44.925	4.590	4.590	4.590	4.568	4.568	4.455	4.452	4.050	3.949	3.961	3.712
DCMIX2	w_1	4.449	4.443	4.444	31.556	31.556	4.443	4.443	4.443	4.411	4.412	4.192	4.191	2.845	2.671	1.634	0.035
	w_2	-11.220	-11.213	-11.213	-11.213	8.640	8.640	-11.213	-11.213	-11.180	-11.181	-10.956	-10.955	-9.539	-9.361	-4.801	-1.558
DCMIX3	w_1	-3.025	-2.932	-2.931	-2.931	-94-509	-94.509	-2.931	-2.931	-2.921	-2.921	-2.891	-2.887	-2.819	-2.795	-2.830	-2.819
	w_2	13.371	12.909	12.907	-103.261	12.907	12.907	12.907	12.907	12.860	12.858	12.718	12.697	12.391	12.274	12.474	12.438

TABLE 4.4: Soret coefficients and numerical error for DCMIX1, DCMIX2 and DCMIX3. Theoretical value ($t = \infty$), analytical value ($t = t_{end}$), numerical value for $g_i = 0$ (G0) and numerical value for reboosting located at the Beginning1 (B1), Beginning2 (B2), Middle1 (M1), Middle2 (M2) and End (E). Superscripts 1 and 2 correspond to the use of Equations (4.3) and (4.4) respectively for the *CD*

		$\varepsilon^1_{B1_{reboost}}$	$\varepsilon^2_{B1_{reboost}}$	$\varepsilon^1_{B2_{reboost}}$	$\varepsilon^2_{B2_{reboost}}$	$\varepsilon^1_{M1_{reboost}}$	$\varepsilon^2_{M1_{reboost}}$	$\varepsilon^1_{M2_{reboost}}$	$\varepsilon^2_{M2_{reboost}}$	$\varepsilon^1_{E_{reboost}}$	$\varepsilon^2_{E_{reboost}}$
DCMIX1	w_1	0.001	0.001	0.072	0.068	0.646	0.642	4.452	4.933	16.120	24.031
	w_2	0.005	0.005	0.493	0.484	2.959	3.027	11.772	13.983	13.709	19.141
DCMIX2	w_1	0.014	0.014	0.735	0.718	5.665	5.685	35.968	39.891	63.227	99.204
	w_2	0.006	0.006	0.298	0.291	2.296	2.303	14.936	16.522	57.182	86.105
DCMIX3	w_1	0.003	0.004	0.333	0.350	1.358	1.503	3.818	4.657	3.470	3.831
	w_2	0.004	0.004	0.365	0.385	1.467	1.630	4.004	4.907	3.354	3.633

TABLE 4.5: Percentage error obtained in the measuring of S_{Ti} for DCMIX1, DCMIX2 and DCMIX3 when reboosting occurs at the Beginning1 (B1), Beginning2 (B2), Middle1 (M1), Middle2 (M2) and End (E). Superscripts 1 and 2 correspond to the use of Equations (4.3) and (4.4) respectively for the *CD*

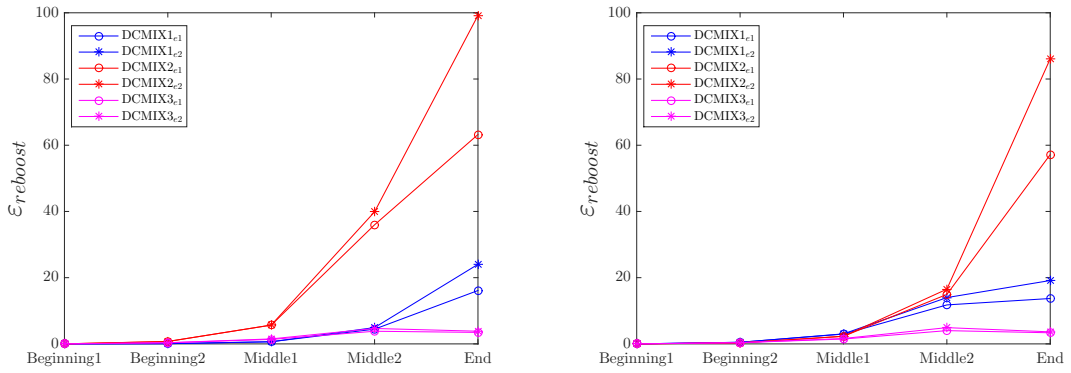

(A) (B)

FIGURE 4.5: Plot of the error obtained in the measurement of S_{Ti} for DCMIX 1, 2 and 3 when reboosting occurs at the Beginning1, Beginning2, Middle1, Middle2 and End (E) for w_1 and w_2. Subscripts $e1$ and $e2$ correspond to the use of Equations (4.3) and (4.4) respectively for the CD

4.1.4.3 Impact of reboosting on the steady state condition

It is also interesting to analyse how the system behaves if a reboosting occurs when the separation has reached the steady state condition ($\hat{t} \approx 2.5 \cdot 10^4$ s for DCMIX2). This is the most harmful situation, since the concentration separation together with the thermal field creates the largest density gradient, and therefore the system is more sensitive to any acceleration field. To analyse this situation, the CD_1 is used to compare the simulation of the experiment during a reboosting and during a quiescent period with the analytical value. This has been done only for the DCMIX2 mixture, because this mixture exhibits the largest distortion caused by the reboosting and because it is the only mixture considered in this study that is being used again in the DCMIX4 campaign.

Figure 4.6 shows the time evolution of CD_1 for the analytical, quiescent and reboosting case after reaching the steady state, $2.5 \cdot 10^4$ $s \leq \hat{t} \leq 7.5 \cdot 10^4$ s.

To eliminate again the numerical error, the CD_1 value for the quiescent (CD_Q) and for the reboosting (CD_R) cases has been obtained as follows,

$$CD_{Q,R} = CD'_{Q,R} + (CD_{analytical} - CD_{G0}), \tag{4.7}$$

where the $CD'_{Q,R}$ is the value obtained in the simulations, $CD_{analytical}$ is the analytical value, and CD_{G0} is the value obtained with a simulation with $g_i = 0$. As it can be seen in Figure 4.6, the quiescent scenario matches the analytical solution, while the system needs approximately $\backsim 2.5 \cdot 10^4$ s to recover the steady state condition.

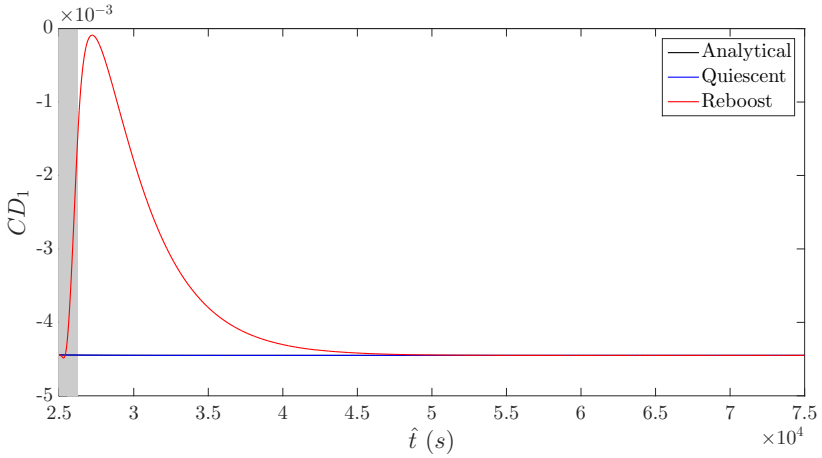

FIGURE 4.6: Time evolution of the CD_1 during DCMIX2 when both a reboosting and a quiescent period occur once the steady state has been reached at $\hat{t} = 2.5 \cdot 10^4$ s. Shadowed area represents the reboosting action

During the period in which the reboosting is occurring, a single convective cell is established with the rotation axis aligned with the y-direction, since the reboosting is acting in the x-direction, and the density gradient is in the z-direction. As it can be seen in Figure 4.7, during the reboosting the maximum velocity is $\backsim 1.4 \cdot 10^{-5}$ m/s, although after the reboosting, the largest value of maximum velocity decreases one order of magnitude down to $\backsim 1.6 \cdot 10^{-6}$ m/s. During the quiescent period, the maximum velocity found is of the same order of magnitude (10^{-6} m/s).

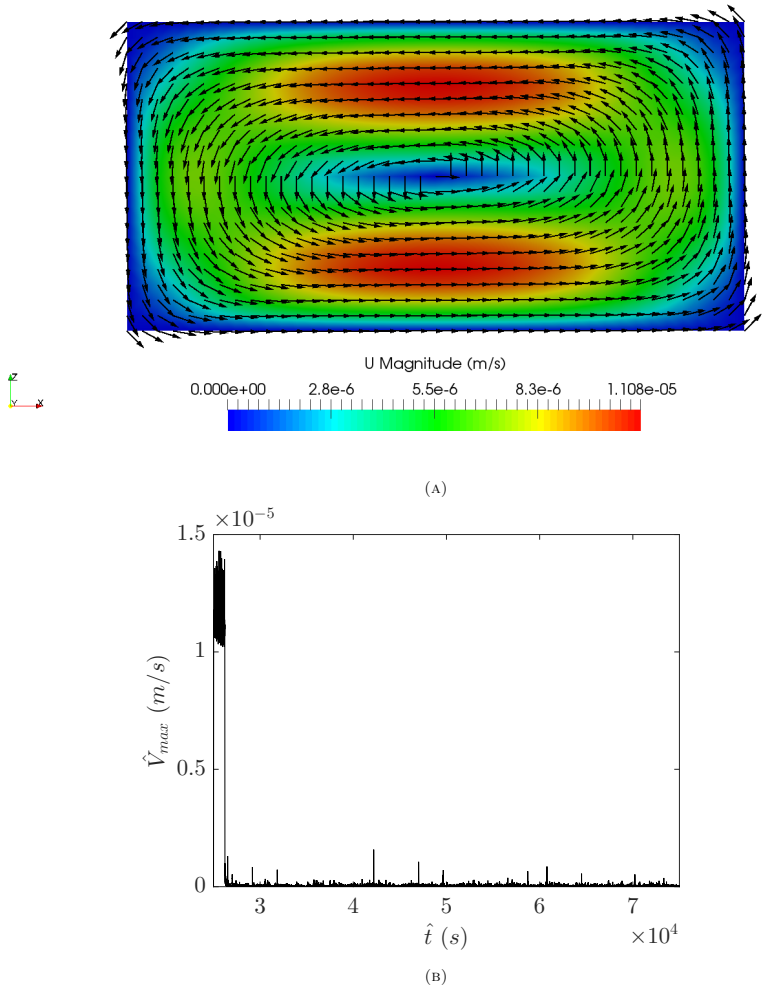

FIGURE 4.7: a) Convective cell produced during the reboosting at time $\hat{t} = 2.6 \cdot 10^4$ s and b) the modulus of the maximum velocity against time in the DCMIX2 mixture

4.2 Pure diffusion step

In this section the experimental pure diffusion step has been reproduce by solving numerically the physical and mathematical model described in Chapter 3. The impact of different reboosting scenarios on the DCMIX1, DCMIX2 and DCMIX3 experiment has been analysed.

4.2.1 Characteristics of the studied cases

Six different compositions of the (THN-IBB-nC12) DCMIX1 mixture have been analysed. Experimental values of the different magnitudes extracted from the literature are summarized in Tables 4.6 and 4.7. It can be seen a relatively large scatter in the values of the different diffusion coefficients depending on the measurement technique used, but

also within the different sets of experiments using the same technique. The thermodiffusion, diffusion and Soret coefficients used in this study are representative enough of those obtained in the literature. Table 4.8 shows the selected values.

	THN-IBB-nC12	$\boldsymbol{\rho(\mathbf{w_1},\mathbf{w_2}) = \mathbf{A}\cdot\mathbf{w_1} + \mathbf{B}\cdot\mathbf{w_2} + \mathbf{c}}$ $(kg\cdot m^{-3})$			$\boldsymbol{\rho(\mathbf{w_1},\mathbf{w_2}) = \rho_0}$ $(kg\cdot m^{-3})$	$\boldsymbol{\alpha}$ $(10^{-3}\cdot K^{-1})$	$\boldsymbol{\mu}$ $(10^{-3}\cdot kg\cdot m^{-1}\cdot s^{-1})$	**Ref. (year)**
	$w_{01}-w_{02}-w_{03}$	A	B	C				
MIXTURES	0.33-0.33-0.33 (Earth laboratory)	217.400	115.443	732.613	842.451	0.914	1.289	[11] (2010)
	0.10-0.10-0.80 (ISS)	183.416	94.189	744.191	771.952	0.954	1.314	[23] (2015)
	0.10-0.80-0.10 (ISS)	228.052	122.807	726.245	847.296	0.947	1.053	[23] (2015)
	0.40-0.20-0.40 (Earth laboratory)	218.554	116.189	731.888	842.547	0.905	1.354	[23] (2015)
	0.45-0.10-0.45 (ISS)	217.380	115.505	732.490	841.862	0.900	1.440	[23] (2015)
	0.80-0.10-0.10 (ISS)	262.597	145.028	700.860	925.440	0.848	1.719	[53] (2015)

	THN-IBB-nC12	$\mathbf{D_{11}}$	$\mathbf{D_{12}}$	$\mathbf{D_{21}}$	$\mathbf{D_{22}}$	**Technique**	**Ref. (year)**
	$w_{01}-w_{02}-W_{03}$	$(10^{-10}\cdot m^2\cdot s^{-1})$					
MIXTURES	0.33-0.33-0.33 (Earth laboratory)	6.92	1.06	-1.37	11.57	CFDC	[70] (2013)
		6.16	-4.61	0.37	11.40	SST	[55] (2014)
		10.31 ± 0.01	0.33 ± 0.13	-4.36 ± 0.01	6.41 ± 0.21	TD	[55, 68] (2013,2014)
		11.60 ± 0.01	0.32 ± 0.16	-6.18 ± 0.19	6.65 ± 0.33	CFDC	[55, 68] (2013,2014)
		8.00 ± 2.00	-2.30 ± 0.60	-2.00 ± 0.50	6.00 ± 2.00	SST	[54] (2015)
		10.1	0.40	-4.07	6.33	TD	[83] (2016)
		5.62	-5.91	1.08	12.18	OBD	[55, 68] (2013,2010)
	0.10-0.10-0.80 (ISS)	10.00 ± 3.00	-0.21 ± 0.06	-1.70 ± 0.40	7.00 ± 2.00	SST	[54] (2015)
		11.2	-0.41	-3.63	9.43	TD	[83] (2016)
	0.10-0.80-0.10 (ISS)	10.00 ± 1.00	-0.80 ± 0.10	-1.50 ± 0.20	10.00 ± 1.00	SST	[54] (2015)
		10.8	-0.13	-1.85	9.13	TD	[83] (2016)
	0.40-0.20-0.40 (Earth laboratory)	8.00 2.00	1.30 ± 0.40	-1.30 ± 0.40	4.00 ± 1.00	SST	[54] (2015)
	0.45-0.10-0.45 (ISS)	7.00 ± 1.00	0.32 ± 0.06	-0.14 ± 0.03	7.00 ± 1.00	SST	[54] (2015)
		8.12	-0.30	-2.61	6.64	TD	[83] (2016)
	0.80-0.10-0.10 (ISS)	5.50 ± 0.51	-0.99 ± 0.63	0.002 ± 0.03	6.60 ± 0.37	OEC	[12, 28] (2015,2015)
		5.23 ± 0.66	-1.80 ± 0.23	0.39 ± 0.05	8.28 ± 1.00	SST	[12, 53] (2015,2015)
		6.61 ± 0.10	-0.59 ± 0.51	-1.55 ± 0.10	5.98 ± 0.44	TD	[12, 66] (2015,2015)

TABLE 4.6: Compilation of the different values reported in the literature for the density, thermal expansion coefficient, dynamic viscosity and diffusion coefficients of six relevant ternary mixtures of the liquid system THN/IBB/nC12. (Acronym list: **CFDC**.- Counter Flow Diffusion Cell, **SST**.- Sliding Symmetric Tubes, **TD**.-Taylor Dispersion, **OBD**.- Optical Beam Deflection, **OEC**.- Open Ended Capillary)

4.2.2 Spatial discretization verification

Simulations at $Ra_1 = 2.512{\cdot}10^8$, $Ra_2 = 1.334{\cdot}10^8$, $Sc = 1.824{\cdot}10^3$ and $D_{12} = -1.824{\cdot}10^{-1}$, $D_{21} = 3.182\cdot10^{-1}$, $D_{22} = 1.031$, which correspond to the case labelled as 1 in Table 4.8 with a constant gravity level of 10 m/s^2 acting along the positive x-direction have been carried out to determine the effect of the finite size of the mesh on the results. This level of gravity corresponds to the highest value of acceleration simulated multiplied by a factor of 100. The time step used was $\Delta t = 3.024\cdot10^{-6}$. The number of cells for the four different uniform meshes attempted are $N_x = 30$, $N_y = 30$, $N_z = 15$, for the first, $N_x = 60$, $N_y = 60$, $N_z = 30$, for the second, $N_x = 80$, $N_y = 80$, $N_z = 40$, for the third, and $N_x = 100$, $N_y = 100$, $N_z = 50$, for the fourth. Figure 4.8, shows the time evolution of the averaged concentration w_1 at the hot wall of the cavity. According to this figure,

	THN-IBB-nC$_{12}$	**D$_{T1}$**	**D$_{T2}$**	**Technique**	**Ref. (year)**	**S$_{T1}$**	**S$_{T2}$**	**Technique**	**Ref. (year)**
	$w_{01} - w_{02} - w_{03}$	$10^{-12} \cdot m^2 \cdot s^{-1} \cdot K^{-1}$				$10^{-3} \cdot K^{-1}$			
MIXTURES	0.33-0.33-0.33	1.10 ± 0.01	0.12 ± 0.02	TGC	[47] (2010)	-	-	TGC + SST	[54] (2015)
	(Earth laboratory)	1.08 ± 0.06	0.06 ± 0.05	TGC	[68] (2015)	1.60 ± 0.40	0.60 ± 0.30		
	0.10-0.10-0.89	laboratory)	0.28 ± 0.04	TGC	[23] (2015)	(2015)	-	TGC + SST	[54] (2015)
	(ISS)	0.51 ± 0.01	0.24 ± 0.03	TGC	[68] (2015)	0.54 ± 0.07	0.36 ± 0.15		
	0.10-0.80-0.10	0.33 ± 0.02	0.12 ± 0.03	TGC	[23] (2015)	-	-	TGC + SST	[54] (2015)
	(ISS)	0.34 ± 0.02	0.17 ± 0.02	TGC	[68] (2015)	0.31 ± 0.06	0.29 ± 0.15		
	0.40-0.20-0.40	1.23 ± 0.03	0.10 ± 0.03	TGC	[23] (2015)	-	-	TGC + SST	[54] (2015)
	(Earth laboratory)	1.25 ± 0.05	0.05 ± 0.03	TGC	[68] (2015)	1.50 ± 0.40	0.60 ± 0.20		
	0.45-0.10-0.45	1.33 ± 0.02	0.11 ± 0.08	TGC	[23] (2015)	-	-	TGC + SST	[54] (2015)
	(ISS)	1.36 ± 0.03	0.03 ± 0.02	TGC	[68] (2015)	1.90 ± 0.20	0.10 ± 0.10		
	0.80-0.10-0.10 (ISS)	0.67 ± 0.05	-0.18 ± 0.01	TGC	[53] (2015)	1.19 ± 0.09	-0.28 ± 0.06	TGC + SST	[53] (2015)
		0.68 ± 0.05	-0.20 ± 0.01	-	[83] (2015)	1.17 ± 0.06	-0.29 ± 0.01	Diff.	[12] (2015)
		-	-	-	-	1.38 ± 0.05	-0.77 ± 0.02	-	[12] (2015)
		0.66 ± 0.01	-0.17 ± 0.01	TGC	[68] (2015)	-	-	-	-
		0.690	-0.215	Calc.	[28] (2015)	1.035	-0.093	ODI	[66] (2015)
		0.988	-0.680	Calc	[28] (2015)	1.426	-0.767	ODI	[66] (2015)
		-	-	-	-	1.39 ± 0.24	-0.90 ± 0.15	ODI	[28] (2015)
		0.72 ± 0.26	-0.22 ± 0.42	OBD	[66] (2015)	1.20 ± 0.09	-0.34 ± 0.14	OBD	[31] (2015)
		-	-	-	-	1.37 ± 0.06	-0.82 ± 0.05	ODI	[9] (2015)

TABLE 4.7: Compilation of the different values reported in the literature for the thermodiffusion and Soret coefficients in the case of six relevant ternary mixtures of the liquid system THN/IBB/nC12. (Acronym list: **TGC**.- Thermogravitational Column, **SST**.- Sliding Symmetric Tubes, **Calc**.- Obtained from the values of the Soret coefficients, **OBD**.- Optical Beam Deflection, **ODI**.- Optical Digital Imaging, **Diff**.- Different techniques – for more details, see the enclosed references)

the $60 \times 60 \times 30$ mesh, presents a good compromise between accuracy and computational cost. Consequently this mesh has been selected for all the simulations.

	$\hat{\mathbf{D}}_{11}$ $(10^{-10} \cdot m^2 s^{-1})$	$\hat{\mathbf{D}}_{12}$ $(10^{-10} \cdot m^2 s^{-1})$	$\hat{\mathbf{D}}_{21}$ $(10^{-10} \cdot m^2 s^{-1})$	$\hat{\mathbf{D}}_{22}$ $(10^{-10} \cdot m^2 s^{-1})$	$\hat{\mathbf{D}}_{T1}$ $(10^{-12} \cdot m^2 s^{-1} \cdot K^{-1})$	$\hat{\mathbf{D}}_{T2}$ $(10^{-12} \cdot m^2 s^{-1} K^{-1})$	$\hat{\mathbf{S}}_{T1}$ $(10^{-3} \cdot K^{-1})$	$\hat{\mathbf{S}}_{T2}$ $(10^{-3} \cdot K^{-1})$	$\mathbf{w_{01} - w_{02} - w_{03}}$
Case 1 (Earth laboratory)	8.39	-1.53	-2.67	8.65	1.90	0.09	2.42	0.85	0.33-0.33-0.33
Case 2 (ISS)	10.60	-0.31	-2.67	8.22	0.50	0.26	0.49	0.47	0.10-0.10-0.80
Case 3 (ISS)	10.40	-0.47	-1.68	9.57	0.34	0.14	0.34	0.21	0.10-0-80-0.10
Case 4 (Earth laboratory)	8.00	1.30	-1.30	4.00	1.24	0.08	1.44	0.67	0.40-0.20-0.40
Case 5 (ISS)	7.56	0.01	-1.38	6.82	1.34	0.07	1.77	0.46	0.45-0.10-0.45
Case 6 (ISS)	5.78	-1.13	-0.39	6.95	0.73	-0.28	1.20	-0.34	0.80-0.10-0.10

TABLE 4.8: Diffusion, thermodiffusion, Soret coefficients and mass concentration of the different mixtures used in the present study

4.2.3 Accelerometric environment

Reboosting data coming from the MAMS OSSRAW sensor located in the U.S. Lab (Destiny module) and corresponding to December 9^{th}, 2011, was used to create the different accelerometric scenarios. Three different signals have been considered. Figure 4.9a shows the whole raw signal ($0 \leq \hat{t} \leq 16218\ s$). This time has been selected because is of the same order of magnitude of the characteristic diffusion time ($\hat{\tau} = \hat{L}^2/\hat{D} \approx 2.5 \cdot 10^4\ s$). Figure 4.9b plots the period $0 \leq \hat{t} \leq 274\ s$ of the whole signal (see Figure 4.9a), focusing on the the reboosting manoeuvre ($0 \leq \hat{t} \lesssim 80\ s$). Finally, the long signal in Figure 4.9c has been constructed artificially by repeating nine times the reboosting period to reinforce the possible impact of this impulsive disturbance on the liquid mixture. With these three signals, a total of six different accelerometric scenarios have been considered

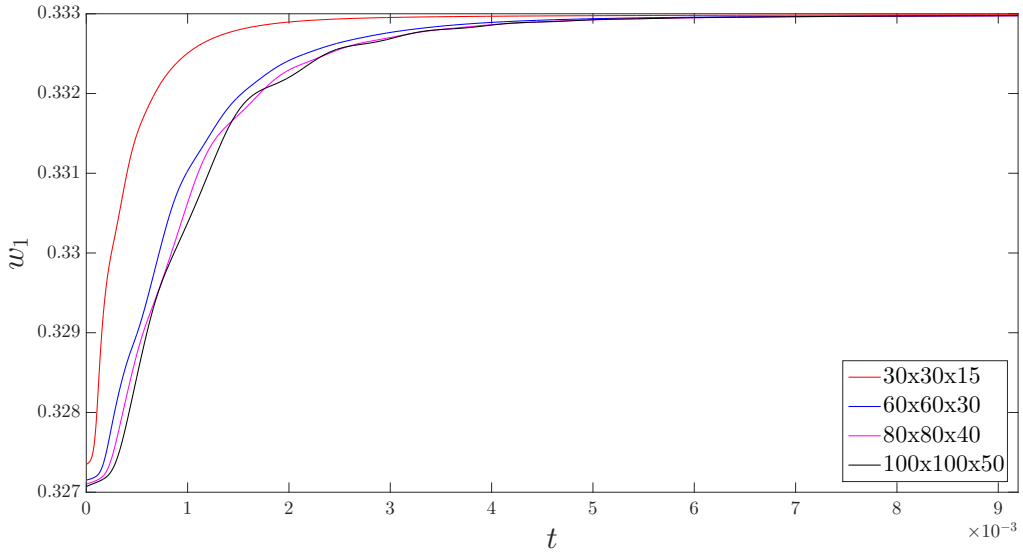

FIGURE 4.8: Grid independence test. Time-evolution of the concentration of w_1 averaged at the hot wall of the cavity

(see Table 4.9). Most of the simulations were performed using the signal shown in Figure 4.9b, during 274 s, along the x-direction (perpendicular to the concentration gradients) and three different acceleration magnitudes with multiplication factors of 1, 10 and 100. Simulations with the acceleration acting along the z-direction (parallel to the concentration gradients) have also been considered only with a multiplication factor of 1. In addition, a set of simulations have been carried out with the signal shown in Figure 4.9c in which the boosting period has been extended artificially up to 664 s. Finally, two cases (Case 1 and 5) have been selected to simulate during the 16218 s of the whole signal.

	Simulated cases (see Table 4.8)	**Direction**	**K (Intensity factor)**	**Duration (s) (see Fig. 4.9)**
RX1S	1-6	x	1	274 (4.9.b)
RX10S	1-6	x	10	274 (4.9.b)
RX100S	1-6	x	100	274 (4.9.b)
RZ1S	1-6	z	1	274 (4.9.b)
RX1L	1-6	x	1	664 (4.9.c)
RX1W	1 and 5	x	1	16218 (4.9.a)

TABLE 4.9: Characteristics of the different accelerometric scenarios

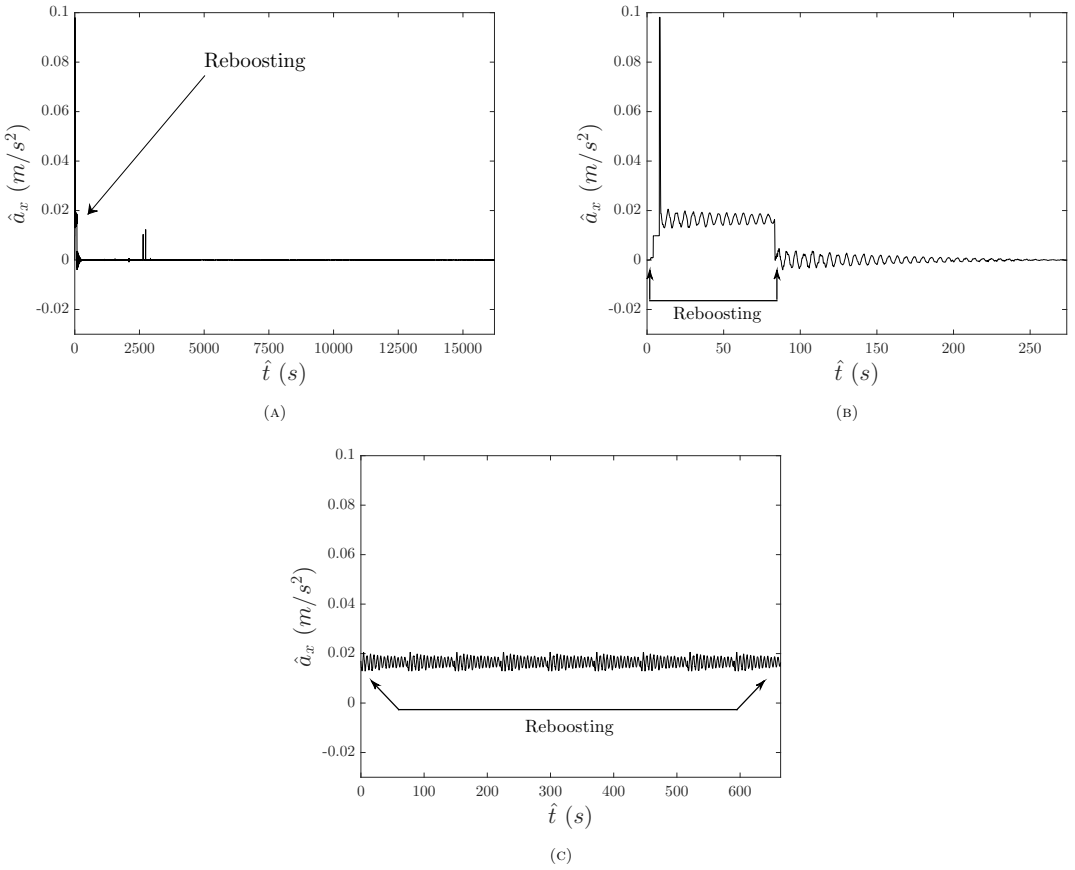

FIGURE 4.9: Signals used for simulations. a) whole signal, b) short signal, c) long signal

4.2.4 Results

4.2.4.1 Concentration profile

In order to evaluate the impact of different accelerometric scenarios, the concentration profile along the x-direction, with $y = 1$ and $z = 0.5$, has been used to analyse the deviation of the concentration field, since in a purely diffusive case, the concentration along this line is constant. Figure 4.10, shows the concentration profiles of the components 1 and 2, at the time in which the maximum deviation with respect to the analytical solution (see Appendix B [7]) for each case is attained. The profiles are normalized with the initial separation in each case according to the following expression,

$$w_i^*(t,x) = \frac{w_i(t,x) - w_{i,mean}(t,x)}{\Delta w_{i,mean}^{t=0}}, \qquad i = 1,2, \tag{4.8}$$

where $\Delta w_{i,mean}^{t=0} = |w_{i,max}(t,z) - w_{i,mean}(t,z)|$.

Concentration is not constant along the x-direction in any case, which means, that

the reboosting creates motion in the fluid perturbing the concentration field. It is worth noting that the deviation of component w_2 in Case 6 tends to move in the opposite direction respect the rest of the cases (see Figure 4.10b, 4.10d, 4.10f and 4.10h). This is due to the negative sign of the thermodiffusion coefficient $\hat{D}_{T2}$, which creates a reverse separation in component 2 (see Table 4.8 case 6).

As can be seen from Figure 4.10, not all cases have the same sensitivity to acceleration. To quantify more accurately this sensitivity, Table 4.10 summarizes the maximum deviation of the concentration defined as,

$$\varepsilon = max(|w_i^*(t,x)|) \cdot 100. \tag{4.9}$$

	RX1S		**RX10S**		**RX100S**		**RX1L**		**RZ1S**	
	w_1^*	w_2^*	w_1^*	w_2^*	w_1^*	w_2^*	w_1^*	w_2^*	w_1^*	w_2^*
Case 1	14.60	15.39	67.01	68.61	83.98	85.93	37.55	40.80	0.017	0
Case 2	3.43	3.57	31.10	32.00	75.27	76.85	9.71	10.47	0	0
Case 3	2.96	3.24	27.53	28.19	74.24	75.43	8.47	8.95	0	0.190
Case 4	8.94	9.43	57.19	59.34	81.44	84.00	24.69	27.76	0	0
Case 5	9.29	9.70	58.10	60.00	81.97	84.00	25.85	28.26	0.023	0
Case 6	4.80	4.72	40.40	39.88	78.63	77.79	14.17	13.65	0	0

TABLE 4.10: Maximum deviation of the concentration along the x-direction ($y = 1$ and $z = 0.5$)

It can be seen that even in the simulations performed with the raw short real signal (RX1S), the error ranges from 2.96% to 15.39%. The distortion created by the RZ1S (not shown in Figure 4.10) signal does not reach even 0.1% in any case because the buoyancy term acts parallel to the concentration gradient.

To justify the shape of the concentration distributions, Figure 4.11 shows the flow pattern created by the RX1S acceleration scenario in terms of the flow field in the plane $y = 1$ and an iso-surface of λ_2, a quantity defined in [39] to detect local minima of pressure produced by vortex cores. When the acceleration is perpendicular to the concentration gradient, i.e. x-direction, the buoyancy force creates a convective cell with the axis of rotation aligned with the y-direction as the one shown in Figure 4.11. In the case RZ1S (i.e. acceleration acting along the z-direction), the velocity magnitude is much lower than in the RX1S, since the density gradient is parallel to the acceleration vector and the fluid does not tend to rotate around the center of the cavity.

Finally, Figure 4.12 details the temporal dependence of the above-mentioned error for the different cases. Clearly, when the reboosting is acting, the error increases rapidly but once reboosting finishes, the error tends to decay slowly. Figure 4.12d shows how the error increases monotonically when the reboosting is acting all the time.

4.2.4.2 Error of the Diffusion coefficients

To analyse the impact of the reboostings on the value of the diffusion coefficients, case 1 and 5 have been selected, since results show that they are the more distorted cases on Earth laboratories and onboard the ISS, respectively. In order to analyse this impact, the CD between the hot and cold walls (see Figure 3.4) as a function of time has been computed. This procedure tries to mimic how the experimentalists extract the coefficients from the ISS experiments. For the duration of the whole diffusive part of the experiment, the RX1W scenario has been selected.

To obtain the analytical CD, from the $1D$ concentration distribution, the following expression is used along the z-direction in order to compare with numerical results,

$$CD_{i,analytical}(t) = \frac{|w_i(t,0) - w_i(t,1)|}{CD_{i,initial}}, \qquad i = 1,2, \tag{4.10}$$

with $CD_{i,initial} = |w_i(0,0) - w_i(0,1)|$. For the numerical case, the CD is calculated by averaging the value of concentration at the hot and cold walls according to the following expression,

$$CD_{i,num}(t) = \frac{|\overline{w_i}(t,x,y,0) - \overline{w_i}(t,x,y,1)|}{CD_{i,initial}}, \qquad i = 1,2, \tag{4.11}$$

where $\overline{w_i}$ is the mean value of component i at the corresponding boundary. So, to compute the diffusion coefficients that would be obtained in an experiment with a reboosting, it should be found the set of diffusion coefficients that minimizes the following objective function,

$$\begin{aligned}\Phi(D_{12}, D_{21}, D_{22}) = \int_{t=0}^{t=t_{end}} [&|CD_{1,analytical}(t) - CD_{1,num}(t)| + \\ &|CD_{2,analytical}(t) - CD_{2,num}(t)|]dt.\end{aligned} \tag{4.12}$$

To find the minimum of Equation (4.12), a large number of sets of diffusion coefficients have been evaluated ($\approx 8 \cdot 10^6$ sets). The set of diffusion coefficients indicated in Table 4.11 ranges from $0.5 \cdot D_{ij}$ to $1.5 \cdot D_{ij}$ with a resolution of $0.005 \cdot D_{ij}$. Based on all the sets, the analytical CD is calculated and compared to the numerical one and then to the function $\Phi(D_{12}, D_{21}, D_{22})$. Due to the used resolution, the analytical case that better fits

the numerical simulation, can have a maximum and a minimum difference of ±50% and ±0.005% respectively. Since the CD is a function of time, the predicted numerical values every 500 s until the end of the simulation (i.e. $\hat{t}_{end} = 16000\ s$) have been considered. Also, the minimum of the function $\Phi(D_{12}, D_{21}, D_{22})$ for a zero-g acceleration level of the cases 1 and 5 (numerical solution for pure diffusion), has been found in order to determine the level of error associated with the simulation and with the numerical evaluation of the integral of Equation (4.12).

		D_{12}	D_{22}	D_{21}
Values used in simulations	Case 1	-0.1824	1.0310	-0.3182
	Case 5	0.0013	0.9021	-0.1825
Best analytical solution for $g_i = 0$	Case 1	-0.1805 (-1%)	1.0258 (-0.5%)	-0.3151 (-1%)
	Case 5	0.0010 (-21%)	0.8976 (-0.5%)	-0.1798 (-1.5%)
Best analytical solution for reboosting	Case 1	-0.1751 (-4%)	1.0155 (-1.5%)	-0.3071 (3.5%)
	Case 5	0.0019 (43.5%)	0.8976 (-0.5%)	-0.1789 (-2%)
Percentage of error after removing the numerical error	Case 1	-3%	-1%	-2.5%
	Case 5	64.5%	0%	0.5%

TABLE 4.11: Set of diffusion coefficients that better fits the numerical cases by evaluating the CD during reboosting time for Case 1 and 5 and associated error, included the zero-g acceleration level for both cases

It can be seen in Table 4.11, that the largest difference in the diffusion coefficients when the reboosting is acting reaches a value of 64.5% for the coefficient D_{12} in case 5. This value is larger than the above-mentioned maximum error (50%), since the $g_i = 0$ case shows a 21% smaller D_{12} value than the used one, while the value of this same diffusion coefficient for the best fitted case during reboosting is 43.5% larger. The fact that diffusion coefficient D_{12}, is two orders of magnitude smaller than D_{22}, makes it very sensitive to any disturbance. It can be seen that, the larger the relative value of the diffusion coefficient the smaller the error found.

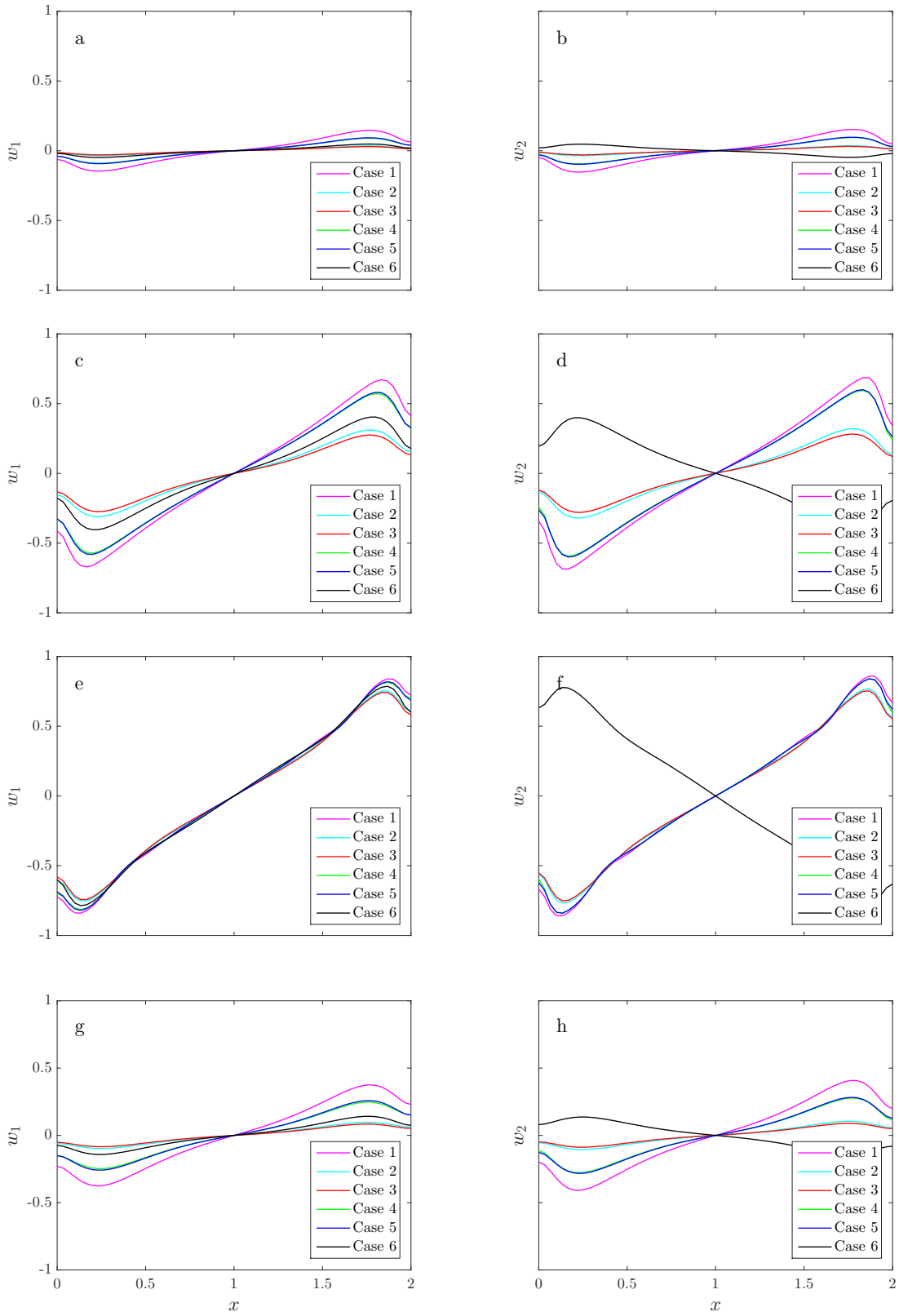

FIGURE 4.10: Concentration profiles of different cases along the x-direction ($y = 1$, $z = 0.5$) for signals RX1S a), b), RX10S c), d), RX100S e), f) and RX1L g), h)

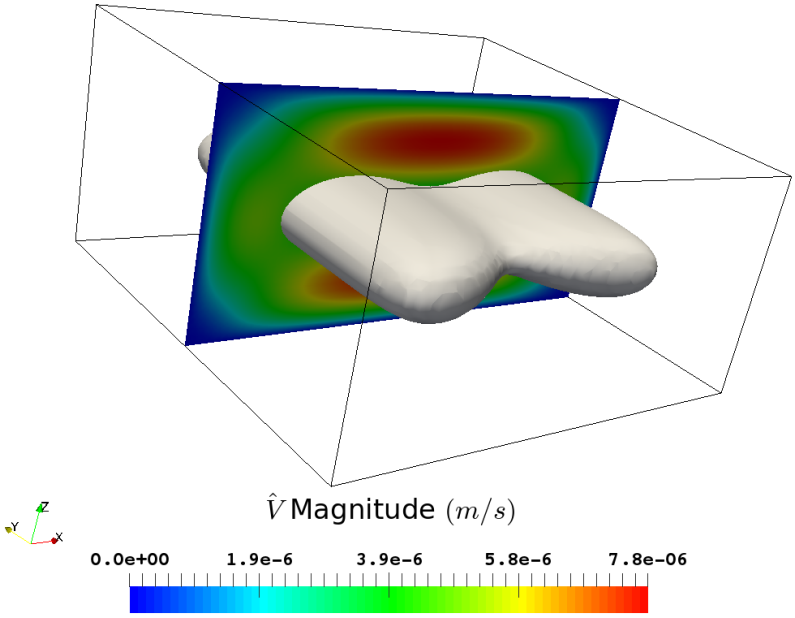

FIGURE 4.11: Convective cell induced by an acceleration perpendicular to the concentration gradient. Vector plot of velocity in the XZ-plane $y = 1$ and isosurface of $\lambda_2 = 5 \cdot 10^{-6}$ (Case 1 RX1S)

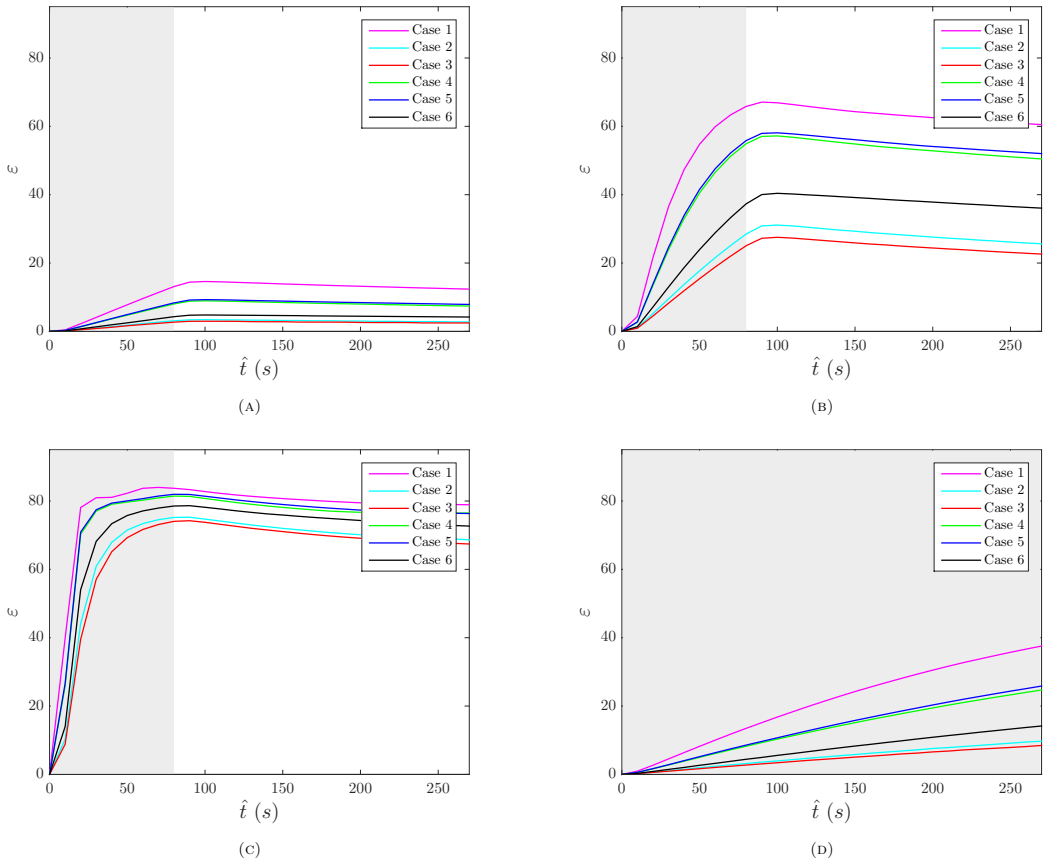

FIGURE 4.12: Maximum deviation of the concentration, ε, as function of time for all cases in each accelerometric scenario. a) RX1S, b) RX10S, c) RX100S and d) RX1L. Shadowed area shows the period when the reboosting is acting

Chapter 5

Conclusions and future works

5.1 Conclusions

In this thesis, the microgravity environment of the International Space Station (ISS) and how the reboosting manoeuvres can affect the DCMIX thermodiffusion experiments have been analysed. Signals coming from different sensors onboard the ISS have been examined to properly characterize the microgravity conditions to which the Diffusion and thermodiffusion Coefficient Measurements in ternary mIXtures (DCMIX) experiments are subject to. The strongest disturbances found have been the reboosting, which produced accelerations levels that can easily exceed the ISS microgravity limits requirements. Thus, special attention has been paid to these episodes. A new OpenFOAM solver has been created to numerically simulate the response of the different DCMIX systems under different reboostings microgravity scenarios created with real acceleration signals.

Accelerometric characterization

Different techniques have been used depending on the availability of the sensors data. Acceleration levels averaged each eight hours as function of time have been found to be successful detectors of the main disturbances existing during DCMIX1 experiments.

When using a SAMS2 signal, the application of Wavelet Denoising Technique (WDT) offers good results in the elimination of the high frequency component of the signal. Once the noise is eliminated from the signal, the low frequency range (the most harmful frequency range for the thermodiffusion experiments) can be properly analised. So, the WDT enables clear and fast comparisons of the different SAMS2 signals, in case MAMS

signals are not available. During the ZOAs disturbances, low frequency bands are different for the three coordinates (X_A, Y_A and Z_A). At high frequencies, the denoising of SAMS2 data shows similar patterns in all cases. During the analysed ZOAs, the environment did not accomplish the ISS vibratory limits requirements, mainly in the low frequency range. During the quiescent periods, the accelerometer in the Glovebox registered an acceleration level within the required limits, while the sensor attached to the structure of the experimental module registered a level slightly higher.

Depending on the selected sensor the main disturbances occurred during the runs, can be analysed or not. Medium disturbances as dockings, have been clearly identified in the Columbus module and were inappreciable within the other ones. In general, the Columbus module presented higher SEN spikes being more vulnerable to the vibrations. RMS warning map technique successfully detected predominant disturbances on Z_A direction at low frequency bands $< 10\ Hz$ for all the analysed signals.

Impact of reboosting on the experiments

The impact of different microgravity scenarios on the calculation of the Soret coefficient during the DCXMIX1, DCMIX2 and DCMIX3 thermodiffusion step and the diffusion coefficients during the DCMIX1 pure diffusion step have been independently analysed. For studying the influence of the reboosting on the Soret coefficients, the largest up-to-date reboosting has been applied at different times of the thermodiffusion step of the experiments. To analyse the error in the calculation of the diffusion coefficients, a typical reboosting occurred during DCMIX1 period has been used to create different microgravity scenarios. In this case, different acting directions, intensities and durations have been applied during the pure diffusion step of the DCMIX1 experiment.

The sensitivity of the system to the reboosting can be determined by using the analytical solution at the time when the reboosting is acting, to calculate the buoyancy term, i.e. the sum of the two concentrational and the thermal Grashof numbers involved in the problem. The larger the sum of the Grashof numbers, the more sensitivity of the system to any acceleration. The thermal Grashof is the one that presents more variation among the different DCMIX mixtures, and therefore, in the three mixtures analysed, is the parameter that determines the distortion of the concentration field.

During the thermodiffusion step, if the Soret coefficient is obtained just by using the value of $CD(t_{end})$, the closer the reboosting occurs to the time of measuring the CD, the larger the error. Using the average value of CD on the hot and cold walls, leads to a lower error than using the concentration in a point of the isothermal walls, although

the error is very similar in both cases. The maximum error is approximately 100% when reboosting occurs at the end of the thermodiffusion step for DCMIX2 mixture.

The simulations showed that when the reboosting acts perpendicular to the concentration gradient during the diffusive step, it creates one convective cell that can substantially distort the concentration field while acceleration parallel to the concentration gradient creates weak convection, and therefore, the distortion of the concentration field is negligible. When the reboosting acts perpendicular to the concentration gradient, the values of the calculated diffusion coefficients can have up to 64% of error. The error is always bigger for the coefficient that has a smaller relative value (normally the cross-diffusion coefficients are significantly smaller than the pure diffusion coefficients).

Taking into account all the aforementioned, it can be stated that the impact of the reboosting on the calculation of the coefficients strongly depends on the system involved in, as different mixtures can have very different thermophysical properties. Furthermore, the method used for calculating the CD and quantifying the concentration field can affect the resulting value of the coefficients.

5.2 Future work

Further analysis can be done in order to help the development of the DCMIX project, in term of saving time or helping the selection of the ternary mixture to be analysed. Some of these further considerations are:

- Calculating the critical Grashof number for typical reboosting manoeuvres would help to know if a DCMIX experiment with a specific system can be conducted during a reboosting or not with the consequent saving of time. Furthermore, if a mixture has very high Grashof numbers, it might be even inappropriate for being used in a microgravity experiment.
- Simulate a whole experiment taking into account the thermodiffusive and pure diffusion step to calculate diffusion and Soret coefficients.
- Study the influence of quiescent periods to analyse if the microgravity level can trigger any perturbation in the concentration field.
- Use a more complex mathematical model by introducing concentration and temperature dependent thermophysical values.

Appendix A

1D analytical solution: Thermodiffusion

The analytical solution that governs the transient concentration field for a ternary liquid system inside the Soret cell with an applied thermal gradient, has been obtained analytically by solving the system of mass transport Equations (3.8)-(3.9) in one dimension. The solution has been obtained following the study [69] for binary mixtures. For that purpose, two assumptions have been made:

1. The buoyancy forces are negligible since the experiment is carried out in a zero gravity environment. Therefore, the convective term can be removed from Equations (3.8)-(3.9), resulting

$$\frac{\partial w_1}{\partial t} = \frac{\partial^2 w_1}{\partial z^2} + D_{12}\frac{\partial^2 w_2}{\partial z^2} + D_{T1}\frac{\partial^2 T}{\partial z^2} \tag{A.1}$$

$$\frac{\partial w_2}{\partial t} = D_{21}\frac{\partial^2 w_1}{\partial z^2} + D_{22}\frac{\partial^2 w_2}{\partial z^2} + D_{T2}\frac{\partial^2 T}{\partial z^2} \tag{A.2}$$

2. Temperature profile does not change in time and varies linearly along the whole domain (z-direction of the cell, see Figure 3.4) according to

$$T(z) = z. \tag{A.3}$$

So the first and second derivative of the temperature function are $\partial T/\partial z = 1$ and

$\partial^2 T/\partial z^2 = 0$ respectively. Applying this to the Equations (A.1)-(A.2) results

$$\frac{\partial w_1}{\partial t} = \frac{\partial^2 w_1}{\partial z^2} + D_{12}\frac{\partial^2 w_2}{\partial z^2} \tag{A.4}$$

$$\frac{\partial w_2}{\partial t} = D_{21}\frac{\partial^2 w_1}{\partial z^2} + D_{22}\frac{\partial^2 w_2}{\partial z^2} \tag{A.5}$$

With these two considerations, the new system of Equations (A.4)-(A.5) can be solved using the appropriate boundary and initial conditions.

At the boundaries the mass flux, $\overrightarrow{J_i}$, is zero as the walls of the cavity are impermeable. The flux for each component is given by the expressions:

$$\overrightarrow{J_1}(t, z = 0) = \overrightarrow{J_1}(t, z = 1) = \frac{\partial w_1}{\partial z} + D_{12}\frac{\partial w_2}{\partial z} + D_{T1} = 0 \tag{A.6}$$

$$\overrightarrow{J_2}(t, z = 0) = \overrightarrow{J_2}(t, z = 1) = D_{21}\frac{\partial w_1}{\partial z} + D_{22}\frac{\partial w_2}{\partial z} + D_{T2} = 0. \tag{A.7}$$

The impermeable boundary conditions at the heated walls in the thermodiffusion problem, are mathematically equivalent to apply non-homogeneous Neumann boundary conditions,

$$\frac{\partial w_1(t, z = 0, 1)}{\partial z} = -D_{12}\frac{\partial w_2}{\partial z} - D_{T1} \tag{A.8}$$

$$\frac{\partial w_2(t, z = 0, 1)}{\partial z} = -\frac{D_{21}}{D_{22}}\frac{\partial w_1}{\partial z} - \frac{D_{T2}}{D_{22}}. \tag{A.9}$$

Applying some algebra on the system of Equations (A.6)-(A.7), the expressions of the Soret coefficients can be obtained as,

$$S_{T1} = \frac{D_{T1}D_{22} - D_{T2}D_{12}}{D_{22} - D_{12}D_{21}} \tag{A.10}$$

$$S_{T2} = \frac{D_{T2} - D_{T1}D_{21}}{D_{22} - D_{12}D_{21}} \tag{A.11}$$

At the beginning of the experiment, the mixture is completely mixed and homogen-

eous. Thus, the initial conditions are uniform concentration field for the three components,

$$w_i(t=0,z) = w_{0i} \qquad i = 1,2, \tag{A.12}$$

where w_{0i} is the average concentration of each component.

The following restrictions have been applied to avoid non-physical (non-real) solutions [96]:

$$1 + D_{22} > 0 \tag{A.13}$$

$$D_{22} - D_{12}D_{21} \geq 0 \tag{A.14}$$

$$D_{12} \neq 0 \tag{A.15}$$

$$(1 - D_{22})^2 + 4D_{12}D_{21} \geq 0. \tag{A.16}$$

Taking into account the above-mentioned assumptions, the system can be written in matrix form, together with the boundary and initial conditions as

$$\begin{pmatrix} \frac{\partial w_1}{\partial t} \\ \frac{\partial w_2}{\partial t} \end{pmatrix} = \begin{pmatrix} 1 & D_{12} \\ D_{21} & D_{22} \end{pmatrix} \begin{pmatrix} \frac{\partial^2 w_1}{\partial z^2} \\ \frac{\partial^2 w_2}{\partial z^2} \end{pmatrix}, \tag{A.17}$$

$$\frac{\partial w_i(t, z=0,1)}{\partial z} = -S_{Ti} \qquad i = 1,2, \tag{A.18}$$

$$w_i(t=0,z) = w_{0i} \qquad i = 1,2. \tag{A.19}$$

To solve this problem, the system of Equations (A.17) must be diagonalized to uncouple the two concentrations w_1 and w_2

$$\begin{pmatrix} \frac{\partial w_1}{\partial t} \\ \frac{\partial w_2}{\partial t} \end{pmatrix} = A \begin{pmatrix} \lambda_1 & 0 \\ 0 & \lambda_2 \end{pmatrix} A^{-1} \begin{pmatrix} \frac{\partial^2 w_1}{\partial z^2} \\ \frac{\partial^2 w_2}{\partial z^2} \end{pmatrix}, \tag{A.20}$$

where, λ_i, represents the eigenvalues of the diffusion coefficients matrix and A is the eigenvector matrix. A new variable ϕ_i can be introduced. Its relation with the concentration,

w_i, can be expressed with the inverse of the eigenvector matrix A^{-1} as

$$\begin{pmatrix}\phi_1\\ \phi_2\end{pmatrix} = A^{-1}\begin{pmatrix}w_1\\ w_2\end{pmatrix} = \begin{pmatrix}\alpha & \beta\\ \gamma & \delta\end{pmatrix}\begin{pmatrix}w_1\\ w_2\end{pmatrix}. \tag{A.21}$$

Using this change of variable, the system, the boundary and the initial conditions can now be written respectively in terms of ϕ_i, as follows

$$\begin{pmatrix}\frac{\partial\phi_1}{\partial t}\\ \frac{\partial\phi_2}{\partial t}\end{pmatrix} = \begin{pmatrix}\lambda_1 & 0\\ 0 & \lambda_2\end{pmatrix}\begin{pmatrix}\frac{\partial^2\phi_1}{\partial z^2}\\ \frac{\partial^2\phi_2}{\partial z^2}\end{pmatrix}, \tag{A.22}$$

$$\begin{pmatrix}\frac{\partial\phi_1(t,z=0,1)}{\partial z}\\ \frac{\partial\phi_2(t,z=0,1)}{\partial z}\end{pmatrix} = \begin{pmatrix}\alpha & \beta\\ \gamma & \delta\end{pmatrix}\begin{pmatrix}-S_{T1}\\ -S_{T2}\end{pmatrix}, \tag{A.23}$$

$$\begin{pmatrix}\phi_1(t=0,z)\\ \phi_2(t=0,z)\end{pmatrix} = \begin{pmatrix}\alpha & \beta\\ \gamma & \delta\end{pmatrix}\begin{pmatrix}w_{01}\\ w_{02}\end{pmatrix}, \tag{A.24}$$

where the eigenvalues, λ_1 and λ_2, are

$$\lambda_1 = \frac{(1-D_{22}) + \sqrt{(1-D_{22})^2 + 4D_{21}D_{12}}}{2} \tag{A.25}$$

$$\lambda_2 = \frac{(1-D_{22}) - \sqrt{(1-D_{22})^2 + 4D_{21}D_{12}}}{2} \tag{A.26}$$

and

$$\alpha = \delta = \frac{\lambda_2 - 1}{\lambda_2 - \lambda_1} \tag{A.27}$$

$$\beta = \frac{\lambda_2 - 1}{\lambda_2 - \lambda_1}\frac{D_{12}}{D_{12} - \lambda_2} \tag{A.28}$$

$$\gamma = \frac{\lambda_2 - 1}{\lambda_2 - \lambda_1}\frac{1 - \lambda_1}{D_{12}}. \tag{A.29}$$

The solution of the system (A.22) for the variable ϕ_i that satisfies the boundary

conditions (A.23), has the form

$$\phi_i(t,z) = \phi_{i,st}(z) + \sum_{n,odd}^{\infty} A_{i,n}\cos(n\pi z)e^{(-n^2\pi^2\lambda_i t)} \qquad i = 1,2, \tag{A.30}$$

where, $\phi_{i,st}(z)$, is the value of ϕ_i when the system reaches the steady state. The expression of $\phi_{i,st}(z)$ is obtained by means of the steady state of the concentration field $w_{i,st}(z)$,

$$w_{i,st}(z) = w_{i,st}(t\to\infty,z) = w_{0i} + S_{Ti}\left(\frac{1}{2} - z\right). \tag{A.31}$$

The introduction of the value of $w_{i,st}(z)$ into the Equation (A.21) gives,

$$\begin{pmatrix}\phi_{1,st}(z)\\ \phi_{2,st}(z)\end{pmatrix} = \begin{pmatrix}\phi_{1,st}(t\to\infty,z)\\ \phi_{2,st}(t\to\infty,z)\end{pmatrix} = \begin{pmatrix}\alpha & \beta\\ \gamma & \delta\end{pmatrix}\begin{pmatrix}w_{01} + S_{T1}\left(\frac{1}{2} - z\right)\\ w_{02} + S_{T2}\left(\frac{1}{2} - z\right)\end{pmatrix}. \tag{A.32}$$

The constants $A_{i,n}$ are determined from the initial conditions (Equation (A.24)),

$$\begin{pmatrix}A_{1,n}\\ A_{2,n}\end{pmatrix} = -\frac{4}{n^2\pi^2}\begin{pmatrix}\alpha & \beta\\ \gamma & \delta\end{pmatrix}\begin{pmatrix}S_{T1}\\ S_{T2}\end{pmatrix}. \tag{A.33}$$

The solution of the system of Equations (A.22) with boundary (A.23) and initial (A.24) conditions is

$$\phi_1(t,z) = (\alpha w_{01} + \beta w_{02}) - (\alpha S_{T1} + \beta S_{T2})\left[\frac{1}{2} - z - \frac{4}{\pi^2}\sum_{n,odd}^{\infty}\frac{1}{n^2}\cos(n\pi z)e^{(-n^2\pi^2\lambda_1 t)}\right] \tag{A.34}$$

$$\phi_2(t,z) = (\gamma w_{01} + \delta w_{02}) - (\alpha S_{T1} + \beta S_{T2})\left[\frac{1}{2} - z - \frac{4}{\pi^2}\sum_{n,odd}^{\infty}\frac{1}{n^2}\cos(n\pi z)e^{(-n^2\pi^2\lambda_2 t)}\right]. \tag{A.35}$$

Finally, the solution for the concentration field can be obtained by introducing the

expressions (A.34)-(A.35) in

$$\begin{pmatrix} w_1(t,z) \\ w_2(t,z) \end{pmatrix} = A \begin{pmatrix} \phi_1(t,z) \\ \phi_2(t,z) \end{pmatrix} = \begin{pmatrix} 1 & \frac{D_{12}}{\lambda_2 - 1} \\ \frac{\lambda_1 - 1}{D_{12}} & 1 \end{pmatrix} \begin{pmatrix} \phi_1(t,z) \\ \phi_2(t,z) \end{pmatrix}, \tag{A.36}$$

resulting

$$w_1(t,z) = \phi_1(t,z) + \frac{D_{12}}{\lambda_2 - 1}\phi_2(t,z) \tag{A.37}$$

$$w_2(t,z) = \frac{\lambda_1 - 1}{D_{12}}\phi_1(t,z) + \phi_2(t,z). \tag{A.38}$$

Appendix B

1D analytical solution: Pure Diffusion

The analytical solution previously obtained in [7] that governs the transient concentration field for a ternary liquid system inside the Soret cell when the thermodiffusion step has finished (i.e. the thermal gradient has been removed) is presented here. It has been obtained analytically by solving the system of mass transport Equations (3.8)-(3.9) in one dimension. For that purpose, two assumptions have been made:

1. The buoyancy forces are negligible since the experiment is carried out in a zero gravity environment. Therefore, the convection term can be removed from Equations (3.8)-(3.9), resulting

$$\frac{\partial w_1}{\partial t} = \frac{\partial^2 w_1}{\partial z^2} + D_{12}\frac{\partial^2 w_2}{\partial z^2} + D_{T1}\frac{\partial^2 T}{\partial z^2} \tag{B.1}$$

$$\frac{\partial w_2}{\partial t} = D_{21}\frac{\partial^2 w_1}{\partial z^2} + D_{22}\frac{\partial^2 w_2}{\partial z^2} + D_{T2}\frac{\partial^2 T}{\partial z^2} \tag{B.2}$$

2. When the thermodiffusion step has finished, the thermal gradient is removed. Since $\tau_T \gg \tau_D$, the system rapidly turns into isothermal. So, the system (B.3)-(B.4), can be simplify as follows

$$\frac{\partial w_1}{\partial t} = \frac{\partial^2 w_1}{\partial z^2} + D_{12}\frac{\partial^2 w_2}{\partial z^2} \tag{B.3}$$

$$\frac{\partial w_2}{\partial t} = D_{21}\frac{\partial^2 w_1}{\partial z^2} + D_{22}\frac{\partial^2 w_2}{\partial z^2} \tag{B.4}$$

With these two considerations, the new system of Equations (B.3)-(B.4) can be solved using the appropriate boundary and initial conditions.

At the boundaries the mass flux, $\overrightarrow{J_i}$, is zero as the walls of the cavity are impermeable. The flux for each component is given by the expressions:

$$\overrightarrow{J_1}(t, z = 0) = \overrightarrow{J_1}(t, z = 1) = \frac{\partial w_1}{\partial z} + D_{12}\frac{\partial w_2}{\partial z} \tag{B.5}$$

$$\overrightarrow{J_2}(t, z = 0) = \overrightarrow{J_2}(t, z = 1) = D_{21}\frac{\partial w_1}{\partial z} + D_{22}\frac{\partial w_2}{\partial z} \tag{B.6}$$

The impermeable boundary conditions at the walls in the pure diffusion problem, is mathematically equivalent to apply homogeneous Neumann boundary conditions,

$$\frac{\partial w_1(t, z = 0, 1)}{\partial z} = 0 \tag{B.7}$$

$$\frac{\partial w_2(t, z = 0, 1)}{\partial z} = 0. \tag{B.8}$$

The concentration field at the steady state of the thermodiffusion step (see Equation (A.31)) is considered here as the initial conditions, which corresponds with a linear profile along the whole domain (z-direction of the cell, see Figure 3.4), defined by

$$w_i(t = 0, z) = w_{0i} + S_{Ti}\left(\frac{1}{2} - z\right) \qquad i = 1, 2, \tag{B.9}$$

where w_{0i} is the average concentration of each component.

The following restrictions have been applied to avoid non-physical (non-real) solutions [96]:

$$1 + D_{22} > 0 \tag{B.10}$$

$$D_{22} - D_{12}D_{21} \geq 0 \tag{B.11}$$

$$D_{12} \neq 0 \tag{B.12}$$

$$(1 - D_{22})^2 + 4D_{12}D_{21} \geq 0. \tag{B.13}$$

Taking into account the above-mentioned assumptions, the system can be written in matrix form, together with the boundary and initial conditions as

$$\begin{pmatrix} \frac{\partial w_1}{\partial t} \\ \frac{\partial w_2}{\partial t} \end{pmatrix} = \begin{pmatrix} 1 & D_{12} \\ D_{21} & D_{22} \end{pmatrix} \begin{pmatrix} \frac{\partial^2 w_1}{\partial z^2} \\ \frac{\partial^2 w_2}{\partial z^2} \end{pmatrix}, \tag{B.14}$$

$$\frac{\partial w_i(t, z = 0, 1)}{\partial z} = 0 \qquad i = 1, 2, \tag{B.15}$$

$$w_i(t = 0, z) = w_{0i} + S_{Ti}\left(\frac{1}{2} - z\right) \qquad i = 1, 2. \tag{B.16}$$

To solve this problem, the system of Equations (B.14) must be diagonalized to uncouple the two concentrations w_1 and w_2

$$\begin{pmatrix} \frac{\partial w_1}{\partial t} \\ \frac{\partial w_2}{\partial t} \end{pmatrix} = A \begin{pmatrix} \lambda_1 & 0 \\ 0 & \lambda_2 \end{pmatrix} A^{-1} \begin{pmatrix} \frac{\partial^2 w_1}{\partial z^2} \\ \frac{\partial^2 w_2}{\partial z^2} \end{pmatrix}, \tag{B.17}$$

where, λ_i, represents the eigenvalues of the diffusion coefficients matrix and A is the eigenvector matrix. A new variable ϕ_i can be introduced. Its relation with the concentration, w_i, can be expressed with the inverse of the eigenvector matrix A^{-1} as

$$\begin{pmatrix} \phi_1 \\ \phi_2 \end{pmatrix} = A^{-1} \begin{pmatrix} w_1 \\ w_2 \end{pmatrix} = \begin{pmatrix} \alpha & \beta \\ \gamma & \delta \end{pmatrix} \begin{pmatrix} w_1 \\ w_2 \end{pmatrix}. \tag{B.18}$$

Using this change of variable, the system, the boundary and the initial conditions can now be written respectively in terms of ϕ_i, as follows

$$\begin{pmatrix} \frac{\partial \phi_1}{\partial t} \\ \frac{\partial \phi_2}{\partial t} \end{pmatrix} = \begin{pmatrix} \lambda_1 & 0 \\ 0 & \lambda_2 \end{pmatrix} \begin{pmatrix} \frac{\partial^2 \phi_1}{\partial z^2} \\ \frac{\partial^2 \phi_2}{\partial z^2} \end{pmatrix}, \tag{B.19}$$

$$\begin{pmatrix} \frac{\partial \phi_1(t, z=0,1)}{\partial z} \\ \frac{\partial \phi_2(t, z=0,1)}{\partial z} \end{pmatrix} = \begin{pmatrix} 0 \\ 0 \end{pmatrix}, \tag{B.20}$$

$$\begin{pmatrix}\phi_1(t=0,z)\\ \phi_2(t=0,z)\end{pmatrix} = \begin{pmatrix}\alpha & \beta\\ \gamma & \delta\end{pmatrix}\begin{pmatrix}w_{01}+S_{T1}\left(\frac{1}{2}-z\right)\\ w_{02}+S_{T2}\left(\frac{1}{2}-z\right)\end{pmatrix}, \tag{B.21}$$

where the eigenvalues, λ_1 and λ_2, are

$$\lambda_1 = \frac{(1-D_{22})+\sqrt{(1-D_{22})^2+4D_{21}D_{12}}}{2} \tag{B.22}$$

$$\lambda_2 = \frac{(1-D_{22})-\sqrt{(1-D_{22})^2+4D_{21}D_{12}}}{2} \tag{B.23}$$

and

$$\alpha = \delta = \frac{\lambda_2-1}{\lambda_2-\lambda_1} \tag{B.24}$$

$$\beta = \frac{\lambda_2-1}{\lambda_2-\lambda_1}\frac{D_{12}}{D_{12}-\lambda_2} \tag{B.25}$$

$$\gamma = \frac{\lambda_2-1}{\lambda_2-\lambda_1}\frac{1-\lambda_1}{D_{12}}. \tag{B.26}$$

The solution of the system (B.19) that satisfy the boundary condition (B.20), has the form

$$\phi_i(t,z) = \phi_{i,st}(z) + \sum_{n=1}^{\infty} A_{i,n}\cos(n\pi z)e^{(-n^2\pi^2\lambda_i t)} \qquad i=1,2, \tag{B.27}$$

where $\phi_{i,st}(z)$ is the value of ϕ_i when the system reaches the steady state. The expression of $\phi_{i,st}(z)$ is obtained by means of the steady state of the concentration field $w_{i,st}(z)$,

$$w_{i,st}(z) = w_{i,st}(t\to\infty,z) = w_{0i}. \tag{B.28}$$

The introduction of the value of $w_{i,st}(z)$ into the Equation (B.18) gives,

$$\begin{pmatrix}\phi_{1,st}(z)\\ \phi_{2,st}(z)\end{pmatrix} = \begin{pmatrix}\phi_{1,st}(t\to\infty,z)\\ \phi_{2,st}(t\to\infty,z)\end{pmatrix} = \begin{pmatrix}\alpha & \beta\\ \gamma & \delta\end{pmatrix}\begin{pmatrix}w_{01}\\ w_{02}\end{pmatrix}. \tag{B.29}$$

The constants $A_{i,n}$ are determined from the initial conditions (Equation (B.20)),

$$\begin{pmatrix} A_{1,n} \\ A_{2,n} \end{pmatrix} = -\frac{(-1)^n - 1}{n^2\pi^2} \begin{pmatrix} \alpha & \beta \\ \gamma & \delta \end{pmatrix} \begin{pmatrix} S_{T1} \\ S_{T2} \end{pmatrix}. \tag{B.30}$$

The solution of the system of Equations (B.19) with boundary (B.20) and initial (B.21) conditions is

$$\phi_1(t,z) = (\alpha w_{01} + \beta w_{02}) - \frac{\alpha S_{T1} + \beta S_{T2}}{\pi^2} \sum_{n=1}^{\infty} \frac{(-1)^n - 1}{n^2} \cos(n\pi z) e^{(-n^2\pi^2\lambda_1 t)} \tag{B.31}$$

$$\phi_1(t,z) = (\alpha w_{01} + \beta w_{02}) - \frac{\alpha S_{T1} + \beta S_{T2}}{\pi^2} \sum_{n=1}^{\infty} \frac{(-1)^n - 1}{n^2} \cos(n\pi z) e^{(-n^2\pi^2\lambda_2 t)} \tag{B.32}$$

Finally, the solution for the concentration field can be obtained by introducing the expressions (B.31)-(B.32) in

$$\begin{pmatrix} w_1(t,z) \\ w_2(t,z) \end{pmatrix} = A \begin{pmatrix} \phi_1(t,z) \\ \phi_2(t,z) \end{pmatrix} = \begin{pmatrix} 1 & \frac{D_{12}}{\lambda_2 - 1} \\ \frac{\lambda_1 - 1}{D_{12}} & 1 \end{pmatrix} \begin{pmatrix} \phi_1(t,z) \\ \phi_2(t,z) \end{pmatrix}, \tag{B.33}$$

resulting

$$w_1(t,z) = \phi_1(t,z) + \frac{D_{12}}{\lambda_2 - 1}\phi_2(t,z) \tag{B.34}$$

$$w_2(t,z) = \frac{\lambda_1 - 1}{D_{12}}\phi_1(t,z) + \phi_2(t,z). \tag{B.35}$$

Appendix C

OpenFOAM `thermoGFoam` solver

In this appendix the source code of the customized OpenFOAM *solver* `thermoGFoam` is presented.

```
thermoGFoam.C

EXE = $(FOAM_USER_APPBIN)/thermoGFoam
```

Listing C.1: File: thermoGFoam/Make/files

```
EXE_INC = \
    -I../buoyantBoussinesqSimpleFoam \
    -I$(LIB_SRC)/sampling/lnInclude \
    -I$(LIB_SRC)/meshTools/lnInclude \
    -I$(LIB_SRC)/fvOptions/lnInclude \
    -I$(LIB_SRC)/finiteVolume/lnInclude \
    -I$(LIB_SRC)/turbulenceModels \
    -I$(LIB_SRC)/turbulenceModels/incompressible/RAS/lnInclude \
    -I$(LIB_SRC)/transportModels \
    -I$(LIB_SRC)/transportModels/incompressible/singlePhaseTransportModel \
    -I$(LIB_SRC)/thermophysicalModels/radiationModels/lnInclude

EXE_LIBS = \
    -lfiniteVolume \
    -lfvOptions \
    -lsampling \
    -lmeshTools \
    -lincompressibleTurbulenceModel \
    -lincompressibleRASModels \
    -lincompressibleTransportModels \
    -lradiationModels
```

Listing C.2: File: thermoGFoam/Make/options

```
/*---------------------------------------------------------------------------*\
  =========                 |
  \\      /  F ield         | OpenFOAM: The Open Source CFD Toolbox
```

```
    \\    /   O peration     |
     \\  /    A nd           | Copyright (C) 2011-2013 OpenFOAM Foundation
      \\/     M anipulation  |
-------------------------------------------------------------------------------
License
    This file is part of OpenFOAM.

    OpenFOAM is free software: you can redistribute it and/or modify it
    under the terms of the GNU General Public License as published by
    the Free Software Foundation, either version 3 of the License, or
    (at your option) any later version.

    OpenFOAM is distributed in the hope that it will be useful, but WITHOUT
    ANY WARRANTY; without even the implied warranty of MERCHANTABILITY or
    FITNESS FOR A PARTICULAR PURPOSE.  See the GNU General Public License
    for more details.

    You should have received a copy of the GNU General Public License
    along with OpenFOAM.  If not, see <http://www.gnu.org/licenses/>.

Application
    buoyantBoussinesqPimpleFoam

Description
    Transient solver for buoyant, turbulent flow of incompressible fluids

    Uses the Boussinesq approximation:
    \f[
        rho_{k} = 1 - beta(T - T_{ref})
    \f]

    where:
        \f$ rho_{k} \f$ = the effective (driving) kinematic density
        beta = thermal expansion coefficient [1/K]
        T = temperature [K]
        \f$ T_{ref} \f$ = reference temperature [K]

    Valid when:
    \f[
        \frac{beta(T - T_{ref})}{rho_{ref}} << 1
    \f]

\*---------------------------------------------------------------------------*/

#include "fvCFD.H"
#include "singlePhaseTransportModel.H"
//#include "RASModel.H"
//#include "radiationModel.H"
#include "fvIOoptionList.H"
#include "pimpleControl.H"
#include "fixedFluxPressureFvPatchScalarField.H"

// * * * * * * * * * * * * * * * * * * * * * * * * * * * * * * * * * * * * * //

int main(int argc, char *argv[])
{
    #include "setRootCase.H"
    #include "createTime.H"
    #include "createMesh.H"
    #include "readGravitationalAcceleration.H"
```

```
    #include "createFields.H"
//    #include "createIncompressibleRadiationModel.H"
    #include "createFvOptions.H"
    #include "initContinuityErrs.H"
    #include "readTimeControls.H"
    #include "CourantNo.H"
    #include "setInitialDeltaT.H"
    #include "readPISOControls.H"

    pimpleControl pimple(mesh);

    // * * * * * * * * * * * * * * * * * * * * * * * * * * * * * * * * * * * * //

    Info<< "\nStarting time loop\n" << endl;

    dimensionedVector gravity;
    fileName caseDir = runTime.constant();
    IFstream dataStream(caseDir/"gravity");

    while (runTime.loop())
    {

//*********************************************************************
//*********************************************************************

    Info<< "\nReading gravity" << endl;

    dataStream >> gravity;

    g = gravity;

    Info<< "Calculating field g.h\n" << endl;
    volScalarField gh("gh", g & mesh.C());
    surfaceScalarField ghf("ghf", g & mesh.Cf());

    volScalarField p
    (
        IOobject
        (
            "p",
            runTime.timeName(),
            mesh,
            IOobject::NO_READ,
            IOobject::AUTO_WRITE
        ),
        p_rgh + rhok*gh
    );

    label pRefCell = 0;
    scalar pRefValue = 0.0;
    setRefCell
    (
        p,
        p_rgh,
        mesh.solutionDict().subDict("PIMPLE"),
        pRefCell,
        pRefValue
    );

    if (p_rgh.needReference())
```

```
    {
125         p += dimensionedScalar
            (
127             "p",
                p.dimensions(),
129             pRefValue - getRefCellValue(p, pRefCell)
            );
131     }

133     Info<< "\ngravity = " << g << nl << endl;

135 //***************************************************************
    //***************************************************************
137
            Info<< "Time = " << runTime.timeName() << nl << endl;
139
            #include "readTimeControls.H"
141         #include "CourantNo.H"
            #include "setDeltaT.H"
143
            // --- Pressure-velocity PIMPLE corrector loop
145         while (pimple.loop())
            {
147             #include "UEqn.H"

149         for (int corr=0; corr<nCorr; corr++)
            {
151             #include "w1Eqn.H"

153             #include "w2Eqn.H"
    }
155
            w3 = 1 - w1 - w2;
157
                #include "TEqn.H"
159
                rhok = 1.0 + beta1*(w1 - w1Ref) + beta2*(w2 - w2Ref)
161             - betaT*(T - TRef);

163             // --- Pressure corrector loop
                while (pimple.correct())
165             {
                    #include "pEqn.H"
167             }

169         }

171         runTime.write();

173         Info<< "ExecutionTime = " << runTime.elapsedCpuTime() << " s"
                << "  ClockTime = " << runTime.elapsedClockTime() << " s"
175             << nl << endl;

177     }

179     Info<< "End\n" << endl;

181     return 0;
}
183
```

```
185 // ************************************************************************* //
```

LISTING C.3: File: thermoGFoam/thermoGFoam.C

```
1     Info<< "Reading thermophysical properties\n" << endl;

3     Info<< "Reading field T\n" << endl;
      volScalarField T
5     (
          IOobject
7         (
              "T",
9             runTime.timeName(),
              mesh,
11            IOobject::MUST_READ,
              IOobject::AUTO_WRITE
13        ),
          mesh
15    );

17    Info<< "Reading field w1\n" << endl;
      volScalarField w1
19    (
          IOobject
21        (
              "w1",
23            runTime.timeName(),
              mesh,
25            IOobject::MUST_READ,
              IOobject::AUTO_WRITE
27        ),
          mesh
29    );

31    Info<< "Reading field w2\n" << endl;
      volScalarField w2
33    (
          IOobject
35        (
              "w2",
37            runTime.timeName(),
              mesh,
39            IOobject::MUST_READ,
              IOobject::AUTO_WRITE
41        ),
          mesh
43    );

45    Info<< "Reading field w3\n" << endl;
      volScalarField w3
47    (
          IOobject
49        (
              "w3",
51            runTime.timeName(),
              mesh,
53            IOobject::MUST_READ,
              IOobject::AUTO_WRITE
55        ),
```

```
        mesh
    );

    Info<< "Reading field p_rgh\n" << endl;
    volScalarField p_rgh
    (
        IOobject
        (
            "p_rgh",
            runTime.timeName(),
            mesh,
            IOobject::MUST_READ,
            IOobject::AUTO_WRITE
        ),
        mesh
    );

    Info<< "Reading field U\n" << endl;
    volVectorField U
    (
        IOobject
        (
            "U",
            runTime.timeName(),
            mesh,
            IOobject::MUST_READ,
            IOobject::AUTO_WRITE
        ),
        mesh
    );

    #include "createPhi.H"

    #include "readTransportProperties.H"

    // Kinematic density for buoyancy force
    volScalarField rhok
    (
        IOobject
        (
            "rhok",
            runTime.timeName(),
            mesh
        ),
        1.0 + beta1*(w1 - w1Ref) + beta2*(w2 - w2Ref) - betaT*(T - TRef)
    );

IOdictionary pathFile
(
    IOobject
    (
        "pathFile",
        runTime.constant(),
        mesh,
        IOobject::NO_READ,
        IOobject::NO_WRITE
    )
);
```

Listing C.4: File: thermoGFoam/createFields.H

```
    singlePhaseTransportModel laminarTransport(U, phi);

    // Kinematic viscosity
    dimensionedScalar nu(laminarTransport.lookup("nu"));

    // Concentration expansion coefficient component 1
    dimensionedScalar beta1(laminarTransport.lookup("beta1"));

    // Concentration expansion coefficient component 2
    dimensionedScalar beta2(laminarTransport.lookup("beta2"));

    // Self diffusion coefficient component 1
    dimensionedScalar D11(laminarTransport.lookup("D11"));

    // Self diffusion coefficient component 2
    dimensionedScalar D22(laminarTransport.lookup("D22"));

    // Cross diffusion coefficient component 1
    dimensionedScalar D12(laminarTransport.lookup("D12"));

    // Cross diffusion coefficient component 2
    dimensionedScalar D21(laminarTransport.lookup("D21"));

    // Reference concentration w1Ref
    dimensionedScalar w1Ref(laminarTransport.lookup("w1Ref"));

    // Reference concentration w2Ref
    dimensionedScalar w2Ref(laminarTransport.lookup("w2Ref"));

    // Thermal expansion coefficient [1/K]
    dimensionedScalar betaT(laminarTransport.lookup("betaT"));

    // Reference temperature [K]
    dimensionedScalar TRef(laminarTransport.lookup("TRef"));

    // Thermodiffusion coefficient component 1
    dimensionedScalar DT1(laminarTransport.lookup("DT1"));

    // Thermodiffusion coefficient component 2
    dimensionedScalar DT2(laminarTransport.lookup("DT2"));

    // Thermal diffusion coefficient
    dimensionedScalar alpha(laminarTransport.lookup("alpha"));

    // Laminar Prandtl number
//    dimensionedScalar Pr(laminarTransport.lookup("Pr"));

    // Turbulent Prandtl number
//    dimensionedScalar Prt(laminarTransport.lookup("Prt"));
```

Listing C.5: File: thermoGFoam/readTransportProperties.H

```
{
    fvScalarMatrix w1Eqn
    (
        fvm::ddt(w1)
      + fvm::div(phi, w1)
      - fvm::laplacian(D11, w1)
      - fvc::laplacian(D12, w2)
      - fvc::laplacian(DT1, T)
```

```
    );

    w1Eqn.relax();

    fvOptions.constrain(w1Eqn);

    w1Eqn.solve();

    fvOptions.correct(w1);

}
```

Listing C.6: File: thermoGFoam/thermoGFoam/w1Eqn.H

```
{
    fvScalarMatrix w2Eqn
    (
        fvm::ddt(w2)
      + fvm::div(phi, w2)
      - fvm::laplacian(D22, w2)
      - fvc::laplacian(D21, w1)
      - fvc::laplacian(DT2, T)
    );

    w2Eqn.relax();

    fvOptions.constrain(w2Eqn);

    w2Eqn.solve();

    fvOptions.correct(w2);

}
```

Listing C.7: File: thermoGFoam/thermoGFoam/w2Eqn.H

```
    // Solve the momentum equation

    fvVectorMatrix UEqn
    (
        fvm::ddt(U)
      + fvm::div(phi, U)
      - fvm::laplacian(nu, U)
     ==
        fvOptions(U)
    );

    UEqn.relax();

    fvOptions.constrain(UEqn);

    if (pimple.momentumPredictor())
    {
        solve
        (
            UEqn
         ==
            fvc::reconstruct
            (
```

```
                (
                  - ghf*fvc::snGrad(rhok)
                  - fvc::snGrad(p_rgh)
                )*mesh.magSf()
            )
        );

        fvOptions.correct(U);
    }
```

LISTING C.8: File: thermoGFoam/UEqn.H

```
{
    fvScalarMatrix TEqn
    (
        fvm::ddt(T)
      + fvm::div(phi, T)
      - fvm::laplacian(alpha, T)
//     ==
//        radiation->ST(rhoCpRef, T)
//      + fvOptions(T)
    );

    TEqn.relax();

    fvOptions.constrain(TEqn);

    TEqn.solve();

//    radiation->correct();

    fvOptions.correct(T);

}
```

LISTING C.9: File: thermoGFoam/TEqn.C

```
{
    volScalarField rAU("rAU", 1.0/UEqn.A());
    surfaceScalarField rAUf("rAUf", fvc::interpolate(rAU));

    volVectorField HbyA("HbyA", U);
    HbyA = rAU*UEqn.H();

    surfaceScalarField phig(-rAUf*ghf*fvc::snGrad(rhok)*mesh.magSf());

    surfaceScalarField phiHbyA
    (
        "phiHbyA",
        (fvc::interpolate(HbyA) & mesh.Sf())
      + rAUf*fvc::ddtCorr(U, phi)
      + phig
    );

    // Update the fixedFluxPressure BCs to ensure flux consistency
    setSnGrad<fixedFluxPressureFvPatchScalarField>
    (
        p_rgh.boundaryField(),
        (
```

```
            phiHbyA.boundaryField()
          - (mesh.Sf().boundaryField() & U.boundaryField())
        )/(mesh.magSf().boundaryField()*rAUf.boundaryField())
    );

    while (pimple.correctNonOrthogonal())
    {
        fvScalarMatrix p_rghEqn
        (
            fvm::laplacian(rAUf, p_rgh) == fvc::div(phiHbyA)
        );

        p_rghEqn.setReference(pRefCell, getRefCellValue(p_rgh, pRefCell));

        p_rghEqn.solve(mesh.solver(p_rgh.select(pimple.finalInnerIter())));

        if (pimple.finalNonOrthogonalIter())
        {
            // Calculate the conservative fluxes
            phi = phiHbyA - p_rghEqn.flux();

            // Explicitly relax pressure for momentum corrector
            p_rgh.relax();

            // Correct the momentum source with the pressure gradient flux
            // calculated from the relaxed pressure
            U = HbyA + rAU*fvc::reconstruct((phig - p_rghEqn.flux())/rAUf);
            U.correctBoundaryConditions();
            fvOptions.correct(U);
        }
    }

    #include "continuityErrs.H"

    p = p_rgh + rhok*gh;

    if (p_rgh.needReference())
    {
        p += dimensionedScalar
        (
            "p",
            p.dimensions(),
            pRefValue - getRefCellValue(p, pRefCell)
        );
        p_rgh = p - rhok*gh;
    }
}
```

Listing C.10: File: thermoGFoam/pEqn.C

Appendix D

OpenFOAM `thermoGFoam` case set up

In this appendix setup case for using `thermoGFoam` is presented. The structure of a typical DCMIX case is shown in Figure D.1.

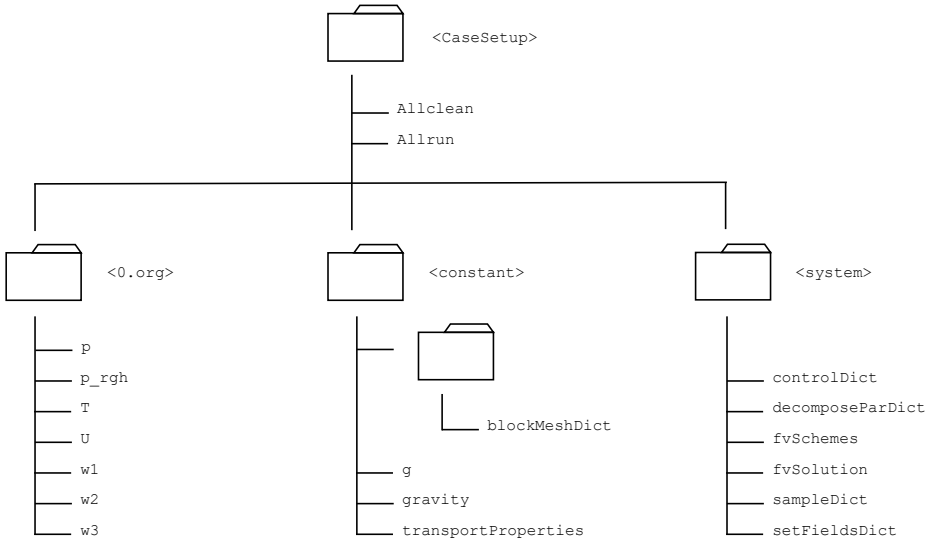

FIGURE D.1: OpenFOAM DCMIX typical case structure

```
#!/bin/sh
cd ${0%/*} || exit 1    # run from this directory

# Clean time directories only

rm -rf 0 > /dev/null 2>&1

rm -rf *[1-9]*
rm -f log.* 2>/dev/null
rm -r processor*
rm -r postProcessing
```

```

# ------------------------------------------------------------ end-of-file
```

LISTING D.1: File: DCMIX2case/Allclean

```
#!/bin/sh
cd ${0%/*} || exit 1    # run from this directory

# Source tutorial run functions
. $WM_PROJECT_DIR/bin/tools/RunFunctions

cp -r 0.org 0 > /dev/null 2>&1

runApplication blockMesh

#runApplication setFields

# For not parallel running
#application=`getApplication`
#runApplication $application

# For parallel running
runApplication decomposePar
runParallel $(getApplication) 3
runApplication reconstructPar

# ------------------------------------------------------------ end-of-file
```

LISTING D.2: File: DCMIX2case/Allrun

```
/*--------------------------------*- C++ -*----------------------------------*\
| =========                 |                                                 |
| \\      /  F ield         | OpenFOAM: The Open Source CFD Toolbox           |
|  \\    /   O peration     | Version:  2.3.0                                 |
|   \\  /    A nd           | Web:      www.OpenFOAM.org                      |
|    \\/     M anipulation  |                                                 |
\*---------------------------------------------------------------------------*/
FoamFile
{
    version     2.0;
    format      ascii;
    class       volScalarField;
    object      p;
}
// * * * * * * * * * * * * * * * * * * * * * * * * * * * * * * * * * * * * //

dimensions      [0 2 -2 0 0 0 0];

internalField   uniform 0;

boundaryField
{
    top
    {
        type            calculated;
        value           $internalField;
    }

    bottom
```

```
    {
        type            calculated;
        value           $internalField;
    }

    front
    {
        type            calculated;
        value           $internalField;
    }

    back
    {
        type            calculated;
        value           $internalField;
    }

    west
    {
        type            calculated;
        value           $internalField;
    }

    east
    {
        type            calculated;
        value           $internalField;
    }
}

// ************************************************************************* //
```

Listing D.3: File: DCMIX2case/0.org/p

```
/*--------------------------------*- C++ -*----------------------------------*\
| =========                 |                                                 |
| \\      /  F ield         | OpenFOAM: The Open Source CFD Toolbox           |
|  \\    /   O peration     | Version:  2.3.0                                 |
|   \\  /    A nd           | Web:      www.OpenFOAM.org                      |
|    \\/     M anipulation  |                                                 |
\*---------------------------------------------------------------------------*/
FoamFile
{
    version     2.0;
    format      ascii;
    class       volScalarField;
    object      p_rgh;
}
// * * * * * * * * * * * * * * * * * * * * * * * * * * * * * * * * * * * * * //

dimensions      [0 2 -2 0 0 0 0];

internalField   uniform 0;

boundaryField
{
    top
    {
        type            fixedFluxPressure;
        rho             rhok;
```

```
        value           uniform 0;
    }

    bottom
    {
        type            fixedFluxPressure;
        rho             rhok;
        value           uniform 0;
    }

    front
    {
        type            fixedFluxPressure;
        rho             rhok;
        value           uniform 0;
    }

    back
    {
        type            fixedFluxPressure;
        rho             rhok;
        value           uniform 0;
    }

    west
    {
        type            fixedFluxPressure;
        rho             rhok;
        value           uniform 0;
    }

    east
    {
        type            fixedFluxPressure;
        rho             rhok;
        value           uniform 0;
    }

}

// ************************************************************************* //
```

Listing D.4: File: DCMIX2case/0.org/p_rgh

```
/*--------------------------------*- C++ -*----------------------------------*\
| =========                 |                                                 |
| \\      /  F ield         | OpenFOAM: The Open Source CFD Toolbox           |
|  \\    /   O peration     | Version:  2.3.0                                 |
|   \\  /    A nd           | Web:      www.OpenFOAM.org                      |
|    \\/     M anipulation  |                                                 |
\*---------------------------------------------------------------------------*/
FoamFile
{
    version     2.0;
    format      ascii;
    class       volScalarField;
    location    "0";
    object      T;
}
// * * * * * * * * * * * * * * * * * * * * * * * * * * * * * * * * * * * * * //
```

```
17
dimensions      [0 0 0 1 0 0 0];
19
internalField   uniform 5;
21
boundaryField
23 {
    top
25  {
        type            fixedValue;
27      value           uniform 10;
    }
29
    bottom
31  {
        type            fixedValue;
33      value           uniform 0;
    }
35
    front
37  {
        type            zeroGradient;
39  }

41  back
    {
43      type            zeroGradient;
    }
45
    west
47  {
        type            zeroGradient;
49  }

51  east
    {
53      type            zeroGradient;
    }
55 }

57

// ************************************************************************* //
```

Listing D.5: File: DCMIX2case/0.org/T

```
/*--------------------------------*- C++ -*----------------------------------*\
2 | =========                 |                                                 |
  | \\      /  F ield         | OpenFOAM: The Open Source CFD Toolbox           |
4 |  \\    /   O peration     | Version:  2.3.0                                 |
  |   \\  /    A nd           | Web:      www.OpenFOAM.org                      |
6 |    \\/     M anipulation  |                                                 |
  \*---------------------------------------------------------------------------*/
8 FoamFile
  {
10    version     2.0;
      format      ascii;
12    class       volVectorField;
      object      U;
14 }
  // * * * * * * * * * * * * * * * * * * * * * * * * * * * * * * * * * * * * //
```

```

dimensions      [0 1 -1 0 0 0 0];

internalField   uniform (0 0 0);

boundaryField
{
    top
    {
        type            fixedValue;
        value           uniform (0 0 0);
    }

    bottom
    {
        type            fixedValue;
        value           uniform (0 0 0);
    }

    front
    {
        type            fixedValue;
        value           uniform (0 0 0);
    }

    back
    {
        type            fixedValue;
        value           uniform (0 0 0);
    }

    west
    {
        type            fixedValue;
        value           uniform (0 0 0);
    }

    east
    {
        type            fixedValue;
        value           uniform (0 0 0);
    }

}

// ************************************************************************* //
```

Listing D.6: File: DCMIX2case/0.org/U

```
/*--------------------------------*- C++ -*----------------------------------*\
| =========                 |                                                 |
| \\      /  F ield         | OpenFOAM: The Open Source CFD Toolbox           |
|  \\    /   O peration     | Version:  2.3.0                                 |
|   \\  /    A nd           | Web:      www.OpenFOAM.org                      |
|    \\/     M anipulation  |                                                 |
\*---------------------------------------------------------------------------*/
FoamFile
{
    version     2.0;
    format      ascii;
```

```
    class       volScalarField;
    object      w1;
}
// * * * * * * * * * * * * * * * * * * * * * * * * * * * * * * * * * * * * * * * * //

dimensions      [0 0 0 0 0 0 0];

internalField   uniform 0.62;

boundaryField
{
    top
    {
        type            groovyBC;
        refValue        uniform 0;
        refGradient     uniform 0;
        valueFraction   uniform 0;
        value           uniform 0.62;
        valueExpression "0";
        gradientExpression "-(-2.956242995525823e-04*snGrad(T)
                            + 0.660092958603015*snGrad(w2))";
        variables       "";
        fractionExpression "0";
        evaluateDuringConstruction 0;

        timelines       (
);
        lookuptables    (
);
    }

    bottom
    {
        type            groovyBC;
        refValue        uniform 0;
        refGradient     uniform 0;
        valueFraction   uniform 0;
        value           uniform 0.62;
        valueExpression "0";
        gradientExpression "-(-2.956242995525823e-04*snGrad(T)
                            + 0.660092958603015*snGrad(w2))";
        variables       "";
        fractionExpression "0";
        evaluateDuringConstruction 0;

        timelines       (
);
        lookuptables    (
);
    }

    front
    {
        type            zeroGradient;
    }

    back
    {
        type            zeroGradient;
    }
```

```
    west
    {
        type            zeroGradient;
    }

    east
    {
        type            zeroGradient;
    }

}

// ************************************************************************* //
```

LISTING D.7: File: DCMIX2case/0.org/w1

```
/*--------------------------------*- C++ -*----------------------------------*\
| =========                 |                                                 |
| \\      /  F ield         | OpenFOAM: The Open Source CFD Toolbox           |
|  \\    /   O peration     | Version:  2.3.0                                 |
|   \\  /    A nd           | Web:      www.OpenFOAM.org                      |
|    \\/     M anipulation  |                                                 |
\*---------------------------------------------------------------------------*/
FoamFile
{
    version     2.0;
    format      ascii;
    class       volScalarField;
    object      w2;
}
// * * * * * * * * * * * * * * * * * * * * * * * * * * * * * * * * * * * * //

dimensions      [0 0 0 0 0 0 0];

internalField   uniform 0.31;

boundaryField
{
    top
    {
        type            groovyBC;
        refValue        uniform 0;
        refGradient     uniform 0;
        valueFraction   uniform 0;
        value           uniform 0.31;
        valueExpression "0";
        gradientExpression "-(-0.001329453361834*snGrad(T)
                            + -0.466187329965022*snGrad(w1))";
        variables       "";
        fractionExpression "0";
        evaluateDuringConstruction 0;

        timelines       (
);
        lookuptables    (
);
    }

    bottom
```

```
    {
        type            groovyBC;
        refValue        uniform 0;
        refGradient     uniform 0;
        valueFraction   uniform 0;
        value           uniform 0.31;
        valueExpression "0";
        gradientExpression "-(-0.001329453361834*snGrad(T)
                            + -0.466187329965022*snGrad(w1))";
        variables       "";
        fractionExpression "0";
        evaluateDuringConstruction 0;

        timelines       (
);
        lookuptables    (
);
    }

    front
    {
        type            zeroGradient;
    }

    back
    {
        type            zeroGradient;
    }

    west
    {
        type            zeroGradient;
    }

    east
    {
        type            zeroGradient;
    }

}

// ************************************************************************* //
```

LISTING D.8: File: DCMIX2case/0.org/w2

```
/*--------------------------------*- C++ -*----------------------------------*\
| =========                 |                                                 |
| \\      /  F ield         | OpenFOAM: The Open Source CFD Toolbox           |
|  \\    /   O peration     | Version:  2.3.0                                 |
|   \\  /    A nd           | Web:      www.OpenFOAM.org                      |
|    \\/     M anipulation  |                                                 |
\*---------------------------------------------------------------------------*/
FoamFile
{
    version     2.0;
    format      ascii;
    class       volScalarField;
    object      w3;
}
// * * * * * * * * * * * * * * * * * * * * * * * * * * * * * * * * * * * * * //
```

```
dimensions      [0 0 0 0 0 0 0];

internalField   uniform 0.07;

boundaryField
{
    top
    {
        type            zeroGradient;
    }

    bottom
    {
        type            zeroGradient;
    }

    front
    {
        type            zeroGradient;
    }

    back
    {
        type            zeroGradient;
    }

    west
    {
        type            zeroGradient;
    }

    east
    {
        type            zeroGradient;
    }

}

// ************************************************************************* //
```

Listing D.9: File: DCMIX2case/0.org/w3

```
/*--------------------------------*- C++ -*----------------------------------*\
| =========                 |                                                 |
| \\      /  F ield         | OpenFOAM: The Open Source CFD Toolbox           |
|  \\    /   O peration     | Version:  2.3.0                                 |
|   \\  /    A nd           | Web:      www.OpenFOAM.org                      |
|    \\/     M anipulation  |                                                 |
\*---------------------------------------------------------------------------*/
FoamFile
{
    version     2.0;
    format      ascii;
    class       dictionary;
    object      blockMeshDict;
}
// * * * * * * * * * * * * * * * * * * * * * * * * * * * * * * * * * * * * * //

convertToMeters 0.001;
```

```
19 vertices
   (
21     (0 0 0)
       (10 0 0)
23     (10 10 0)
       (0 10 0)
25     (0 0 5)
       (10 0 5)
27     (10 10 5)
       (0 10 5)
29 );

31 blocks
   (
33     hex (0 1 2 3 4 5 6 7) (40 40 20) simpleGrading (1 1 1)
   );
35
   edges
37 (
   );
39
   boundary
41 (
       top
43     {
           type wall;
45         faces
           (
47             (4 5 6 7)
           );
49     }

51     bottom
       {
53         type wall;
           faces
55         (
               (0 3 2 1)
57         );
       }
59
       front
61     {
           type wall;
63         faces
           (
65             (0 1 5 4)
           );
67     }

69     back
       {
71         type wall;
           faces
73         (
               (3 2 6 7)
75         );
       }
77
```

```
    west
    {
        type wall;
        faces
        (
            (0 4 7 3)
        );
    }

    east
    {
        type wall;
        faces
        (
            (1 2 6 5)
        );
    }
);

mergePatchPairs
(
);

// ************************************************************************* //
```

Listing D.10: File: DCMIX2case/constant/polyMesh/blockMeshDict

```
/*--------------------------------*- C++ -*----------------------------------*\
| =========                 |                                                 |
| \\      /  F ield         | OpenFOAM: The Open Source CFD Toolbox           |
|  \\    /   O peration     | Version:  2.3.0                                 |
|   \\  /    A nd           | Web:      www.OpenFOAM.org                      |
|    \\/     M anipulation  |                                                 |
\*---------------------------------------------------------------------------*/
FoamFile
{
    version     2.0;
    format      ascii;
    class       uniformDimensionedVectorField;
    location    "constant";
    object      g;
}
// * * * * * * * * * * * * * * * * * * * * * * * * * * * * * * * * * * * * * //

dimensions      [0 1 -2 0 0 0 0];
value           ( 0 9.81 0 );


// ************************************************************************* //
```

Listing D.11: File: DCMIX2case/constant/g

```
[0 1 -2 0 0 0 0] ( -2.740129200e-04 -1.102644000e-03 -1.308359700e-03 )
[0 1 -2 0 0 0 0] ( -2.737186200e-04 -1.270983600e-03 -1.581470100e-03 )
[0 1 -2 0 0 0 0] ( -2.534511600e-04 -1.388605500e-03 -1.754616600e-03 )
[0 1 -2 0 0 0 0] ( -2.114545500e-04 -1.410187500e-03 -1.605308400e-03 )
[0 1 -2 0 0 0 0] ( -1.362707100e-04 -1.315913400e-03 -1.203098400e-03 )
[0 1 -2 0 0 0 0] ( -9.398078100e-06 -1.105292700e-03 -8.718147000e-04 )
[0 1 -2 0 0 0 0] ( 1.556552700e-04 -8.035371000e-04 -8.4186477000e-04 )
```

```
        .               .                   .                   .
        .               .                   .                   .
        .               .                   .                   .
        .               .                   .                   .

[0 1 -2 0 0 0 0] ( 3.486081600e-04 -4.6432692000e-04 -1.096071300e-03 )
[0 1 -2 0 0 0 0] ( 5.421496500e-04 -1.6520040000e-04 -1.465221600e-03 )
[0 1 -2 0 0 0 0] ( 7.069086000e-04 3.52424250000e-06 -1.763445600e-03 )
[0 1 -2 0 0 0 0] ( 8.082360900e-04 1.49779080000e-05 -1.908437400e-03 )
[0 1 -2 0 0 0 0] ( 8.399518200e-04 -6.4758753000e-05 -2.005262100e-03 )
[0 1 -2 0 0 0 0] ( 7.580088900e-04 -1.2554838000e-04 -2.204012700e-03 )
[0 1 -2 0 0 0 0] ( 5.019188400e-04 -1.4889618000e-04 -2.499195600e-03 )
[0 1 -2 0 0 0 0] ( 1.729797300e-04 -2.8899279000e-04 -2.782017900e-03 )
[0 1 -2 0 0 0 0] ( -7.07791500e-05 -5.2027335000e-04 -2.894342400e-03 )
[0 1 -2 0 0 0 0] ( -1.80621720e-04 -7.1630658000e-04 -2.539710900e-03 )
```

Listing D.12: File: DCMIX2case/constant/gravity

```
/*--------------------------------*- C++ -*----------------------------------*\
| =========                 |                                                 |
| \\      /  F ield         | OpenFOAM: The Open Source CFD Toolbox           |
|  \\    /   O peration     | Version:  2.3.0                                 |
|   \\  /    A nd           | Web:      www.OpenFOAM.org                      |
|    \\/     M anipulation  |                                                 |
\*---------------------------------------------------------------------------*/
FoamFile
{
    version     2.0;
    format      ascii;
    class       dictionary;
    object      transportProperties;
}

// * * * * * * * * * * * * * * * * * * * * * * * * * * * * * * * * * * * * //

transportModel Newtonian;

// Laminar viscosity
nu              nu [0 2 -1 0 0 0 0] 6.6989e-07;

// Concentration expansion coefficient component 1
beta1           beta1 [0 0 0 0 0 0 0] 0.1368;

// Concentration expansion coefficient component 2
beta2           beta2 [0 0 0 0 0 0 0] 0.0449;

// Self diffusion coefficient component 1
D11             D11 [0 2 -1  0 0 0 0] 2.30e-9;

// Self diffusion coefficient component 2
D22             D22 [0 2 -1  0 0 0 0] 0.51e-9;

// Cross diffusion coefficient component 1
D12             D12 [0 2 -1  0 0 0 0] 1.52e-9;

// Cross diffusion coefficient component 1
D21             D21 [0 2 -1  0 0 0 0] -0.24e-9;

// Reference concentration w1
w1Ref            w1Ref [0 0 0 0 0 0 0] 0.62;
```

```
// Reference concentration w2
w2Ref            w2Ref [0 0 0 0 0 0 0] 0.31;

// Thermal expansion coefficient
betaT           betaT [0 0 0 -1 0 0 0] 1.1568e-3;

// Reference temperature
TRef            TRef [0 0 0 1 0 0 0] 5;

// Thermodiffusion coefficient component 1
DT1             DT1 [0 2 -1  -1 0 0 0] -6.806e-13;

// Thermodiffusion coefficient component 2
DT2             DT2 [0 2 -1  -1 0 0 0] -6.841e-13;

// Thermal diffusion coefficient
alpha             alpha [0 2 -1 0 0 0 0] 1e-7;


// ************************************************************************* //
```

LISTING D.13: File: DCMIX2case/constant/transportProperties

```
/*--------------------------------*- C++ -*----------------------------------*\
| =========                 |                                                 |
| \\      /  F ield         | OpenFOAM: The Open Source CFD Toolbox           |
|  \\    /   O peration     | Version:  2.3.0                                 |
|   \\  /    A nd           | Web:      www.OpenFOAM.org                      |
|    \\/     M anipulation  |                                                 |
\*---------------------------------------------------------------------------*/
FoamFile
{
    version     2.0;
    format      ascii;
    class       dictionary;
    location    "system";
    object      controlDict;
}
// * * * * * * * * * * * * * * * * * * * * * * * * * * * * * * * * * * * * * //

application     thermoGFoam;

startFrom       startTime;

startTime       0;

stopAt          endTime;

endTime         25000;

deltaT          0.1;

writeControl    runTime;

writeInterval   500;

purgeWrite      0;

writeFormat     ascii;
```

```
37
writePrecision  16;
39
writeCompression off;
41
timeFormat      general;
43
timePrecision   6;
45
runTimeModifiable true;
47
adjustTimeStep  no;
49
maxCo           0.5;
51
libs ( "libOpenFOAM.so" );
53
functions
55 {

57     topAverage
       {
59         type faceSource;
           functionObjectLibs ("libfieldFunctionObjects.so");
61         outputControl timeStep;
           writeInterval   1;
63         log yes;
           valueOutput true;
65         source patch;
           surfaceFormat null;
67         verbose true;
           sourceName top; // replace this with your boundary patch name
69         operation average;

71         fields
           (
73             w1
               w2
75         );
       }
77
       bottomAverage
79     {
           type faceSource;
81         functionObjectLibs ("libfieldFunctionObjects.so");
           outputControl timeStep;
83         writeInterval   1;
           log yes;
85         valueOutput true;
           source patch;
87         surfaceFormat null;
           verbose true;
89         sourceName bottom; // replace this with your boundary patch name
           operation average;
91
           fields
93         (
               w1
95             w2
           );
```

```
    }

    MinMax
    {
        type            fieldMinMax;
        functionObjectLibs ("libsampling.so");
        outputControl   timeStep;
        outputInterval  1;

        fixedLocations  false;
        fields
        (
        U
        );
    }


}

libs ( "libOpenFOAM.so" "libgroovyBC.so" ) ;

// ************************************************************************* //
```

LISTING D.14: File: DCMIX2case/system/controlDict

```
/*--------------------------------*- C++ -*----------------------------------*\
| =========                 |                                                 |
| \\      /  F ield         | OpenFOAM: The Open Source CFD Toolbox           |
|  \\    /   O peration     | Version:  2.3.0                                 |
|   \\  /    A nd           | Web:      www.OpenFOAM.org                      |
|    \\/     M anipulation  |                                                 |
\*---------------------------------------------------------------------------*/
FoamFile
{
    version     2.0;
    format      ascii;
    class       dictionary;
    location    "system";
    object      decomposeParDict;
}
// * * * * * * * * * * * * * * * * * * * * * * * * * * * * * * * * * * * * * //

numberOfSubdomains 3;

method          simple;

simpleCoeffs
{
    n               ( 3 1 1 );
    delta           0.001;
}

hierarchicalCoeffs
{
    n               ( 1 1 1 );
    delta           0.001;
    order           xyz;
}

manualCoeffs
```

```
{
    dataFile        "";
}

distributed     no;

roots           ( );


// ************************************************************************* //
```

LISTING D.15: File: DCMIX2case/system/decomposeParDict

```
/*--------------------------------*- C++ -*----------------------------------*\
| =========                 |                                                 |
| \\      /  F ield         | OpenFOAM: The Open Source CFD Toolbox           |
|  \\    /   O peration     | Version:  2.3.0                                 |
|   \\  /    A nd           | Web:      www.OpenFOAM.org                      |
|    \\/     M anipulation  |                                                 |
\*---------------------------------------------------------------------------*/
FoamFile
{
    version     2.0;
    format      ascii;
    class       dictionary;
    location    "system";
    object      fvSchemes;
}
// * * * * * * * * * * * * * * * * * * * * * * * * * * * * * * * * * * * * //

ddtSchemes
{
    default         CrankNicolson 0.9;
}

gradSchemes
{
    default         cellLimited Gauss linear 1;
    grad(p)         cellLimited Gauss linear 1;
}

divSchemes
{
    default          Gauss linear;
    div(phi,U)       Gauss limitedLinear 1;
    div(phi,w1)      Gauss vanLeer01;
    div(phi,w2)      Gauss vanLeer01;
//    div(phi,T)      Gauss upwind;
//    div(phi,k)      Gauss upwind;
//    div(phi,epsilon) Gauss upwind;
//    div(phi,R)      Gauss upwind;
//    div(R)          Gauss linear;
//    div((nuEff*dev(T(grad(U))))) Gauss linear;
}

laplacianSchemes
{
    default         Gauss linear corrected;
}

```

```
interpolationSchemes
{
    default         linear;
}

snGradSchemes
{
    default         corrected;
}

fluxRequired
{
    default         no;
    p_rgh;
}


// ************************************************************************* //
```

LISTING D.16: File: DCMIX2case/system/fvSchemes

```
/*--------------------------------*- C++ -*----------------------------------*\
| =========                 |                                                 |
| \\      /  F ield         | OpenFOAM: The Open Source CFD Toolbox           |
|  \\    /   O peration     | Version:  2.3.0                                 |
|   \\  /    A nd           | Web:      www.OpenFOAM.org                      |
|    \\/     M anipulation  |                                                 |
\*---------------------------------------------------------------------------*/
FoamFile
{
    version     2.0;
    format      ascii;
    class       dictionary;
    location    "system";
    object      fvSolution;
}
// * * * * * * * * * * * * * * * * * * * * * * * * * * * * * * * * * * * * //

solvers
{
    p_rgh
    {
        solver          PCG;
        preconditioner  DIC;
        tolerance       1e-15;
        relTol          0.01;
    }

    p_rghFinal
    {
        $p_rgh;
        relTol          0;
    }

    w1
    {
        solver          PBiCG;
        preconditioner  DILU;
        tolerance       1e-15;
        relTol          0.01;
```

```
    }

    w1Final
    {
        $w1;
        relTol          0;
    }

    w2
    {
        solver          PBiCG;
        preconditioner  DILU;
        tolerance       1e-15;
        relTol          0.01;
    }

    w2Final
    {
        $w2;
        relTol          0;
    }


    "(U|T|k|epsilon|R)"
    {
        solver          PBiCG;
        preconditioner  DILU;
        tolerance       1e-15;
        relTol          0.1;
    }

    "(U|T|k|epsilon|R)Final"
    {
        $U;
        relTol          0;
    }
}

PIMPLE
{
    momentumPredictor no;
    nOuterCorrectors 1;
    nCorrectors     2;
    nNonOrthogonalCorrectors 0;
    pRefCell        0;
    pRefValue       0;
}
PISO
{
    nCorrectors     2;
    nNonOrthogonalCorrectors 0;
    pRefCell        0;
    pRefValue       0;
}

relaxationFactors
{
    fields
    {
```

```
    }
    equations
    {
        "(U|T|k|epsilon|R)" 1;
        "(U|T|k|epsilon|R)Final" 1;
    }
}

// ************************************************************************* //
```

LISTING D.17: File: DCMIX2case/system/fvSolution

```
/*--------------------------------*- C++ -*----------------------------------*\
| =========                 |                                                 |
| \\      /  F ield         | OpenFOAM: The Open Source CFD Toolbox           |
|  \\    /   O peration     | Version:  2.3.0                                 |
|   \\  /    A nd           | Web:      www.OpenFOAM.org                      |
|    \\/     M anipulation  |                                                 |
\*---------------------------------------------------------------------------*/
FoamFile
{
    version         2.0;
    format          ascii;
    class           dictionary;
    location        "system";
    object          sampleDict;
}

// * * * * * * * * * * * * * * * * * * * * * * * * * * * * * * * * * * * * * //

interpolationScheme cellPointFace;

setFormat raw;

sets
(
    line
    {
        type            uniform;
        axis            xyz;
        start           (0.005 0.005 0);
        end             (0.005 0.005 0.005);
    nPoints     1000;
    }

);

fields
(
    w1
    w2
    U
    T
    p
);


// ************************************************************************* //
```

LISTING D.18: File: DCMIX2case/system/sampleDict

```
/*--------------------------------*- C++ -*----------------------------------*\
| =========                 |                                                 |
| \\      /  F ield         | OpenFOAM: The Open Source CFD Toolbox           |
|  \\    /   O peration     | Version:  2.3.0                                 |
|   \\  /    A nd           | Web:      www.OpenFOAM.org                      |
|    \\/     M anipulation  |                                                 |
\*---------------------------------------------------------------------------*/
FoamFile
{
    version     2.0;
    format      ascii;
    class       dictionary;
    location    "system";
    object      setFieldsDict;
}
// * * * * * * * * * * * * * * * * * * * * * * * * * * * * * * * * * * * * * //

defaultFieldValues
(
    volScalarFieldValue w1 0

    volScalarFieldValue w2 0

    volScalarFieldValue w3 0
);

regions
(
    boxToCell
    {
        box (0 0 0) (0.006 0.006 0.005000);
        fieldValues
        (
            volScalarFieldValue w1 0.45
            volScalarFieldValue w2 0.1
            volScalarFieldValue w3 0.45
        );
    }

    boxToCell
    {
        box (0 0 0.005) (0.006 0.006 0.01000);
        fieldValues
        (
            volScalarFieldValue w1 0.45
            volScalarFieldValue w2 0.1
            volScalarFieldValue w3 0.45
        );
    }

);


// ************************************************************************* //
```

Listing D.19: File: DCMIX2case/system/setFieldsDict

Bibliography

[1] ESA, Record boost for ATV. http://www.esa.int/Our_Activities/Human_Spaceflight/ATV/Record_boost_for_ATV_to_raise_ISS_orbit.

[2] *OpenFOAM, The Open Source CFD Toolbox, User Guide.*

[3] Principal Investigator Microgravity Science NASA Handbook. https://pims.grc.nasa.gov/handbook/.

[4] Principal Investigator Microgravity Science NASA website. https://pims.grc.nasa.gov/html/ISSAccelerationArchive.html.

[5] Abbasi, A. *Theoretical Investigation of Thermodiffusion (Soret Effect) in Multicomponent Mixtures.* PhD thesis, 2010.

[6] Ahadi, A., and Saghir, M. Z. Transient effect of micro vibration from two space vehicles on mixture during thermodiffusion experiment. *Microgravity Science and Technology 25*, 2 (2013), 127–139.

[7] Ahadi, A., and Saghir, M. Z. New experimental method to measure pure and cross diffusion coefficients of transparent ternary mixtures using Mach–Zehnder interferometry. *Optics and Lasers in Engineering 59* (2014), 72–81.

[8] Ahadi, A., and Saghir, M. Z. The microgravity DSC-DCMIX1 mission onboard ISS: Experiment description and results on the measurement of the Soret coefficients for isobutylbenzene, dodecane, tetralin ternary hydrocarbons mixtures. *Experimental Thermal and Fluid Science 74* (jun 2016), 296–307.

[9] Ahadi, A., and Ziad Saghir, M. Contribution to the benchmark for ternary mixtures: Transient analysis in microgravity conditions. *European Physical Journal E 38*, 4 (2015).

[10] Aller, L., and Chapman, S. Diffusion in the Sun. *The Astrophysical Journal 132* (1960), 461.

[11] Blanco, P., Bou-Ali, M. M., Platten, J. K., de Mezquia, D. A., Madariaga, J. A., and Santamaría, C. Thermodiffusion coefficients of binary and ternary hydrocarbon mixtures. *The Journal of chemical physics 132*, 11 (2010), 114506.

[12] Bou-Ali, M., Ahadi, A., de Mezquia, D. A., Galand, Q., Gebhardt, M., Khlybov, O., Köhler, W., Larrañaga, M., Legros, Jean Claudeand Lyubimova, T., et al. Benchmark values for the soret, thermodiffusion and molecular diffusion coefficients of the ternary mixture tetralin+ isobutylbenzene+ n-dodecane with 0.8-0.1-0.1 mass fraction. *The European Physical Journal E 38*, 4 (2015), 30.

[13] Bou-Ali, M. M., Ecenarro, O., Madariaga, J. A., Santamaría, C. M., and Valencia, J. J. Measurement of negative soret coefficients in a vertical fluid layer with an adverse density gradient. *Physical Review E 62* (Jul 2000), 1420–1423.

[14] Candes, E. J., Sing-Long, C. A., and Trzasko, J. D. Unbiased risk estimates for singular value thresholding and spectral estimators. *IEEE transactions on signal processing 61*, 19 (2013), 4643–4657.

[15] Ceglia, E. European users guide to low gravity platforms. *Erasmus User Center and Communication Office, ESA* (2005).

[16] Chacha, M., Faruque, D., Saghir, M., and Claude, L. J. Solutal thermodiffusion in binary mixture in the presence of g-jitter. *International Journal of Thermal Sciences 41*, 10 (2002), 899 – 911.

[17] Chacha, M., and Saghir, M. Solutal-thermo-diffusion convection in a vibrating rectangular cavity. *International Journal of Thermal Sciences 44*, 1 (2005), 1 – 10.

[18] Chacha, M., Saghir, M., and Viviani, A. 3d numerical simulations of thermodiffusion experiment for a ternary mixture on-board foton. *Microgravity-Science and Technology 17*, 2 (2005), 31–37.

[19] Chapman, S. Thermal Diffusion in Ionized Gases. *Proceedings of the Physical Society 72* (1958).

[20] Chompusri, Y., Dejhan, K., and Yimman, S. Mother wavelet selecting method for selective mapping technique ecg compression. In *2012 9th International Conference on Electrical Engineering/Electronics, Computer, Telecommunications and Information Technology* (May 2012), pp. 1–4.

[21] Cohen, A. Ten lectures on wavelets, cbms-nsf regional conference series in applied mathematics, vol. 61, i. daubechies, siam, 1992, xix+ 357 pp. *Journal of Approximation Theory 78*, 3 (1994), 460–461.

[22] Croccolo, F., Giraudet, C., Bataller, H., Cerbino, R., and Vailati, A. Shadowgraph Analysis of Non-equilibrium Fluctuations for Measuring Transport Properties in Microgravity in the GRADFLEX Experiment. *Microgravity Science and Technology 28*, 4 (2016), 467–475.

[23] de Mezquia, D. A., Larrañaga, M., Bou-Ali, M. M., Madariaga, J. A., Santamaría, C., and Platten, J. K. Contribution to thermodiffusion coefficient measurements in dcmix project. *International Journal of Thermal Sciences 92* (2015), 14 – 16.

[24] Donoho, D. L., and Johnstone, I. M. Adapting to unknown smoothness via wavelet shrinkage. *Journal of the American Statistical Association 90*, 432 (1995), 1200–1224.

[25] Duhr, S., and Braun, D. Why molecules move along a temperature gradient. *Proceedings of the National Academy of Sciences 103*, 52 (2006), 19678–19682.

[26] Ergen, B. Comparison of wavelet types and thresholding methods on wavelet based denoising of heart sounds. *Journal of Signal and Information Processing 4*, 03 (2013), 164.

[27] ESA. SODI-DCMIX3 hardware, 2010.

[28] Galand, Q., and Van Vaerenbergh, S. Contribution to the benchmark for ternary mixtures: Measurement of diffusion and soret coefficients of ternary system tetrahydronaphtalene-isobutylbenzene-n-dodecane with mass fractions 80-10-10 at 25° c. *The European Physical Journal E 38*, 4 (2015), 26.

[29] Galliero, G., Bataller, H., Croccolo, F., Vermorel, R., Artola, P.-A., Rousseau, B., Vesovic, V., Bou-Ali, M., De Zárate, J. M. O., Xu, S., and Montel, F. Impact of thermodiffusion on the initial vertical distribution of species in hydrocarbon reservoirs. *Microgravity Science and Technology 28*, 2 (2016), 79–86.

[30] Gaponenko, Y., Mialdun, A., and Shevtsova, V. Experimental and numerical analysis of mass transfer in a binary mixture with Soret effect in the presence of weak convection. *The European Physical Journal E 37*, 10 (2014), 90.

[31] Gebhardt, M., and Köhler, W. Contribution to the benchmark for ternary mixtures: measurement of the soret and thermodiffusion coefficients of tetralin+ isobutylbenzene+ n-dodecane at a composition of (0.8/0.1/0.1) mass fractions by two-color optical beam deflection. *The European Physical Journal E 38*, 4 (2015), 24.

[32] Ghorayeb, K., Firoozabadi, A., and Anraku, T. Interpretation of the unusual fluid distribution in the Yufutsu gas-condensate field. *Society of Petroleum Engineers 8*, 02 (2003), 114–123.

[33] Goswami, J. C., and Chan, A. K. *Fundamentals of wavelets: theory, algorithms, and applications*, vol. 233. John Wiley & Sons, 2011.

[34] Grossmann, T., and Winkelmann, J. Ternary diffusion coefficients of cyclohexane + toluene + methanol by taylor dispersion measurements at 298.15 k. part 1. toluene-rich area. *Journal of Chemical & Engineering Data 54*, 2 (2009), 405–410.

[35] Grossmann, T., and Winkelmann, J. Ternary Diffusion Coefficients of Cyclohexane plus Toluene plus Methanol by Taylor Dispersion Measurements at 298.15 K. Part 1. Toluene-Rich Area. *Journal of Chemical and Engineering Data 54*, 2 (2009), 405–410.

[36] Grossmann, T., and Winkelmann, J. Ternary Diffusion Coefficients of Cyclohexane plus Toluene plus Methanol by Taylor Dispersion Measurements at 298.15 K. Part 2. Toluene-Rich Area. *Journal of Chemical and Engineering Data 54*, 2 (2009), 485–490.

[37] Holt, T., Lindeberg, E., and Ratkje, K. S. The effect of gravity and temperature gradients on methane distribution in oil reservoirs. *Society of Petroleum Engineers* (1983).

[38] Issa, R. Solution of the implicitly discretised fluid flow equations by operator-splitting. *Journal of Computational Physics 62*, 1 (1986), 40 – 65.

[39] Jeong, J., and Hussain, F. On the identification of a vortex. *Journal of Fluid Mechanics 285* (1995), 69–94.

[40] Jules, K., Hrovat, K., Kelly, E., and Reckart, T. International space station increment-6/8 microgravity environment summary report november 2002 to april 2004.

[41] Jules, K., McPherson, K., Hrovat, K., and Kelly, E. Initial characterization of the microgravity environment of the international space station: increments 2 through 4. *Acta astronautica 55*, 10 (2004), 855–887.

[42] Jurado, R., Gavaldà, J., Simón, M. J., Pallarés, J., Laverón-Simavilla, A., Ruiz, X., and Shevtsova, V. Some considerations on the vibrational environment of the DSC-DCMIX1 experiment onboard ISS. *Acta Astronautica 129*, July (2016), 345–356.

[43] Jurado, R., Pallarès, J., Gavaldà, J., and Ruiz, X. On the impact of the ISS reboosting maneuvers during thermodiffusion experiments of ternary liquid systems: Pure diffusion. *International Journal of Thermal Sciences 132*, November 2017 (2018), 186–198.

[44] Kania, M., Fereniec, M., and Maniewski, R. Wavelet denoising for multi-lead high resolution ecg signals. *Measurement science review 7*, 4 (2007), 30–33.

[45] Khlybov, O. A., Ryzhkov, I., and Lyubimova, T. Contribution to the benchmark for ternary mixtures: measurement of diffusion and soret coefficients in 1, 2, 3, 4-tetrahydronaphthalene, isobutylbenzene, and dodecane onboard the iss. *The European Physical Journal E 38*, 4 (2015), 29.

[46] Khoshnevis, A., Ahadi, A., and Saghir, M. Influence of static and oscillatory gravity fields on thermodiffusion of a binary mixture. *International Journal of Thermal Sciences 75* (2014), 221 – 232.

[47] Khoshnevis, A., Ahadi, A., and Saghir, M. On the influence of g-jitter and prevailing residual accelerations onboard international space station on a thermodiffusion experiment. *Applied Thermal Engineering 68*, 1 (2014), 36 – 44.

[48] Kitmacher, G. H. *Reference guide to the international space station.* 2006.

[49] Köhler, W., Krekhov, A., and Zimmermann, W. *Thermal diffusion in polymer blends: criticality and pattern formation*, vol. 227. Springer, 2009, pp. 145–198.

[50] Kolodner, P., Williams, H., and Moe, C. Optical measurement of the Soret coefficient of ethanol/water solutions. *The Journal of Chemical Physics 88*, 10 (1988), 6512–6524.

[51] Lapeira, E. *Análisis de los fenómenos de transporte en mezclas multicomponentes en condiciones terrestres mediante técnicas convectivas y no convectivas.* PhD thesis, Mondragon Unibersitatea, 2017.

[52] Larrañaga, M. *Determinación de las propiedades de transporte en mezclas multicomponentes.* PhD thesis, 2015.

[53] Larrañaga, M., Bou-Ali, M. M., de Mezquia, D. A., Rees, D. A. S., Madariaga, J. A., Santamaría, C., and Platten, J. K. Contribution to the benchmark for ternary mixtures: Determination of soret coefficients by the thermogravitational and the sliding symmetric tubes techniques. *The European Physical Journal E 38*, 4 (2015), 28.

[54] Larrañaga, M., Bou-Ali, M. M., Lizarraga, I., Madariaga, J. A., and Santamaría, C. Soret coefficients of the ternary mixture 1, 2, 3, 4-tetrahydronaphthalene+ isobutylbenzene+ n-dodecane. *The Journal of chemical physics 143*, 2 (2015), 024202.

[55] Larrañaga, M., Rees, D. A. S., and Bou-Ali, M. M. Determination of the molecular diffusion coefficients in ternary mixtures by the sliding symmetric tubes technique. *The Journal of Chemical Physics 140*, 5 (feb 2014), 054201.

[56] Legros, J. C., Gaponenko, Y., Mialdun, A., Triller, T., Hammon, A., Bauer, C., Köhler, W., and Shevtsova, V. Investigation of fickian diffusion in the ternary mixtures of water–ethanol–triethylene glycol and its binary pairs. *Phys. Chem. Chem. Phys. 17* (2015), 27713–27725.

[57] Ludwig, C. Diffusion zwischen ungleich erwärmten Orten gleich Zusammengesetz lösungen. *Akad Wiss Wien Math-Naturwiss Kl 20* (1856), 539.

[58] Lyubimova, T., Shklyaeva, E., Legros, J. C., Shevtsova, V., and Roux, B. Numerical study of high frequency vibration influence on measurement of Soret and diffusion coefficients in low gravity conditions. *Advances in Space Research 36*, 1 (2005), 70–74.

[59] Mallat, S. *A wavelet tour of signal processing: the sparse way.* Academic press, 2008.

[60] Marín, M., Dubert, D., Simón, M. J., Ollé, J., Gavaldà, J., and Ruiz, X. ISS quasi-steady accelerometric data as a tool for the fetection of external eisturbances during the period 2009-2016. *Microgravity Science and Technology* (2018), 1–24.

[61] Martin, A., and Bou-Ali, M. M. Determination of thermal diffusion coefficient of nanofluid: fullerene-toluene. *Comptes Rendus Mécanique 339*, 5 (2011), 329–334.

[62] McDougall, T. J. Double-diffusive convection caused by coupled molecular diffusion. *Journal of Fluid Mechanics 126* (1983), 379–397.

[63] McPherson, K., Hrovat, K., Kelly, E., and Keller, J. A researcher's guide to: International space station acceleration environment. *National Aeronautics and Space Administration* (2015).

[64] McPherson, K., Kelly, E., and Keller, J. Acceleration environment of the international space station. In *47th AIAA Aerospace Sciences Meeting including The New Horizons Forum and Aerospace Exposition* (2009), p. 957.

[65] McPherson, K., Kenneth, H., Kelly, E., and Jennifer, K. *A Researcher's Guide to: International Space Station Acceleration Environment*, 2015.

[66] Mialdun, A., Legros, J. C., Yasnou, V., Sechenyh, V., and Shevtsova, V. Contribution to the benchmark for ternary mixtures: Measurement of the soret, diffusion and thermodiffusion coefficients in the ternary mixture thn/ibb/nc 12 with 0.8/0.1/0.1 mass fractions in ground and orbital laboratories. *The European Physical Journal E 38*, 4 (2015), 27.

[67] Mialdun, A., Ryzhkov, I., Khlybov, O., Lyubimova, T., and Shevtsova, V. Measurement of Soret coefficients in a ternary mixture of toluene–methanol–cyclohexane in convection-free environment. *The Journal of Chemical Physics 148*, 4 (jan 2018), 044506.

[68] Mialdun, A., Sechenyh, V., Legros, J. C., Ortiz De Zárate, J. M., and Shevtsova, V. Investigation of fickian diffusion in the ternary mixture of 1, 2, 3, 4-tetrahydronaphthalene, isobutylbenzene, and dodecane. *The Journal of Chemical Physics 139*, 10 (2013), 104903.

[69] Mialdun, A., and Shevtsova, V. Development of optical digital interferometry technique for measurement of thermodiffusion coefficients. *International Journal of Heat and Mass Transfer 51*, 11-12 (2008), 3164–3178.

[70] Mialdun, A., Yasnou, V., and Shevtsova, V. Measurement of isothermal diffusion coefficients in ternary mixtures using counter flow diffusion cell. *Comptes Rendus Mécanique 341*, 4 (2013), 462 – 468. 10th International Meeting on Thermodiffusion.

[71] Ngui, W. K., Leong, M. S., Hee, L. M., and Abdelrhman, A. M. Wavelet analysis: Mother wavelet selection methods. In *Advances in Manufacturing and*

Mechanical Engineering (11 2013), vol. 393 of *Applied Mechanics and Materials*, Trans Tech Publications, pp. 953–958.

[72] Ollé, J., Dubert, D., Gavaldà, J., Laverón-Simavilla, A., Ruiz, X., and Shevtsova, V. Onsite vibrational characterization of dcmix2/3 experiments. *Acta Astronautica 140* (2017), 409 – 419.

[73] Pallares, J., Gavaldà, J., and Ruiz, X. Solutal natural convection flows in ternary mixtures. *International Journal of Heat and Mass Transfer 106* (2017), 232–243.

[74] Parsa, A., Srinivasan, S., and Saghir, M. Z. Impact of density gradients on the fluid flow inside a vibrating cavity subjected to soret effect. *The Canadian Journal of Chemical Engineering 91*, 3 (2012), 550–559.

[75] Patankar, S. *Numerical heat transfer and fluid flow*. CRC press, 1980.

[76] Percival, D. B., and Walden, A. T. *Spectral Analysis for Physical Applications: Multitaper and Conventional Unvariate Techniques*. Cambridge University Press, 1993.

[77] Percival, D. B., and Walden, A. T. *Wavelet methods for time series analysis 4*, vol. 4. Cambridge university press, 2006.

[78] Platten, J. K. The Soret Effect: A Review of Recent Experimental Results. *Journal of Applied Mechanics 73*, 1 (2006), 5.

[79] Rahman, M. A., and Saghir, M. Z. Thermodiffusion or Soret effect: Historical review. *International Journal of Heat and Mass Transfer 73* (jun 2014), 693–705.

[80] Rogers, M. J., Hrovat, K., McPherson, K., Moskowitz, M. E., and Reckart, T. Accelerometer data analysis and presentation techniques.

[81] Sáez, N., Ruiz, X., Gavaldà, F., and Shevtsova, V. Comparative analyses of esa, nasa and jaxa signals of acceleration during the sodi-ividil experiment. *Microgravity Science and Technology 26*, 1 (2014), 57–64.

[82] Sáez, N., Ruiz, X., and Gavaldà, J. On the detection of external disturbances using reduced quasi-steady accelerometric data. ELGRA Biennial Symposium and General Assembly.

[83] Sechenyh, V., Legros, J. C., Mialdun, A., Ortiz de Zárate, J. M., and Shevtsova, V. Fickian diffusion in ternary mixtures composed by 1,2,3,4-tetrahydronaphthalene, isobutylbenzene, and n-dodecane. *The Journal of Physical Chemistry B 120*, 3 (2016), 535–548. PMID: 26700401.

[84] Shannon, C. E. A mathematical theory of communication. *Bell Syst. Tech. J 27*, 1 (1948), 379–423.

[85] Shenoi, B. A. *Introduction to digital signal processing and filter design*. John Wiley & Sons, 2005.

[86] Shevtsova, V., Gaponenko, Y., Sechenyh, V., Melnikov, D., Lyubimova, T., and Mialdun, A. Dynamics of a binary mixture subjected to a temperature gradient and oscillatory forcing. *Journal of Fluid Mechanics 767* (2015), 290–322.

[87] Shevtsova, V., Melnikov, D., Legros, J. C., Yan, Y., Saghir, Z., Lyubimova, T., Sedelnikov, G., and Roux, B. Influence of vibrations on thermodiffusion in binary mixture: A benchmark of numerical solutions. *Physics of Fluids 19*, 1 (jan 2007), 017111.

[88] Shevtsova, V., Santos, C., Sechenyh, V., Legros, J. C., and Mialdun, A. Diffusion and Soret in Ternary Mixtures. Preparation of the DCMIX2 Experiment on the ISS. *Microgravity Science and Technology 25*, 5 (2014), 275–283.

[89] Shu, Y., Li, B., and De Groh, H. C. Numerical study of g-jitter induced double-diffusive convection. *Numerical Heat Transfer: Part A: Applications 39*, 3 (2001), 245–265.

[90] Shukla, K. K., and Tiwari, A. K. *Efficient algorithms for discrete wavelet transform: with applications to denoising and fuzzy inference systems*. Springer Science & Business Media, 2013.

[91] Soret, C. Sur l'etat d'equilibre que prend au point de vue de sa concentration une dissolution saline primitivement homohéne dont deux parties sont portées à des températures différentes. *Archives des Sciences Physiques et Naturelles 2* (1879), 48–61.

[92] Srinivasan, S., Dejmek, M., and Saghir, M. Z. Thermo-solutal-diffusion in high pressure liquid mixtures in the presence of micro-vibrations. *International Journal of Thermal Sciences 49*, 9 (2010), 1613 – 1624.

[93] Srinivasan, S., and Saghir, M. Z. Experimental approaches to study thermodiffusion - A review. *International Journal of Thermal Sciences 50*, 7 (2011), 1125–1137.

[94] Srinivasan, S., and Saghir, M. Z. Impact of the vibrations on soret separation in binary and ternary mixtures. *Fluid Dynamics & Materials Processing 7*, 2 (2011), 201–216.

[95] Stein, C. M. Estimation of the mean of a multivariate normal distribution. *The annals of Statistics* (1981), 1135–1151.

[96] Taylor, R., and Krishna, R. *Multicomponent Mass Transfer*, vol. 2. John Wiley & Sons, 1993.

[97] Touzet, M., Galliero, G., Lazzeri, V., Saghir, M. Z., Montel, F., and Legros, J.-C. Thermodiffusion: From microgravity experiments to the initial state of petroleum reservoirs. *Comptes Rendus Mécanique 339*, 5 (2011), 318.

[98] Triller, T., Bataller, H., Bou-Ali, M. M., Braibanti, M., Croccolo, F., Ezquerro, J. M., Galand, Q., Gavaldà, J., Lapeira, E., Laverón-Simavilla, A., Lyubimova, T., Mialdun, A., Ortiz de zárate, J. M., Rodríguez, J., Ruiz, X., Ryzhkov, I., Shevtsova, V., Van Vaerenbergh, S., and Köhler, W. Thermodiffusion in ternary mixtures of water/ethanol/triethylene glycol: first report on the DCMIX3-experiments performed on the International Space Station. *Microgravity Science and Technology 30*, 3 (2018), 295–308.

[99] Vaseghi, S. V. *Advanced digital signal processing and noise reduction*. John Wiley & Sons, 2008.

[100] Versteeg, H. K., and Malalasekera, W. *Introduction to Computational Fluid Dynamics*, vol. 44. 2005.

[101] Welch, P. The use of fast fourier transform for the estimation of power spectra: A method based on time averaging over short, modified periodograms. *IEEE Transactions on Audio and Electroacoustics 15*, 2 (June 1967), 70–73.

[102] Yan, Y., Jules, K., and Saghir, M. A comparative study of g-jitter effect on thermal diffusion aboard the international spacestation. *Fluid Dyn. Mater. Process 3*, 3 (2007), 231–246.

[103] Yan, Y., Pan, S., Jules, K., and Saghir, M. Vibrational effect on thermal diffusion under different microgravity environments. *Microgravity-Science and Technology 19*, 2 (2007), 12.

[104] Yan, Y., Shevtsova, V., and Saghir, M. Numerical study of low frequency g-jitter effect on thermal diffusion. *Fluid Dynamics and Material Processing 1*, 4 (2005), 315–328.

[105] Yan, Y., Viviani, A., and Saghir, M. Z. Double diffusion convection under sinusoidal modulations of low-frequency vibrations. *Acta Astronautica 63*, 5 (2008), 665 – 672.

[106] Zavalishin, D., Belyaev, M. Y., and Sazonov, V. Study of vibration microaccelerations onboard the international space station. *Cosmic Research 51*, 4 (2013), 261–269.